Intracellularly Targeted Optogenetic Actuators

Von der Fakultät für Mathematik, Informatik und Naturwissenschaften der RWTH Aachen University zur Erlangung des akademischen Grades einer Doktorin der Naturwissenschaften genehmigte Dissertation

vorgelegt von

Jiali Wang, M.Sc.

aus

Shanxi, China

Berichter: *Universitätsprofessor Dr. Andreas Offenhäusser*
Universitätsprofessor Dr. Björn Michael Kampa

Tag der mündlichen Prüfung: *01.03.2023*

Abstract

Optogenetics thrived in recent years as a powerful technique combining optical and genetic methods to monitor and control cellular activity. Its prominent merits are relatively high temporal and spatial precision in comparison to the classical techniques. However, wild types of optogenetic actuators are usually distributed throughout the cells, which enables effective manipulation of the overall activity of cells but hampers their further applications at the subcellular level considering that cells, especially polarized cells, have vital morphological and functional compartmentalization. Thus, wild types of optogenetic actuators are limited for subcellular mechanism research, such as investigating subcellular physiology and intracellular signaling pathways. This limitation can be solved by restricting the expression of actuators in a specific subcellular compartment, which enables more precise optogenetic manipulation. Therefore, this work aims to subcellularly localize the expression of optogenetic actuators that have shown high whole cell currents when very small membrane areas are illuminated. To distribute the functional membrane proteins to subcellular regions, a key mechanism that cells use is specific sorting, the principles of which are conserved between polarized epithelia and neurons to a certain extent. In this work, the reported sorting motifs producing polarized expression in epithelia were used. The actuators constructed in this way may allow the use in both polarized cell types. Two types of subcellularly-localized optogenetic actuators were constructed by using seamless cloning.

For the first one, an apical targeting (AT) motif from rhodopsin was fused to the C-terminus of ChR2opt, an optimized version of Channelrhodopsin-2 (ChR2). It was found that this AT motif targeted ChR2opt primarily to somatodendritic compartment of neurons and apical surface of MDCK cells, as shown by fluorescent immunostaining. Then, electrophysiology characterizations were studied by using patch clamp technique combined with laser stimulation, suggesting the expression of ChR2opt-AT did not alter the intrinsic electrophysiological properties of neurons and the AT sequence did not affect the conduction function of channelrhodopsin. Also, major properties and kinetics of ChR2opt and ChR2opt-AT were compared when expressed in both neurons and HEK293 cells. Furthermore, the electrophysiological measurements of neurons confirmed that the spatial specificity of optogenetic manipulation by using ChR2opt-AT can be enhanced. Additionally, a retrograde trafficking of ChR2op-AT from axon to cell body was observed, and it was proposed that this polarized protein trafficking may be related to the function of dynein.

The second type of subcellular targeted optogenetic actuators was constructed based on the high current channelrhodopsin ChR2XXL, utilizing 5, 10, or 15 tandem repeats (TR) from mucin protein as N-terminal targeting motifs. The modified channelrhodopsin maintained its electrophysiological properties, which could be used to introduce continuous depolarization blocks to the cell membrane, demonstrating the feasibility of modifying the N-terminus of channelrhodopsins to create useful optogenetic tools. Then it was shown that these actuators

were subcellularly localized in polarized cells. In polarized epithelial cells, all three actuators were localized to the lateral membrane surface. In primary cortical neurons, TR5-ChR2XXL and TR10-ChR2XXL were mainly targeted to the somatodendrites, though TR15-ChR2XXL could not express well in neurons. Moreover, comparing the transfection efficiencies of these proteins in different cell types indicated that it was related to the cell types and tandem repeats' length.

In summary, two types of subcellular targeted optogenetic actuators were constructed, which could be used to probe cellular electrophysiological functions with increased spatial resolution. In addition, the present work showed either the C-terminus or N-terminus of channelrhodopsin-2 can be modified to construct subcellularly-localized actuators. The preserved channel function with the N-terminal modification opens more possibilities to use the often ignored N-terminal motifs, considering the most modifications of channelrhodopsins rely on replacing the globular C-terminal. Furthermore, the work verified for the first time to our knowledge that the targeting motifs from epithelial cells can be used to express compartment-specific optogenetic actuators in both neurons and epithelia. In this case, the more precise manipulation of ion currents will improve our understanding of the subcellular function of polarized cells.

Zusammenfassung

Die Optogenetik entwickelte sich in den letzten Jahren zu einer leistungsstarken Technik, die optische und genetische Methoden kombiniert, um die Zellaktivität zu überwachen und zu kontrollieren. Herausragende Vorzüge sind eine relativ hohe zeitliche und räumliche Genauigkeit im Vergleich zu den klassischen Techniken. Wildtypen von optogenetischen Aktoren sind jedoch normalerweise über die Zellen verteilt, was eine effektive Manipulation der Gesamtaktivität von Zellen ermöglicht, aber ihre weitere Anwendung auf subzellulärer Ebene behindert, wenn man bedenkt, dass Zellen, insbesondere polarisierte Zellen, eine lebenswichtige morphologische und funktionelle Kompartimentierung aufweisen. Daher sind Wildtypen von optogenetischen Aktoren für die Erforschung subzellulärer Mechanismen, wie die Untersuchung der subzellulären Physiologie und intrazellulärer Signalwege, begrenzt. Diese Einschränkung kann gelöst werden, indem die Expression von Aktoren in einem bestimmten subzellulären Kompartiment eingeschränkt wird, was eine präzisere optogenetische Manipulation ermöglicht. Daher zielt diese Arbeit darauf ab, die Expression von optogenetischen Aktoren subzellulär zu lokalisieren, die hohe Ganzzellströme gezeigt haben, wenn sehr kleine Membranbereiche beleuchtet wurden. Um die funktionellen Membranproteine in subzelluläre Regionen zu verteilen, ist ein Schlüsselmechanismus, den Zellen verwenden, die spezifische Sortierung, deren Prinzipien zwischen polarisierten Epithelien und Neuronen bis zu einem gewissen Grad konserviert sind. In dieser Arbeit wurden die berichteten Sortiermotive verwendet, die eine polarisierte Expression in Epithelien erzeugen. Die so konstruierten Aktoren können den Einsatz in beiden polarisierten Zelltypen ermöglichen. Zwei Arten von subzellulär lokalisierten optogenetischen Aktoren wurden durch nahtloses Klonen konstruiert.

Für das erste wurde ein apikales Targeting (AT)-Motiv von Rhodopsin mit dem C-Terminus von ChR2opt, einer optimierten Version von Channelrhodopsin-2 (ChR2), fusioniert. Es wurde festgestellt, dass dieses AT-Motiv ChR2opt hauptsächlich auf das somatodendritische Kompartiment von Neuronen und die apikale Oberfläche von MDCK-Zellen ausrichtete, wie durch fluoreszierende Immunfärbung gezeigt wurde. Dann wurden elektrophysiologische Charakterisierungen unter Verwendung der Patch-Clamp-Technik in Kombination mit Laserstimulation untersucht, was darauf hindeutet, dass die Expression von ChR2opt-AT die intrinsischen elektrophysiologischen Eigenschaften von Neuronen nicht verändert und die AT-Sequenz die Leitungsfunktion von Channelrhodopsin nicht beeinflusst. Außerdem wurden die wichtigsten Eigenschaften und Kinetiken von ChR2opt und ChR2opt-AT verglichen, wenn sie sowohl in Neuronen als auch in HEK293-Zellen exprimiert wurden. Darüber hinaus bestätigten die elektrophysiologischen Messungen von Neuronen, dass die räumliche Spezifität der optogenetischen Manipulation durch die Verwendung von ChR2opt-AT verbessert werden kann. Desweiteren wurde ein retrograder Transport von ChR2op-AT vom Axon zum Zellkörper beobachtet, und es wurde vorgeschlagen, dass dieser polarisierte Proteintransport

mit der Funktion von Dynein zusammenhängen könnte.

Der zweite Typ subzellulärer zielgerichteter optogenetischer Aktuatoren wurde basierend auf dem Hochstromkanalrhodopsin ChR2XXL konstruiert, wobei 5, 10 oder 15 Tandem-Wiederholungen (TR) aus dem Muzinprotein als N-terminale Zielmotive verwendet wurden. Das modifizierte Channelrhodopsin behielt seine elektrophysiologischen Eigenschaften bei, die verwendet werden können, um kontinuierliche Depolarisationsblöcke in die Zellmembran einzuführen, was die Machbarkeit der Modifikation des N-Terminus von Channelrhodopsin zur Schaffung nützlicher optogenetischer Werkzeuge demonstriert. Dann wurde gezeigt, dass diese Aktoren subzellulär in polarisierten Zellen lokalisiert sind. In polarisierten Epithelzellen sind alle drei Aktoren an der lateralen Membranoberfläche lokalisiert. In primären kortikalen Neuronen zielten TR5-ChR2XXL und TR10-ChR2XXL hauptsächlich auf die Somatodendriten ab, obwohl TR15-ChR2XXL in Neuronen nicht gut exprimieren konnte. Darüber hinaus zeigte der Vergleich der Transfektionseffizienz dieser Proteine in verschiedenen Zelltypen, dass dies mit den Zelltypen und der Länge der Tandem-Wiederholungen zusammenhängt.

Zusammenfassend wurden zwei Arten von subzellulären zielgerichteten optogenetischen Aktoren konstruiert, die verwendet werden können, um zelluläre elektrophysiologische Funktionen mit erhöhter räumlicher Auflösung zu untersuchen. Darüber hinaus zeigte die vorliegende Arbeit, dass entweder der C-Terminus oder der N-Terminus von Channelrhodopsin-2 modifiziert werden kann, um subzellulär lokalisierte Aktuatoren zu konstruieren. Die erhaltene Kanalfunktion mit der N-terminalen Modifikation eröffnet mehr Möglichkeiten, die oft ignorierten N-terminalen Motive zu verwenden, wenn man bedenkt, dass die meisten Modifikationen von Kanalrhodopsinen auf dem Ersatz des kugelförmigen C-Terminus beruhen. Darüber hinaus bestätigte die Arbeit unseres Wissens zum ersten Mal, dass die Targeting-Motive von Epithelzellen verwendet werden können, um kompartimentspezifische optogenetische Aktoren sowohl in Neuronen als auch in Epithelien zu exprimieren. In diesem Fall wird die genauere Manipulation von Ionenströmen unser Verständnis der subzellulären Funktion polarisierter Zellen verbessern.

Contents

1 Introduction

This chapter provides the fundamental theory and background of this work. First, the basic structure and function of neurons, electrophysiological fundamentals, and neuronal polarization *in vitro* are introduced, along with the basics of epithelial cells (**Section 1.1**). Then, the basic information about optogenetics is presented, primarily including the history, general strategy, and problems facing currently, based on which the motivation of this work is proposed (**Section 1.2**). Next, the classical optogenetic actuator channelrhodopsin-2 is introduced emphatically (**Section 1.3**) as this work is conducted based on two mutants of this actuator. Subsequently, the subcellular targeting strategy utilized in this work is provided with an emphasis on the conservative targeting mechanism of protein trafficking in polarized cells along with two different targeting motifs used (**Section 1.4**). Finally, the patch clamp technique is presented (**Section 1.5**) as it is the major electrophysiological readout method applied in this work.

1.1 The polarized cells

Organisms generally have a highly ordered hierarchical organization. A typical animal body is formed by multiple organ systems, each of which is made up of organs that work together. The organ performing a specific function is composed of various tissues. The tissue is a group of similar cells. As the basic structural and functional unit of living organisms, cells differentiate into a variety of types performing various functions [1]. The majority of cells have polarity, which refers to the asymmetry of a cell in morphology and function. Cell polarity is crucial to many biological processes such as reproduction, development, and homeostasis [2]. The neurons in the nervous tissue and epithelial cells in the epithelial tissue are two representative polarized cells. The following subsections will introduce these two types of cells with an emphasis on neurons.

1.1.1 The neuron

1.1.1.1 Structure and function of a neuron

The neuron is one of the most complex cells in nature and it is the basic structural and functional unit of the nervous system (**Figure 1.1**). Although there are different types of neurons such as sensory neurons, interneurons, and motor neurons, a typical neuron is composed of a cell body and neurites, including multiple dendrites and a single axon. The cell body is also named soma where the nucleus and most of the organelles like endoplasmic reticulum, Golgi apparatus, and mitochondria are located, maintaining the fundamental function of a neuron. The dendrites are short (~100-300 μm) and highly branched, which taper gradually towards the end, while the axon is much longer (could be more than 1 m), and has a relatively constant diameter. The

soma and dendrites are grouped in the somatodendritic area and a short region (~ 40 μm) called the axon initial segment (AIS) or axon hillock separates this area from the axon. These compartments differ in cytoskeletal structure and membrane composition. Take microtubules for example, they have a uniform plus-end out orientation in axon while their polarity is mixed in dendrites. Another example is that there are lots of voltage-gated ion channels located at AIS but not at other compartments. This highly specialized cellular organization provides a structural basis for neuronal function. The main function of neurons is to receive, integrate, and transmit information. Dendrites as well as the cell body receive sensory information or output from other cells as input signals in the form of electrical signals. Then cell integrates these signals temporally and spatially, and if the integrated signals are suprathreshold, action potentials would be initiated at the axon hillock. Electrical signals travel along the axon and down to its terminal, which forms a junction called synapse with another cell. The electrical signals trigger regulated release of chemical signals stored in synaptic vesicles. These chemical signals are neurotransmitters, which bind to the receptors in downstream target cells and trigger new electrical signals in the cells. Each neuron has multiple dendrites and an axon with massive branches at its terminals, enabling it to communicate with thousands of other neurons. Take human brain as an example, it has billions of neurons and trillions of synapses, forming a complicated neural network.

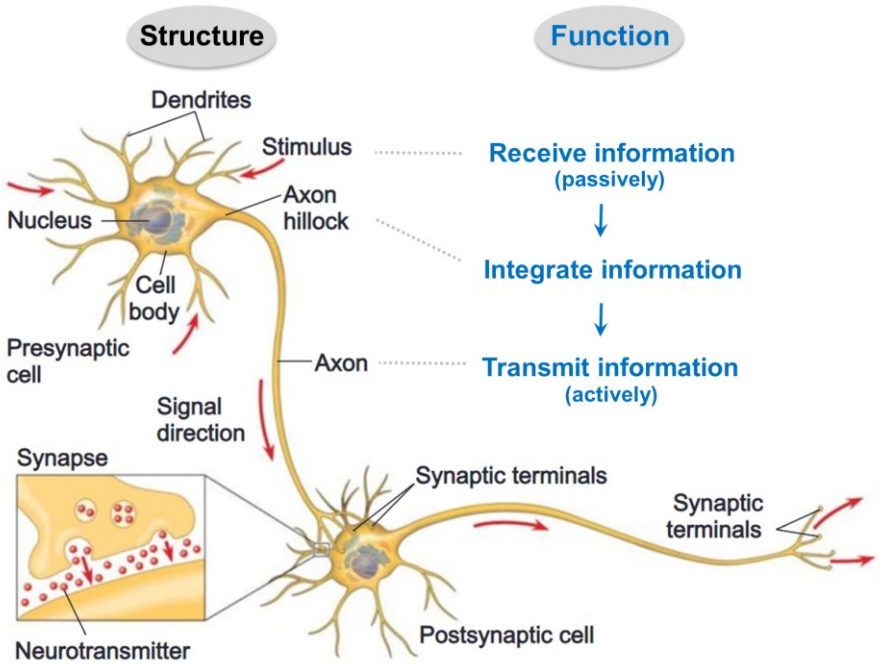

Figure 1.1 The basic structure and function of neurons. The main structures of a neuron are dendrite, soma and axon. Dendrites receive information, which is integrated at the axon hillock, then the axon transmits the information to the next neuron through a synapse. Image adapted from [3].

1.1.1.2 Electrophysiology of neurons

1). Resting potential

As in other cells, the cell membrane of neurons separates the intracellular region from its extracellular environment. The various ions are unequally distributed at intracellular and extracellular compartments, which are established by active transporters embedded in the membrane. For instance, the high concentration of sodium ions (Na^+) outside the cell and potassium ions (K^+) inside the cell are maintained by the sodium-potassium pump. The plasma membrane has ionic permselectivity, permitting certain ions to move across the membrane more easily than others. Take K^+ as an example, when K^+ diffuses down its concentration gradient through K^+ channel, the positive charge carried by K^+ also moves across the membrane, which produces an electrical force across the membrane. This electrical force has an opposite direction to the chemical force. When these two forces reach a balance, the net flow of K^+ across membrane is zero. The electrical force at this equilibrium is the potassium's equilibrium potential, which can be calculated by using the Nernst equation (1.1).

$$E_x = \frac{RT}{zF} ln \frac{[x]_{out}}{[x]_{in}} \tag{1.1}$$

where E_x is the Nernst equilibrium potential of ion x, R is the universal gas constant, T is the absolute temperature, z is the valence of the ion x, and F is the Faraday constant. $[x]_{out}$ and $[x]_{in}$ are the concentrations of ion x at extracellular and intracellular compartments, respectively. In this Nernst equation, only a single permeant ion species is considered. Actually, there are multiple permeant ions across the neuronal membrane. In this case the Goldman equation (1.2) is applied, in which the relative permeability of the membrane to each permeant ion species is introduced.

$$V_x = \frac{RT}{zF} ln \left(\frac{P_x[x]_{out}}{P_x[x]_{in}} \right) \tag{1.2}$$

where V_x is the membrane potential generated by ion x, P_x is the relative permeability of ion x across the membrane, and other parameters are all the same as in the Nernst equation (1.1). For neurons, the primary permeant ions are K^+, Na^+ and chloride (Cl^-). Therefore, the membrane potential generated by these ions can be calculated by using the Goldman equation (1.3).

$$V_m = \frac{RT}{F} ln \left(\frac{P_{K^+}[K^+]_{out} + P_{Na^+}[Na^+]_{out} + P_{Cl^-}[Cl^-]_{in}}{P_{K^+}[K^+]_{in} + P_{Na^+}[Na^+]_{in} + P_{Cl^-}[Cl^-]_{out}} \right) \tag{1.3}$$

where V_m is the membrane potential of a neuron. There is one positive charge per Na^+ and per K^+, and one negative charge per Cl^-, so the z for Na^+, K^+ and Cl^- are +1, +1 and -1, respectively. Other parameters are as illustrated above. For neurons at a resting state without signaling, the membrane potential is called resting potential (**Figure 1.3**), usually in the range of -60 ~ -80

millivolts (mV). It is much closer to the equilibrium potential for K^+ (-90 mV at 37℃) rather than the equilibrium potential for Na^+ (+62 mV at 37℃) because the membrane of a resting neuron has a larger permeability to K^+ than to Na^+, which means there are more K^+ channels than Na^+ channels open at the resting state.

2). Graded potential and action potential

The function of information processing of neurons is realized in the form of electrical signals and chemical signals. The chemical signals are mediated by neurotransmitters that pass information from the transmitting neuron to the receiving cell. As for the electrical signals, they can be divided into two types, graded potential and action potential.

Graded potential

The graded potential is a shift in membrane potential that varies with the magnitude of the subthreshold stimulus. The graded potential is usually small and dissipates over space and time. The passive conduction of electrical signals along dendrites or non-myelinated axons has been described by using cable theory. Accordingly, the electrical properties of neurons underlying the propagation of electrical signals are called cable properties. The cable theory was first proposed by William Thomson in 1854 to describe signal decay in underwater telegraph cables [4]. For applying this theory to the signal conduction of neurons, a series of simplified assumptions are made [5] so that an equivalent electrical circuit can be constructed (**Figure 1.2**). One of the basic assumptions is that the segments of neurites are uniform cylinders with parallel capacitances and resistances. First, the insulating plasma membrane separates conductive extracellular solution from conductive intracellular solution, so it acts as a capacitor. Second, the membrane prevents the ion from flowing through the membrane, so it behaves as a resistor in the meanwhile. Besides, there are also resistances against the charge movement at intracellular and extracellular solutions. However, the external resistance is relatively low compared with the internal resistance owing to the large extracellular volume, so the external resistance is assumed to be negligible.

Here membrane resistance r_m and membrane capacitance c_m are both defined in per unit length, and the internal longitudinal resistance of cytoplasm is denoted as r_i. Given that the specific membrane resistance R_m and specific membrane capacitance C_m are defined in per unit area, the internal resistance of cytoplasm is R_i and the radius of the assumed cylinder is a, their corresponding relationships are as follows.

$$r_m = \frac{R_m}{2\pi a}$$

$$c_m = C_m 2\pi a$$

$$r_i = -\frac{R_i}{\pi a^2}$$

In order to easily derive the cable equation, it is first assumed that there is no leakage current flowing through the membrane, so the r_m is infinite. Also the c_m is assumed to be zero. If a current is injected at position $x = 0$ inside the neuronal fiber, the internal longitudinal current (i_i) can be given as equation (1.4) based on Ohm's Law.

$$i_i = -\frac{1}{r_i}\frac{\partial V}{\partial x} \tag{1.4}$$

where V is voltage over length x along the neuronal fiber. Then the reality that ions are fluxing through the membrane is considered. According to the Kirchoff's Law, the membrane current (i_m) is calculated by equation (1.5)

$$i_m = -\frac{\partial i_i}{\partial x} \tag{1.5}$$

Considering from another aspect, the i_m can be divided into capacitive current (i_c) and resistive current (i_r). Further, the i_c is related to c_m and membrane voltage V over time t. The i_r is equal to V divided by r_m according to Ohm's Law. Thus the i_m can be given by equation (1.6).

$$i_m = i_c + i_r = c_m\frac{\partial V}{\partial t} + \frac{V}{r_m} \tag{1.6}$$

Combining equations 1.4, 1.5 and 1.6 produces the cable equation (1.7).

$$\frac{r_m}{r_i}\frac{\partial^2 V}{\partial^2 x} - V = c_m r_m\frac{\partial V}{\partial t} \tag{1.7}$$

Then, two passive properties of the membrane are introduced. The length constant or space constant λ is defined as the square root of r_m/r_i (equation (1.8)), which represents the speed of a subthreshold potential spread over distance. The larger the λ, the greater the distance that the electrical signal can spread. Whereas the time constant τ is defined as the product of c_m and r_m (equation (1.9)), which represents the rate of charging or discharging the membrane over time. The smaller the τ, the more rapidly the change of membrane potential would be.

$$\lambda = \sqrt{\frac{r_m}{r_i}} \tag{1.8}$$

$$\tau = c_m r_m \tag{1.9}$$

Introducing equation (1.8) and equation (1.9) into equation (1.7) produces the updated cable equation (1.10).

$$\lambda^2\frac{\partial^2 V}{\partial^2 x} - V = \tau\frac{\partial V}{\partial t} \tag{1.10}$$

Therefore, the propagation of electrical signals along the neurites over space and time can be mathematically understood with the cable equation. Especially, the introduction of space

constant and time constant simplify the spatial and temporal description of signal decay. For instance, with increasing distance from the stimulus site, the magnitude of the membrane potential change decays as current leaks out of the neuronal fiber, and if the membrane resistance is larger, the longer the electrical signal would travel along the fiber. Also the smaller the membrane capacitance, the less the current loss and the faster the electrical signal propagates. Hence, the cable theory is useful in analyzing and explaining the electrophysiological signals of neurons and is also critical in computational neuroscience.

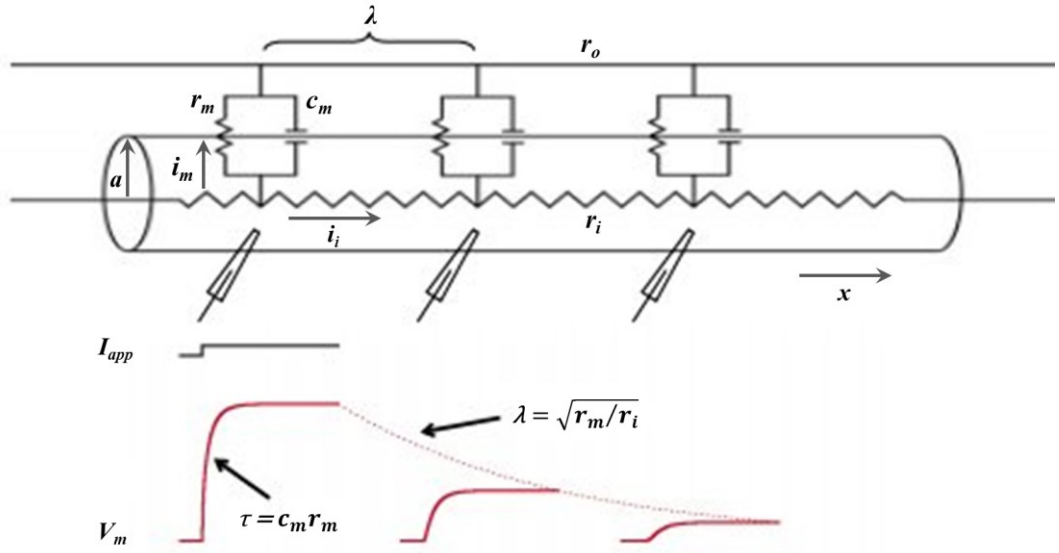

Figure 1.2 Cable theory model of electrical signal conduction along the neuronal fiber. The electrical circuits are composed of a series of parallel capacitances and resistances. The radius of neuronal fiber is a. In infinitely small segment x, membrane resistance is r_m and membrane capacitance is c_m. The current passing through the membrane is i_m and the internal longitudinal current is i_i. Internal longitudinal resistance of cytoplasm is r_i, and external resistance r_o is relatively small so that it can be neglected. Two passive properties of the membrane, space constant λ and time constant τ, are shown. In response to injected current I_{app}, the amplitude of resulting membrane potential change V_m decays over space and time. Image adapted from [6].

Action potential

An action potential will be initiated if a stimulus is sufficiently strong and the triggered depolarization researches threshold (about -55 mV). The action potential is a massive and rapid membrane potential change with a characteristic shape (**Figure 1.3**). Unlike graded potential, action potential has a constant magnitude and an all-or-none feature. The initiation of action potential is attributed to a large number of voltage-gated sodium and potassium channels at AIS. Fast voltage-gated sodium channels open first, which permit massive sodium ions to inflow rapidly owing to the high sodium concentration on the extracellular side, forming a fast-rising phase (depolarizing phase) of the action potential. Then sodium channels inactivate quickly, and meanwhile slow voltage-gated potassium channels open, which allows potassium ions outflowing, generating a falling phase (repolarizing phase) of the action potential. A transient undershoot phase (hyperpolarizing phase) follows, which is caused by the higher K^+

permeability of the membrane at this phase than at the resting level. Finally, the extra potassium channels close and membrane potential returns to the resting potential level. At the repolarizing phase and the beginning of the hyperpolarizing phase, the voltage-gated sodium channels are inactivated. During these periods, a second action potential can not be initiated, which is called refractory period.

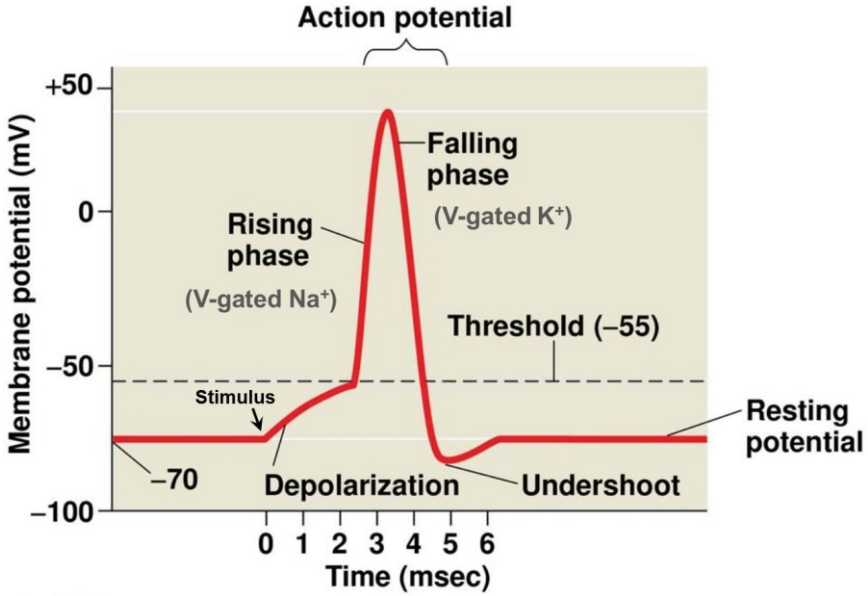

Figure 1.3 The schematic of a typical action potential. A neuron at resting state receives a stimulus that surpasses the threshold. Voltage-gated sodium (V-gated Na^+) channels open first, forming a fast-rising phase (depolarization). Then sodium channels inactivate quickly, whereas slow voltage-gated potassium (V-gated K^+) channels open, generating a falling phase (repolarization). Finally, a transient undershoot phase (hyperpolarization) follows and membrane potential returns to the resting potential level. Image adapted from [3].

The initiation and propagation of action potential can be explained by a Hodgkin-Huxley equivalent circuit model (**Figure 1.4**). This model was first proposed by Alan Lloyd Hodgkin and Andrew Fielding Huxley in 1952 to describe the electrical properties of membranes in neurons [7]. First, as mentioned above, the plasma membrane acts as a capacitor since it can separate and store charges. Meanwhile, the ion channels across the membrane behave as conductors as they have different permeabilities or conductances to different ion species. Therefore, the total membrane currents (I_m) are composed of two parts, one is capacitive current (I_c) and the other one is ionic current (I_i). Thus, the total currents passing through the membrane can be denoted by equation (1.11).

$$I_m = I_c + I_i \tag{1.11}$$

The I_c is determined by the membrane capacitance (C_m), membrane potential (E_m) and time (t). The I_i is divided into currents carried by sodium and potassium ions (I_{Na+} and I_{K+}, respectively), and leakage currents caused by chloride and other ions (I_l). Thus, the equation (1.11) can be denoted as equation (1.12).

$$I_m = C_m \frac{dE_m}{dt} + I_{Na^+} + I_{K^+} + I_l \tag{1.12}$$

Furthermore, according to Ohm's Law, the current is equal to voltage divided by resistance ($I = E/R$), and the conductance is the reciprocal of the membrane resistance ($g = 1/R$), so the current can be given as $I = gE$. Thus, the ionic currents are determined by the membrane conductance (g) and electrochemical driving force (E) that acts on the ion. For sodium and potassium currents, the conductances (g_{Na+} and g_{K+}) depend on membrane potential (E_m) and time (t), whereas the leakage conductance (g_l) does not. The driving force is derived from the difference between the membrane potential (E_m) and the equilibrium potential (E_{Na+}, E_{K+} and E_l) that can be calculated according to the Nernst equation (1.1). Thereby, the total currents across the membrane are given by equation (1.13).

$$I_m = C_m \frac{dE_m}{dt} + g_{Na^+}(E_m - E_{Na^+}) + g_{K^+}(E_m - E_{K^+}) + g_l(E_m - E_l) \tag{1.13}$$

The equation (1.13) is the mathematical form of the Hodgkin-Huxley equivalent circuit model. The model can accurately predict various features of the action potential and other related electrophysiological properties like the refractory period. The theory of action potential is evaluated as one of the most important mathematical models in neuroscience.

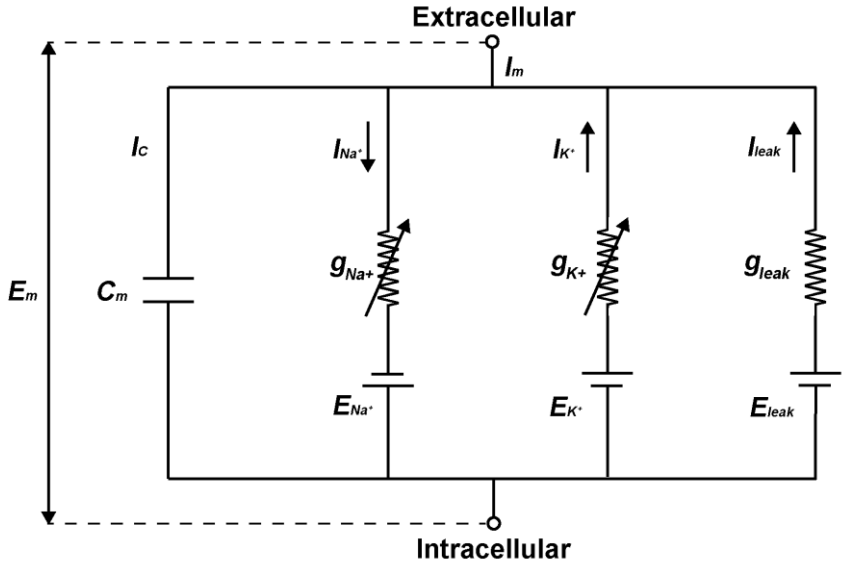

Figure 1.4 The conventional Hodgkin-Huxley equivalent circuit model. The electrical circuit contains four parallel branches, one is the capacitive branch and three are conductive or resistive branches. I_m is total membrane current, which is divided into capacitive current I_c and ionic currents. C_m is the specific capacitance of the plasma membrane. Ionic currents include I_{Na+}, I_{K+} and I_{leak}. I_{Na+} and I_{K+} are currents carried by sodium and potassium ions respectively, whereas I_{leak} is leakage current caused by chloride and other ions. g_{Na+}, g_{K+} and g_{leak} are conductances of Na^+, K^+ and leak current, and among them g_{Na+} and g_{K+} vary with membrane potential and time (resistor with an arrow) while g_{leak} is constant (resistor without an arrow). E_{Na+}, E_{K+} and E_{leak} are electrochemical gradients that drive ions passing through the ion channels. E_m is membrane potential.

1.1.1.3 The development stages of a neuron *in vitro*

The neuronal model systems are essential in neuroscience and *in vivo* and *in vitro* model systems have been available for a long time. *In vivo* model systems are valuable for many fields such as investigating neuronal development and degeneration, but the indefinite microenvironment caused by the inherent structural and functional complexity of various nerve cells makes it difficult to understand the observations at molecular or structural levels. Whereas *in vitro* model systems can provide defined homogeneous populations of cells, and can be easily applied in some fields such as electrophysiological research. Unlike many adherent cell lines that can grow on a polystyrene-treated substrate or bare borosilicate glass, neurons need to grow on further processed substrates. Animal cells *in vivo* are surrounded and supported by the extracellular matrix (ECM) which is a complex meshwork of polysaccharides and proteins such as laminin, fibronectin and vitronectin. Coating substrates with the extracts of these proteins facilitates *in vitro* culture of neurons as they can provide neurons with a mimetic extracellular condition. However, purifying natural ECM components is challenging and costly. The addition of synthetic polypeptides such as poly-l-lysine (PLL), poly-d-lysine (PDL) and poly-l-ornithine (PLO) is proven as a good alternative since they have abundant positive charges that facilitate the combination of negative charges of cells, promoting cell adhesion [8]. Meanwhile considering obtaining quality images by using phase contrast microscopy or others, glass coverslips are a good substrate to use. Therefore, neurons *in vitro* are usually cultured on ECM and polypeptide co-coated glass coverslips.

The basic property of neurons cultured *in vitro* is to establish and maintain neuronal polarity as they do *in vivo*, which is the foundation of the complexity of neuronal function. The specialization process to break the original symmetry and establish the cell polarity is termed neuronal polarization. For neurons grown *in vitro*, there are five stages of development characterized according to their morphological changes [9-12], as shown in **Figure 1.5**. At the first stage (0-0.25 d (day)), neurons are round spheres with small filopodia shortly after being dissociated from embryonic rat brains. Then, a few filopodia grow into immature neurites that display similar morphology and undergo dynamic growth and retraction, which comprises the second stage (0.25-1 d). Next, neurons enter the third stage (1-3 d), during this period one neurite extends faster than other neurites, becoming an axon with a growth cone at its tip. Although the axonal polarization is largely a matter of chance *in vitro*, it is induced by various internal or external symmetry breaking cues *in vivo,* such as the concentration gradients of TGF-β (transforming growth factor β), neurotrophins and N-Cadherin [11]. At the fourth stage (3-7 d), the axon keeps extending and the remaining neurites elongate and become dendrites. Finally, the axon and dendrites become mature with well-developed arbors, and synaptic contacts are established between dendritic spines and axonal terminals, forming a complex neural network at the fifth stage (> 7 d). Afterwards, the established cell polarity is maintained by neurons throughout their lives except in some special cases where neurons need to reestablish the cell polarity in response to new asymmetric cues.

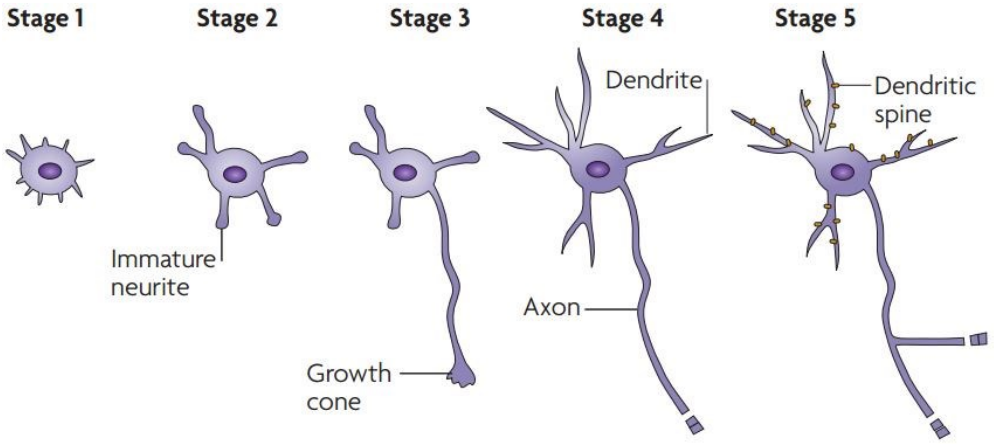

Figure 1.5 The development stages of a neuron *in vitro* to establish the neuronal polarity. Stage 1, after plating, round neurons form thin filopodia. Stage 2, immature neurites are projected, extending, and retracting dynamically. Stage 3, one neurite extends fast, becoming the axon. Stage 4, other neurites elongate and become dendrites. Stage 5, neurons become mature with dendritic spines and synapses, forming a complex neural network. Image adapted from [12].

1.1.2 The epithelial cell

The epithelia are tissues composed of a single layer or multiple layers of similar cells bound closely together. They cover all external and internal surfaces throughout the bodies of most animals, separating the internal medium from the outside environment and providing selective barriers at the interface. They line the surfaces of various organs and cavities, and they are the major tissues in glands [13, 14]. The epithelia can be classified by their shapes and layering. First, based on the shape, they are divided into three types, squamous, cuboidal, and columnar epithelia. Second, according to the number of layers, they are divided into another three types, simple, stratified, and pseudostratified epithelia [15].

The constituent cells of epithelia are epithelial cells, which can be divided into three domains. The region facing the exterior or lumen of organs is an apical domain, and the opposite side attached to the underneath is a basal domain. The region that adheres to the neighboring cells is a lateral domain. Since the basal and lateral membranes share some common properties, they are also referred to as basolateral membranes. The basolateral membrane is separated from the apical membrane by intercellular adhesion complexes based on cadherins. The junctional structures in vertebrates are tight junctions. The compartmentalized structures provide foundations for diverse functions. The apical surface is usually covered by specialized projections that confer it specific functions. For example, the microvilli on the apical side of small intestines increase the surface area, facilitating the absorption of nutrients. Cilia on the apical side of the respiratory tract help clear away the dust. The basal membrane attaches to a layer of extracellular matrix called basement membrane that provides a scaffolding for epithelia. Also the maintenance of epithelial physiological conditions relies on the absorption of essential substances from the underlying tissues by the basal membrane, as the epithelia are avascular, that is, they are not associated with or supplied by blood vessels. The tight junctions prevent

the movement of large molecules across the epithelium, serving as a selective filter. Overall, based on their morphology and location, epithelia play roles in secretion, diffusion, protection, active absorption, and so forth [14, 16, 17].

1.2 Optogenetics

Elucidating circuit functions benefits us to understand how a brain works and thereby to treat psychiatric disorders, but the complexity of the nervous system makes it a difficult task and it is still one of the major goals in neuroscience. Classical techniques such as electrophysiological stimulation and pharmacological intervention indeed are valuable tools that have broadened our understanding about the brain. Electrical stimulation has high temporal precision, however, it can not target a specific cell type, resulting in poor spatial resolution among different cell types. Local pharmacological intervention is also useful in many cases. However, this approach also suffers from the problem of low spatial resolution. Additionally, this method faces a low temporal resolution problem as well because of the slow release of drugs. In recent decades, novel neuronal activity stimulation methods utilizing various external energy sources are emerging such as optogenetics [18, 19], chemogenetics [20-22], thermogenetics [23-25], magnetogenetics [26-29] and sonogenetics [30-32]. Each method has its pros and cons [33-36]. For example, chemogenetics has high cell specificity and noninvasiveness, but the response is in the timescale of minutes. Compared with other approaches, optogenetics thrived in these years as a powerful technique, which combines optical and genetic methods to monitor or control biological functions. The tool used for monitoring the function is an optogenetic sensor and the tool used for controlling the function is an optogenetic actuator. This work mainly focuses on the latter. The optogenetic manipulation has high temporal precision that can be limited to a millisecond timescale, enabling it to match the fast speed of electrical activity in neurons (**Figure 1.3**). Also the control can only occur in specific cells expressing light-sensitive proteins, so it also has a high spatial resolution. Meanwhile, light control is reversible, that is, the initial state without light illumination can reappear after withdrawing light. Moreover, light stimulation can be applied to multiple targeting positions simultaneously. It is also possible to combine multiple light controls using proteins with different optical spectrums. Overall, the rise of optogenetics provides neuroscientists with an innovative way to conduct research in neuroscience.

1.2.1 The history of optogenetics

In the 19th century, eminent Russian botanist Andrei Sergeyevich Faminzin first described the effect of light on the movement of *Chlamydomonas* [37]. This initial exploration of light-sensitive protein laid the groundwork for the story of optogenetics. In 1979, Francis Crick suggested in *Scientific American* that the major challenge neuroscientists faced was the need to control one type of neuron in the brain while leaving others unaltered [38], which was the origin of the conceptual inspiration for optogenetics. 20 years later, Francis Crick presented in

a lecture that light potentially could be a relevant control tool but without a clear concept about how this could be achieved [39]. Gero Miesenböck's group first introduced a light-sensitive protein from the eyes of fruit flies into nerve cells and demonstrated that it was possible to use light to modify neuronal activity [40]. But this work did not receive much attention at that time owing to the limitations of the multiple-component system ChARGed and the slow kinetics. Until 2002 and 2003 when Georg Nagel and colleagues identified light-activated inwardly cation channels channelrhodopsin-1 (ChR1) [41] and channelrhodopsin-2 (ChR2) [42] from unicellular algae *Chlamydomonas reinhardtii* successively, people started to pay attention to light-sensitive proteins in neuroscience. In the following years, five laboratories as pioneers first activated neurons independently by using ChR2 [43-47]. Since 2006 when Deisseroth et al. first termed this technique optogenetics [48], the field has emerged formally. One year later, Adamantidis et al. first controlled the behavior in a freely moving mammal by using ChR2 [49]. By 2010, two other light-sensitive proteins, bacteriorhodopsin (BR) and halorhodopsin (HR) also had been proven capable of modifying neuronal activity under illumination. They had actually been discovered much earlier than ChR2. BR was discovered from *Halobacterium salinarum* by Stoeckenius and Oesterhelt in 1971 [50], while HR was found from *Natronomonas pharaonic* by Matsuno-Yagi and Mukohata in 1977 [51]. Although with the ability to suppress cellular activity, effective inhibition requires high protein expression levels and high light power intensities due to low ion transport efficiency. In 2010, optogenetics was chosen as the method of the year in Nature Methods [52]. Since then, the field of optogenetics has been developed rapidly and the optogenetic toolboxes have been expanded largely to solve the limitations of natural light-sensitive proteins and meet the specific requirements of different applications (see also Section 1.2.3 and 1.3.2). Nowadays, optogenetics becomes a versatile technology not only in the field of neuroscience for understanding how the brain works and treating neurogenic disease, but also in other fields such as cardiac research [53-55], vision restoration [56-58], and stem cell research [59-61]. In recent years, optogenetic applications even have been extended from animal into plant research fields [62, 63].

1.2.2 Basic requirements of optogenetics

The general strategy of optogenetics includes: 1) selecting a specific light-sensitive protein of interest; 2) delivering genes encoding the light-sensitive protein to a specific cell type; 3) illuminating the target region by corresponding light with defined parameters; and 4) obtaining reliable resulting readouts of the optogenetic manipulation (**Figure 1.6**). Each part will be introduced in the following sections.

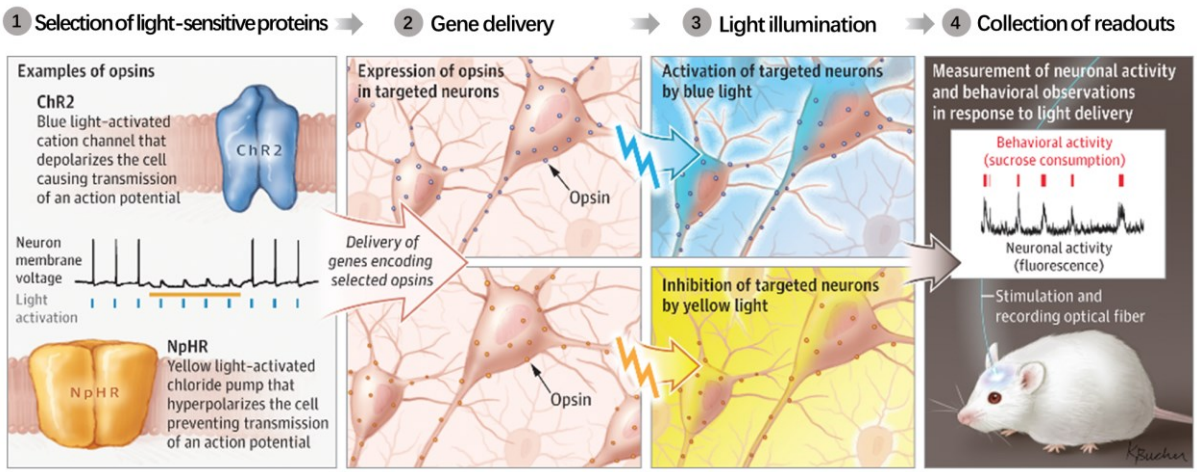

Figure 1.6 The general strategy of optogenetics includes four basic steps. Step 1, select specific light-sensitive proteins of interest. An excitatory ChR2 and an inhibitory NpHR (*Natronomonas pharaonis* Halorhodopsin) are shown as examples; Step 2, deliver genes encoding the light-sensitive proteins to targeted neurons; Step 3, illuminate the targeted cells with the corresponding wavelength of light. Here, the ChR2-expressing neurons are excited by blue light and the NpHR-expressing neurons are inhibited by yellow light; and Step 4, obtain reliable readouts of the optogenetic manipulation. Images adapted from [64].

1.2.2.1 Selection of light-sensitive proteins

Light is a vital cue for nearly all organisms to obtain energy and information from their environment. In nature, organisms have acquired different abilities to sense and make use of light via various light-sensitive proteins during evolution. These photosensitive proteins, also known as photoreceptor proteins, are existing in various kingdoms of life. They are mainly rhodopsins, light-oxygen-voltage (LOV) sensors, phytochromes, cryptochromes, xanthopsins, light-activated adenylyl cyclase (PAC) and UV-B receptors (UVR8). These light-sensitive proteins encompass chromophores such as retinal, bilin and FAD/FMN, which act as light sensors that can undergo conformational changes upon photon absorption. In certain cases, light can elicit signal transduction directly within the sensory proteins because they encompass both the light sensation and effector functions. This kind of light-sensitive protein can be used for modulating the membrane potential, for instance, the majority of microbial rhodopsins. In other cases, the triggered signals need to be propagated from the sensors to effectors that are located at other domains of the proteins or even to other interacting proteins. These light-sensitive proteins are usually used for modulating cellular signaling pathways by activating a series of enzymes. LOV sensors, phytochromes and animal rhodopsins are examples of this type of protein [65].

Among various light-sensitive proteins, rhodopsin families are one of the most powerful and widely used optogenetic actuators. Their absorption wavelengths of light are in the range of visible light (390-700 nm). Rhodopsin is the complex of an opsin and a retinal chromophore. Retinal is a vitamin A derivative, acting as a photon-absorbing cofactor. Opsin is an integral membrane protein with seven transmembrane domains, serving as an apoprotein. The retinal

covalently binds to a conserved lysine residue located at helix seven (TM7) via a protonated retinal Schiff base ($RSBH^+$). According to their features, rhodopsins are classified into two major types, microbial rhodopsins and animal rhodopsins (**Figure 1.7**). Microbial rhodopsins, also known as Type I rhodopsins, are found in microbial organisms including bacteria, archaea, algae and fungi where they perform photosensory functions for navigating towards or away from light. The majority of microbial rhodopsins discovered in nature are ion channels and ion pumps. The ion channel-type rhodopsins are cation channelrhodopsins (CCR; e.g., ChR1 and ChR2) and anion channelrhodopsins (ACR; GtACR1 and GtACR2). Ion pump-type rhodopsins are BR (outward H^+ pump), HR (inward Cl^- pump), Krokinobacter rhodopsin 2 (KR2, outward Na^+ pump) and Xenorhodopsin (XeR, inward H^+ pump). These microbial rhodopsins utilize all-trans retinal, which isomerizes into 13-cis retinal upon light illumination. This isomerization leads to ion flux through ion channels or ion pumps. At light-off the 13-cis configuration thermally reconverts to the all-trans configuration rapidly. During the whole process, the retinal keeps associating with the opsin via the covalent bond. Therefore, the entire process is named photocycle. Actually, in addition to the well-known ion channels and ion pumps mentioned above, the minority of microbial rhodopsins are signaling/enzyme-type such as rhodopsin-guanylyl cyclase (RhGC) and rhodopsin-phospho diesterase (RhoPDE) [66]. Animal rhodopsins are Type II rhodopsins, which are actually G-protein-coupled receptors (GPCRs). Upon light absorption, 11-cis retinal isomerizes into all-trans retinal, initiating cellular signaling cascades by transducing signals to corresponding intracellular effectors, which is different from the ion flux induced by microbial ion channels or pumps. After isomerization, the all-trans retinal is released from the opsin apoprotein and a new 11-cis retinal is needed for the next light response. Thus the process is named photobleaching. Type II rhodopsins are discovered in vertebrate cells. They play roles primarily in vision, circadian rhythm and pigment regulation. The engineered vertebrate rhodopsin can be used to control biochemical reactions in cells. For instance, optoXRs are produced by replacing the intracellular loops of bovine rhodopsin with the intracellular loops from GPCRs, which are useful for the optical control of G protein signaling. Animal and microbial rhodopsins have structural and mechanistic similarities but share low sequence homologies [67-69].

Significantly, ion channel-type and ion pump-type microbial rhodopsins are the most commonly used optogenetic actuators for modulating membrane potential owing to their advantageous properties. First, they are single-component tools that unify both the sensor and effector domains, so it is convenient to use and modify. Second, the genes encoding the rhodopsin proteins are small, thereby it is easier to deliver these genes into target cells. Third, the amount of all-trans retinal is sufficient in mammalian neurons for optogenetic manipulation without exogenous retinal supplementation. Moreover, the efficiency of ion channels is higher than that of ion pumps, as ion channels passively transport multiple ions in a single photocycle while ion pumps actively translocate only a single ion every time. Therefore, the most common channelrhodopsin ChR2 is chosen as the optogenetic actuator used in this work and it will be focused on in Section 1.3.

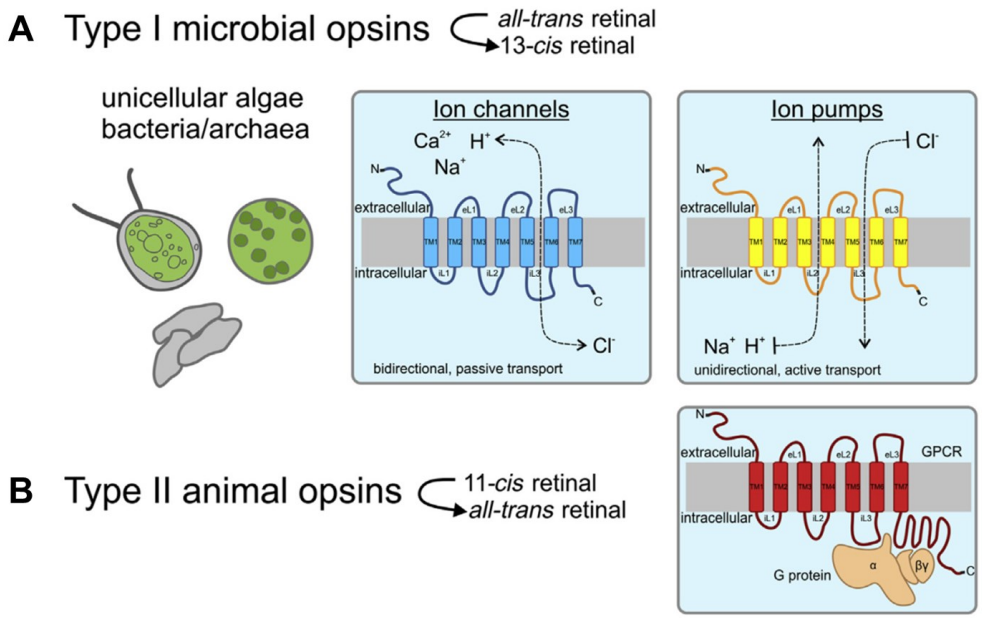

Figure 1.7 Two types of rhodopsins. (**A**) Type I microbial rhodopsins mainly including ion channels and ion pumps isomerize all-trans retinal into 13-cis retinal upon light illumination. (**B**) Type II animal rhodopsins, a type of G-protein-coupled receptors, transform 11-cis retinal into all-trans retinal. Image adapted from [70].

1.2.2.2 Gene delivery

Introducing light-sensitive proteins into target cells is crucial for optogenetic manipulation. For this, different gene delivery methods can be used, mainly including transfection, viral gene transfer, electroporation and utilization of transgenic animal lines. Each method has its advantages and drawbacks in terms of efficiency, expression level, cell viability, cost and reproducibility. First, there are lots of commercial offerings for chemical transfection based on different mechanisms such as calcium-phosphate/DNA co-precipitation, cationic polymer and lipid. Transfection usually can produce high levels of expression in most cell types and the results are reproducible. But, one drawback is that the transfection efficiency in primary and non-dividing cells like neurons is relatively low. Thus, for non-neuronal cell types in this work, a chemical transfection approach with FuGENE® HD Transfection Reagent was applied, see more in Section 2.3.2. Also, this method is not suitable for *in vivo* gene delivery [71, 72]. Second, viral expression systems produce consistently high efficiency and can be used for delivering genes into primary and non-dividing cells, and even are compatible for *in vivo* gene delivery. But the payload length of virus vectors is usually small, which limits their applications for delivering large genes. Besides, this approach requires the preparation of new virus particles for each construct, which is time-consuming. Moreover, working with viruses needs additional biosafety precautions although most viruses in use are replication incompetent [73, 74]. Third, electroporation can be used for delivering genes into the cytoplasm, producing high transfection efficiency in cells. *In utero* electroporation (IUE) has been widely used and developed to target specific cell types. But this high efficiency is often achieved at the cost of high cell death. Also, the parameters for different cell types need to be optimized. However,

for postmitotic cells like neurons, the efficiency is comparably low [75, 76]. Nucleofection is an improved electroporation technique, which utilizes short high-voltage pulses to transfer genes into the nucleus, resulting in high transfection efficiency [77, 78]. The combined application with an optimized cell-specific buffer ensures high cell survival and viability. A major drawback is that the nucleofection can be applied only to freshly isolated neurons in suspension, which limits their applications for the research on mature neurons. In addition, the cost is relatively expensive because of the equipment and reagents. Nevertheless, considering its significant advantages for *in vitro* application in primary neurons, this approach was adopted to deliver genes into primary neurons in the present work, and the detailed procedure is seen in Section 2.3.1. Fourth, transgenic animal lines expressing opsin genes under different promoters such as the Thy-1 promoter have been developed [79, 80]. They can be used to restrict gene expression to a specific cell type *in vivo*. However, some promoters produce an insufficient expression that is unable to achieve optogenetic control. Cre recombinase-based mouse lines combined with the utilization of a viral vector carrying a double-floxed inverted opsin gene are developed, in which only the cells expressing Cre recombinase can activate the opsin gene [81, 82]. These approaches are effective ways to introduce genes *in vivo*. Overall, these different gene delivery methods confer light-sensitive properties on target cells, making it possible to conduct optogenetic manipulation under various conditions.

1.2.2.3 Light illumination

Precise optogenetic manipulation relies on a controllable light delivery system. A primary experimental consideration is to choose the proper wavelength of light source matched to the activation spectrum of the optogenetic tool of interest. Various light sources are available in optogenetics currently [83, 84]. For *in vitro* illumination, filtered light from mercury arc lamps is used at the earliest but with limitations in on/off gating light and is not suitable for *in vivo* applications due to the low optical fiber coupling efficiency. Besides, lasers are attractive light sources for optogenetic applications owing to their narrow bandwidth (< 1 nm) and low divergence property, but with a relatively high cost. The laser with proper wavelength is chosen as the light source in this work and see details in Section 2.6. Light-emitting diodes (LEDs) are also an appealing option because of their simplicity, low cost, low power requirements and narrow spectral tuning. Both lasers and LEDs can be directly coupled to the microscope light path to illuminate cultured cells or acute brain slices. For *in vivo* illumination, more specialized approaches are needed. If illumination regions are superficial cortical neurons, small LED lamps can be mounted directly on top of the target region. If illumination regions are deep brain tissues, light can not be delivered to the target region directly since brain tissue scatters light. The common strategy is using a lightweight and flexible optical fiber to deliver light to the target region. One end of the optical fiber cable is inserted into a cannula that is implanted in the skull to the target region, and the other end is connected to a light source, usually a laser or a LED. However, some disadvantages such as heat generation, hindrance of completely free movement and the low efficiency of LED-optical fiber coupling weakens their applications.

But nowadays implantable wireless LED devices make certain limitations less of a problem [85, 86].

1.2.2.4 Collection of readouts

The final step of optogenetic manipulation is to read the outcome of optogenetic inputs from the targeted cells, tissues and organisms, which could be recorded by electrodes, fluorescence-based biosensors, magnetic resonance or behavioral tests [39, 87, 88]. First, the most common recording is from electrodes, which can be used to measure membrane electrical signals in response to illumination [89, 90]. According to the placement of the electrode in the sample, the recordings can be divided into intracellular and extracellular recordings. In the intracellular recording, the electrode such as a patch or sharp microelectrode is attached or inserted into the cell, and the recording is from inside of the cell. This recording can provide precise information about the generated electrical signals including local potentials and the signals of ion channels. However, it can not provide effective information on network connectivity as it can only be applied to individual cells, and can not be used for long-time recordings due to the mechanical instability and damage to the cell. In the extracellular recording, the electrode is placed outside the cell near the membrane, and the recording is from the outside of the cell, so it would not produce a negative effect on the cell's health. However, the extracellular recordings are unable to detect the subthreshold signals. The advanced development of multiple electrodes such as tetrode and multielectrode array (MEA) makes it possible to record the activities of multiple cells at the same time, so it is suitable for analyzing neural network connectivity. But this recording approach lacks spatial flexibility as the electrodes are fixed. Second, fluorescence-based biosensors such as voltage-sensitive dyes, genetically encoded calcium indicators and genetically encoded voltage indicators could also be applied to record neuronal activities arising from optogenetic control [91, 92]. This recording can achieve more spatial distribution information than electrode-based electrophysiology, but with much lower temporal resolution. One important thing to be taken into account for this all-optical control and readout is to select appropriate light without interference from spectral overlap. Third, blood oxygenation level-dependent (BOLD) functional magnetic resonance imaging (fMRI) is also used in combination with optogenetic manipulation [60, 93, 94]. The foundation is that electrically active neurons have a higher metabolism rate and consume more energy, which can be measured through blood oxygenation-level in the brain. This noninvasive approach is valuable for exploring functional connectivity in the view of the whole-brain. Moreover, morphological changes or animal behaviors are also a kind of readout of optogenetic manipulation [49, 73, 95], these readouts are more straightforward than other approaches mentioned above. These approaches are suitable for studying, for instance, the underlying mechanism related to morphology, or how a specific neural activity results in a behavioral response. The main readout approach used in this work is the electrode recording by using the patch clamp technique that will be focused on in Section 1.5.

1.2.3 The problems with using wild-type optogenetic actuators

The innovation of optogenetics has profoundly transformed the field of neuroscience. Now it is possible to conduct optogenetic manipulation in genetically defined populations of neurons by using genetic methods such as a specific targeting promoter or a Cre recombinase-based system. Also optogenetic control in functionally defined neurons can be achieved based on circuit connectivity, that is, projection targeting [18, 39, 96]. However, as the wild types of optogenetic actuators are usually distributed throughout the cell, we are still facing the following problems. The first one is the excess and unphysiological activation [97]. The indiscriminate distribution of optogenetic actuators can achieve effective control of the overall activity of neurons. But in neurons it is usually the dendrite that receives input signals from other cells, then the axon transmits these messages to the next cells. Therefore, physiologically, it is not all the compartments of neurons are activated simultaneously. Current light delivery techniques have allowed targeting light to a small enough area, but the off-target effects exist when stimulating a specific neural circuit, which is caused by dense neural networks. For example, if a given neuron expresses a wild type of optogenetic actuator, since the cell body is closely packed with neurites that may originate from distant and functionally unrelated neurons, optogenetic stimulation on the cell body of the given neuron may also activate the packed actuator-expressing neurites. But if the actuator is only expressed in the cell body, the packed neurites will not be activated simultaneously. Thus, if optogenetic actuators could be specifically targeted to certain subcellular compartments, such as axons or dendrites, while maintaining currents, specific circuits could be manipulated without disruptions due to effects on neighboring cell structures. Restricting the expression of actuators in a specific subcellular compartment enables more precise optogenetic manipulation. In a word, the final specificity necessary would be the subcellular targeting of the actuator.

Various subcellular targeting approaches have been adopted to construct subcellular optogenetic tools for controlling not only the membrane potential but also many other cellular actions like gene expression or organelles' localization [98, 99]. The general strategy is to utilize short sequence motifs that provide specific sorting, retention, anchor, or fusion information. For example, the ankyrin G-interacting domain is usually used for AIS targeting, and synaptophysin is applied for presynaptic cytosol targeting. However, problems induced by subcellular expression of optogenetic actuators for membrane potential control are still existing. For instance, AIS targeting of ChR2 mediated by II-III intracellular loop of sodium channel impairs neuronal firing due to its interference with the localizations of endogenous ion channels [100-102]. Motifs from synaptic vesicles or lysosomes affect the function of ChR2 [103]. So far, canonical subcellularly-localized actuators for membrane depolarization have not been established. Therefore, this work aims to construct subcellularly-localized optogenetic actuators for controlling the membrane potential mainly based on a classic channelrhodopsin which will be focused on in Section 1.3, and the targeting strategy utilized will be introduced in Section 1.4.

1.3 Channelrhodopsin-2 (ChR2)

1.3.1 The basics of ChR2

1.3.1.1 The mechanism of ChR2-induced membrane depolarization

Channelrhodopsins-2 (ChR2), a typical microbial rhodopsin, is currently not only the best studied channelrhodopsin but also the most commonly used optogenetic tool for membrane depolarization. ChR2 is found naturally in the unicellular algae *Chlamydomonas reinhardtii* where it serves as a sensory photoreceptor in its eyespot, overlapping with part of the plasma membrane. Upon large or abrupt changes in light intensity, ion influx happens across the ChR2, driving flagellar beating to navigate the algae towards or away from light [104]. Specifically, naturally occurring ChR2 (737 aa (amino acids)) consists of an N-terminal seven transmembrane helices (1-315 aa) and a C-terminal tail domain (316-737 aa) (**Figure 1.8**). It is found that only the transmembrane domains are needed for light manipulation since this region contains a unified light sensor and ion channel functionality [42], whereas the C-terminal domain is relevant for channelrhodopsin targeting and protein-protein interactions in the alga. The chromophore retinal covalently binds to Lys^{257} on TM7 of ChR2 via $RSBH^{+}$. The maximum absorption wavelength of light for ChR2 is around 470 nm, namely blue light. In response to blue light, the retinal isomerizes from all-trans to 13-cis configuration, which triggers a side-flip of the transmembrane helix. Then channel opens and cations inflow across the membrane, inducing membrane depolarization (**Figure 1.8B**). The ion channel is nonselective towards cations and they are mainly proton, sodium, potassium, and calcium in descending order under physiological conditions. The sodium is evaluated to be about 10^5-10^6 times lower than the proton conductance, while it is around eight times higher than calcium conductance [105].

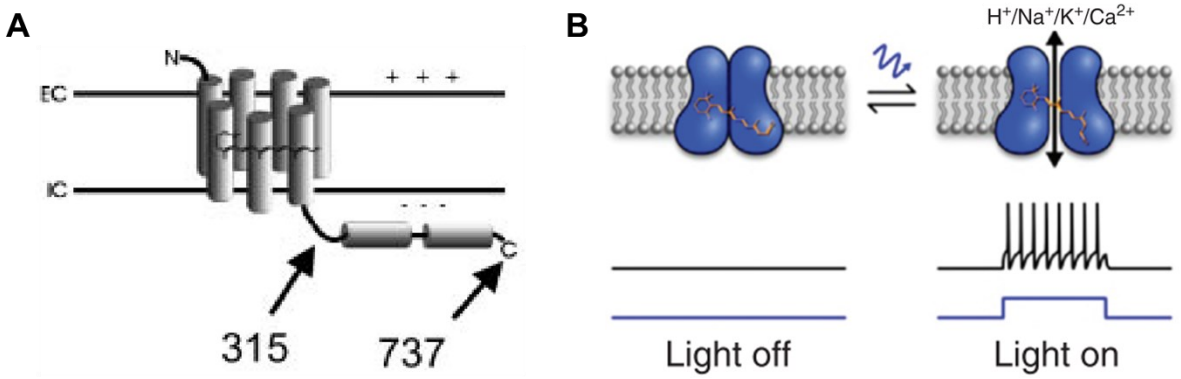

Figure 1.8 The basic structure and function of channelrhodopsin-2 (ChR2). (**A**) Scheme of the structure of ChR2 that consists of an N-terminal seven transmembrane helices (1-315 aa) and a C-terminal tail domain (316-737 aa). A retinal binds to the transmembrane region. (**B**) In response to blue light, the retinal photoisomerizes from all-trans to 13-cis configuration and the channel opens, depolarizing the cell. Images adapted from [42] and [106].

1.3.1.2 The photocurrent of ChR2

The photocurrent of ChR2 is the sum of migrated charges through the open ChR2 at a specific membrane potential in response to blue light. The photocurrent depends on the number of open channels and the conductance of a single channel at a given potential [107, 108]. The former is related to the number of expressed ChR2 in the illuminated area, received photons, and the likelihood of a ChR2 absorbing a photon and successfully converting the channel from a closed state to an open state, namely quantum efficiency, which is hard to optimize. The latter is determined by its ion permeation (see Section 1.3.1.4) which can be modified through genetic engineering (see Section 1.3.2). The conductance of wild-type ChR2 is evaluated to be 50-250 fS [109].

The configuration of a typical ChR2 photocurrent elicited by blue light is shown in **Figure 1.9A**, which displays two obvious amplitudes. In response to blue light, a peak current (I_p) is triggered first, then it decays fast to a steady-state current (I_{ss}). The process of photocurrent transition from the peak to steady state under continuous illumination is called desensitization or inactivation and the corresponding time constant is denoted as τ_{des} or τ_{inact}. The level of desensitization of wild-type ChR2 is high, up to 80% under physiological conditions. This high level of desensitization is the main drawback of ChR2. Two other kinetics are indicated in the figure as well. The time constant of channel opening at the beginning of the light pulse is denoted as τ_{on} and the time constant of channel closure at the end of the light pulse is denoted as τ_{off}. ChR2 has a rapid open rate and a moderate closing rate. These photocurrent properties are important for the precise depolarization performance by using this channelrhodopsin.

1.3.1.3 Simplified photocycle of ChR2 with key intermediates

The cyclic process of various ChR2 intermediates under different light conditions is the photocycle of ChR2. **Figure 1.9B** shows several key intermediates in the photocycle of ChR2. D470, which is non-conducting but excitable, is a long dark-adapted ChR2 with an all-trans retinal. Upon blue light illumination, D470 immediately converts to a nonconductive early intermediate P500 and a transient intermediate P390 in sequence. Then the channel opens and becomes a conductive intermediate P520, which is in equilibrium with earlier nonconducting intermediate P390. In intermediates P500, P390 and P520, the bound retinal is in a 13-cis configuration. Next, the retinal isomerizes back to an all-trans configuration and the channel converts to a nonconductive intermediate P480. After a relatively long dark period, the channel thermally returns to the initial ground state. Alternatively, if the interpulse time is short, the P480 can photochemically convert to P500 since the P480 is photoactive to blue light. In addition, the P520 can return to D470 directly without going through P480 under green light illumination.

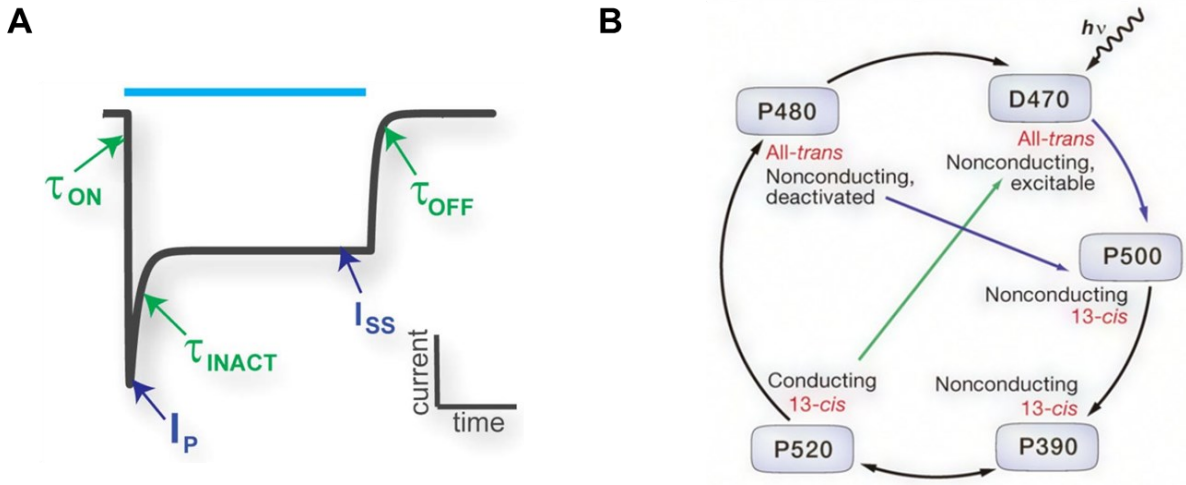

Figure 1.9 The photocurrent and simplified photocycle of ChR2 in response to blue light. (**A**) A photocurrent (black line) is elicited in response to blue light (light blue bar). Two current amplitudes (in dark blue): peak current (I_p) and steady-state current (I_{ss}), and three kinetics (in green): on (τ_{on}), inactivation (τ_{inact}) and off (τ_{off}) time constant, describe the photocurrent. (**B**) A simplified photocycle of ChR2 with key intermediates D470, P500, P390, P520 and P480. Images adapted from [110] and [111].

1.3.1.4 Ion permeation pathway of ChR2

Understanding the ion permeation of channelrhodopsin is important for optimizing its optogenetic performance, which has progressed largely since the high-resolution crystal structure in the dark state was solved by Hideaki E. Kato in 2012 [112]. It is mainly TM1, TM2, TM3 and TM7 that form the ion permeation pore (**Figure 1.10**). The charges of polar amino acid residues along the ion permeation pathway make the pore hydrophilic, which is critical to the properties of channelrhodopsin. There are two key positions along the hydrophilic ion pore. In the middle position is a central gate (**Figure 1.10E**) consisting of Ser^{63}, Glu^{90} and Asn^{258} that blocks water from the extracellular region in a dark state and serves as a selective ion filter. The other key position close to the intracellular membrane is named the inner gate, which is formed by Glu^{82} and Glu^{83} together with their hydrogen-binding partners His^{134} and His^{265}(**Figure 1.10C**). This gate closes the channel and prevents water flux from the intracellular bulk phase in the dark. It also plays a filter role in determining ion selectivity. Thus both gates are responsible for keeping the channel closed in a dark state and conformation changes are needed at these two sites to open the channel upon light illumination. Two glutamate resides, Glu^{123} and Glu^{253}, around the retinal binding pocket are also critical for the performance of channelrhodopsin since they are related to stabilizing the charge of the $RSBH^+$. Another two residues that are crucial to the kinetics of channel opening and closing are Cys^{128} and Asp^{156} [105, 113] (**Figure 1.10D**).

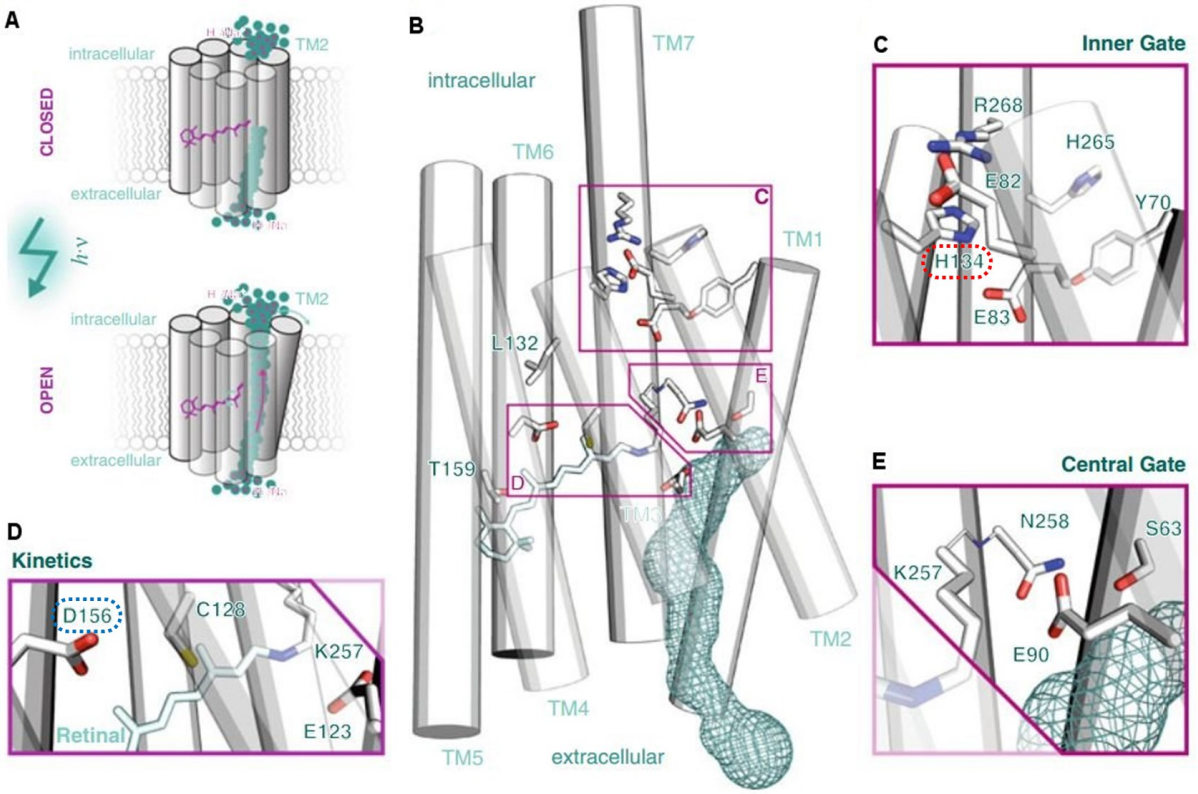

Figure 1.10 The crystal structure of channelrhodopsin with an emphasis on key positions. (**A**) Upon light illumination, dark-adapted ChR2 converts from a closed state (top) to an open state (bottom), triggering ion fluxes. (**B**) An overall view of the crystal structure of dark-adapted ChR2 with seven transmembrane helices (TM) and key amino acid residues. TM1, TM2, TM3 and TM7 form the ion permeation pathway. (**C**) A closer look into the inner gate along the ion permeation pathway. H134 residue is emphasized by a red dotted circle. (**D**) A closer look into the key residues around the retinal binding pocket that are relevant for channel kinetics. D156 residue is emphasized by a blue dotted circle. (**E**) A closer look into the central gate along the ion permeation pathway. Image adapted from [107].

1.3.2 The variants of ChR2

Mutations of the residues at key sites mentioned above can produce new ChR variants with different properties via structure-guided mutagenesis. For instance, the first mutant ChR2(H134R) with an enhanced stationary photocurrent is generated in this way [45]. As an actuator used in this work, it will be focused on in Section 1.3.2.1. Besides, other strategies such as genomic screening, chimeragenesis and molecular trafficking have also been used to generate new variants. The properties modified are mainly from these aspects; absorption spectrum, channel kinetics, ion selectivity and channel conductance. These variants discovered in various species in nature and the ones engineered artificially in the laboratory can achieve more specific control of optogenetic manipulations for different applications. For example, red-shifted ChRs such as VChR1 [114], C1V1 [115], ReaCh [116], Chronos and ChrimsonR [117] utilize light with higher tissue penetrability with fewer phototoxicity effects, which are useful for non-invasive light delivery. These red-shifted channelrhodopsins combined with blue light-sensitive channelrhodopsins enable two-color control of neuronal activities without crosstalk.

Ultrafast channelrhodopsins, like ChETA(E123T) [118] and ChEF/ChIEF [119], can elicit spikes at high rates (up to 200 Hz) but with limited photocurrents. These ultrafast channelrhodopsins usually involve mutations in amino acid residues that are related to stabilizing the protonated retinal Schiff base in the open state. After the removal of light, the channels transform back to the nonconducting state faster, accelerating the photocycle. This kind of variant is suitable in cases where a high stimulation frequency is desired to realize extremely fast temporal control of neuronal activity. In addition, step function or bi-stable opsins (SFOs) with rather extremely slow deactivation kinetics are generated by introducing mutation at C128 or/and D156 position(s). This is because these two residues also stay close to the retinal binding pocket and their mutations dramatically affect the channel photocycling. This kind of channelrhodopsin is suitable for controlling cellular activity in behavioural paradigms where the connection to a fiber optic would be burdensome. One of this type of variants used in this work, ChR2(D156C), will be introduced in more details in Section 1.3.2.2. Moreover, certain variants have a different ion selectivity compared with wild-type ChR2. For example, calcium translocating channelrhodopsin CatCh^{+} with L132C and T159C/T159S mutations [120] conducts increased calcium by 1.6 times, which can be used in cardiomyocytes. In some cases, mutations even convert ChR2 from a cationic conductance to an anionic conductance, like iC1C2 [121], iC++ [122], ChloC [123] and iChloC [124] which conduct chloride, and these variants can be used to silence neurons under physiological conditions.

1.3.2.1 ChR2(H134R)

The first channelrhodopsin used in this work is ChR2(H134R), which is generated by replacing histidine (H) with arginine (R) at site 134 on TM3. The original consideration was that H134 corresponds to D96 in bacteriorhodopsin, and this residue is crucial for proton pumping as it reprotonates the retinal Schiff base [45] (**Figure 1.10C**). As the first mutant of ChR2, it has been largely favored since its discovery [70, 125, 126] partly owing to the wide commercial availability of virus vectors carrying this encoded gene and corresponding transgenic animals, apart from its excellent performance. As mentioned above (Section 1.3.1.4), His^{134} interacts with one of the conserved glutamates (Glu^{82}) within the inner gate along the ion-conducting pore of ChR2, so it plays a critical role in the performance of ChR2. Although residue change at this critical site does not change the activation spectrum, it alters some properties of ChR2. Compared with wild-type ChR2, in response to blue light this variant produces a larger stationary photocurrent with a mild higher sodium/proton ratio (1.2), causing fewer side effects to the cell. The extent of desensitization, a major disadvantage when using natural ChR2 for optogenetic experiments upon continuous illumination, is slightly relieved. One drawback of this variant is the mutation slows down the off-kinetics slightly, making it less temporally precise in comparison to wild-type ChR2. Therefore, this variant is suitable for applications where a moderate stimulation frequency is desired, like in cardiac myocytes, since the firing rate of cardiomyocytes does not exceed 6 Hz under physiological conditions.

1.3.2.2 ChR2(D156C)

ChR2(D156C) is another variant of ChR2 used in the present work. It is also known as ChR2XXL, as it has extra high expression and a long open state. It is produced by replacing aspartic acid (D) with cysteine (C) at site 156, based on structure-guided mutagenesis [127] (**Figure 1.10D**). The Asp^{156} residue on TM4 and Cys^{128} residue on TM3 form a putative hydrogen bond which is referred to as a DC gate or DC pair. These two residues are highly relevant for channel gating and are critical determinants for the kinetics of channel closing. D156 acts as an internal proton donor, reprotonating the Schiff base in the photocycle [128]. Mutation of D156C enhances retinal binding affinity and obviously slows down the channel kinetics, which extends the open state lifetime leading to an increased light sensitivity, since slow channel closure makes activated channels stuck in the open state, and as a result, the responsiveness will be saturated at low light intensities. ChR2XXL provides currently the highest photostimulation efficiency [127]. Besides, it exhibits elevated photocurrents owing to its extra high expression level in cells. A disadvantage is its low temporal precision, but this makes it most suited for the prolonged induction of depolarization without continuous illumination [129, 130], solving the problems in some cases where light delivery or light intensity is a limiting factor. Furthermore, since the creation of ChR2XXL, it has been applied immediately in behavior investigations mainly in Drosophila such as circadian clock [131], locomotor behavior [130] and spatial learning [132]. Recently, its applications even have extended from animal to plant research fields [62, 63]. But the electrophysiological characterization of the channel has not been fully explored yet. Few studies are about the specific electrophysiological behaviors of the channel in response to different stimulation protocols, unlike comparable variants such as ChR2(C128A), ChR2(C128S), and ChR2(D156A) that are well explored [133-136].

1.4 Subcellular targeting

1.4.1 Membrane protein trafficking

Cells, especially polarized cells, distribute the membrane proteins to subcellular regions to establish and maintain morphological and functional properties. For example, in neurons, the precise subcellular distribution of components such as various ion channels, neurotransmitters and ankyrins plays a fundamental role in complex neuronal functions. In order to achieve exquisite subcellular compartmentalization, cells use various mechanisms, including polarized trafficking [137-140], endocytosis and transcytosis [141-143], diffusional restriction of the membrane [139, 144, 145] and local translation of messenger RNA [146-149]. Among them, polarized membrane trafficking is fundamentally important and it involves selective sorting, selective transport and selective fusion [139, 140]. In these processes sorting signals play key roles, which are some special short peptide sequences usually located at the C or N-terminus of transmembrane proteins. These sequences can direct proteins to the right destinations.

Selective sorting usually occurs at the trans-Golgi network (TGN) where cargo adaptors bind to the sorting signals of the cargo proteins. As a consequence, only proteins carried with the specific sorting signals can be concentrated in this process. Thus, these sorting signals help package cargo proteins into distinct vesicles at the TGN [139, 140]. Then, various vesicles move along microtubules towards different plasma membrane domains, being driven by motor proteins. Motor proteins are responsible for transporting cargos in cells by walking on the cytoskeleton utilizing energy from ATP hydrolyzation. Specific motors are bound to vesicles through cargo adaptors that bind with targeting motifs. Motor proteins kinesins and dyneins move along microtubules for long distance transport whereas myosin walks along actin filaments for local transport. Specifically, dyneins translocate vesicles towards the minus end of microtubules, while most kinesins move vesicles in the opposite direction. After reaching the destination, vesicles selectively fuse with the appropriate membranes and this process is mediated by the SNARE complex [150].

There are some similarities in the subcellular localization of membrane proteins between polarized epithelia and neurons. First, morphologically, for example, neurons differentiate and maintain the somatodendritic and axonal membranes, and AIS marks the boundaries between these two domains. Likewise, epithelial cells differentiate and maintain the basolateral and apical membranes, and a tight junction separates these two regions. Further, the principles of sorting are conserved between polarized epithelia and neurons to a certain extent. Some basolateral proteins such as transferrin receptor (TfR) and low density lipoprotein receptor (LDLR) are somatodendritic proteins, whereas apical proteins such as γ-aminobutyric acid (GABA) transporter GAT-1 and influenza hemagglutinin (HA) are axonal proteins [151, 152]. It is reported that both somatodendritic and basolateral sorting signals are frequently located at the cytoplastic tails of transmembrane proteins, while axonal and apical sorting signals are usually at the extracellular or transmembrane domains of proteins [139, 153-157]. For instance, the basolateral and somatodendritic sortings of TfR both depend on its cytoplasmic targeting sequence [158, 159]. So far most of the known subcellularly plasma membrane-targeted optogenetic actuators have focused on utilizing the targeting motifs identified in neurons, such as the motifs from the myosin binding domain [160, 161], II-III loop sequence of sodium channel [101, 102] and voltage-gated potassium channel [162]. However, the sorting motifs found in epithelial cells are also potentially useful. Subcellularly-localized optogenetic actuators constructed by using this kind of motifs probably can be used not only in neurons, but also in non-neuronal cell types like epithelia. Despite this often-ignored application, subcellularly-localized optogenetic actuators are also actually useful for studying biological processes like controlling ionic currents across the epithelium. Moreover, it is also interesting to figure out how a specific targeting motif directs the locations of proteins in different polarized cells.

A variety of targeting motifs are proved effective for the subcellular localization of membrane proteins [139, 163, 164]. In this project, two different types of targeting sequences are selected as the motifs to be used, primarily based on their excellent subcellular targeting effects in

epithelial cells. One is from cytoplasmic tail of type II rhodopsin, and the other one is tandem repeat from human mucin. For the former one, another consideration is that the type II rhodopsin and channelrhodopsin both belong to the rhodopsin protein. If the cytoplasmic tail sequence can target type II rhodopsin to a subcellular region, it is also likely to target the type I rhodopsin - channelrhodopsin - to a subcellular compartment. For the latter one, tandem repeats have their own unique characteristics, and they are interesting and challenging sequences to be studied. These two targeting motifs will be introduced in detail in the following sections.

1.4.2 Targeting motif from the cytoplasmic tail of rhodopsin

Retinal cells are the photoreceptors in vertebrates. They contain less than 2% cone cells and about 70% rod cells, which are highly differentiated cells consisting of the cell body, rod inner segment (RIS), rod outer segment (ROS) and synaptic terminal. RIS contains various organelles such as mitochondria, endoplasmic reticulum (ER) and Golgi complex, producing essential materials to maintain the fundamental functions of cells. ROS contains rhodopsin and auxiliary proteins. Here, the rhodopsin is a seven-TM GPCR protein (type II rhodopsin), which is responsible for detecting photons. Subsequently, the light signals are rapidly transduced and amplified by auxiliary proteins. The apoprotein opsin is synthesized and processed through the ER-Golgi-TGN-post Golgi pathway in RIS, then trafficked to the internal disks of ROS with high fidelity [165-167]. The rhodopsins are highly concentrated in the bilayered disk membranes of ROS. It is reported that the vectorial delivery of rhodopsins to the ROS is related to its C-terminal region [165, 168, 169]. The terminal amino acids from the cytoplasmic tail of

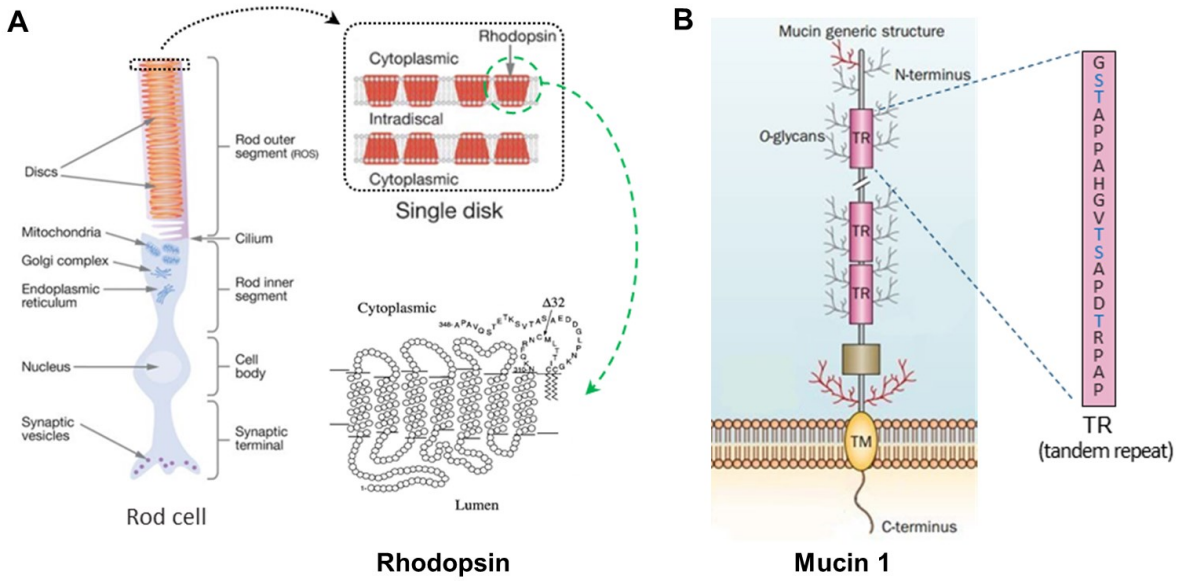

Figure 1.11 The targeting motifs used in this work. (**A**) A targeting motif consists of 32 amino acids from the cytoplasmic tail of human rhodopsin, which is located at the rod outer segment of rod cells. (**B**) A targeting motif, tandem repeat (TR), from the ectodomain of human mucin 1. Each TR consists of 20 amino acids with five Ser/Thr residues serving as sites for O-linked glycosylation. Image adapted from [170, 171] and [172].

rhodopsin is an apical sorting signal and it is sufficient to redirect the basolateral membrane protein CD7 (cluster of differentiation 7) and cytosolic protein glutathione S-transferase to the apical surface of Madin-Darby canine kidney (MDCK) cells, a typical epithelial cell [171]. Removal of the last 32 amino acids abolished the apical targeting. Besides, the sequences in the cytoplasmic tail are highly conserved among different species [173]. Thus, it is proposed to utilize this apical targeting sequence (**Figure 1.11A**) to construct a subcellularly localized optogenetic actuator.

1.4.3 Targeting motif from tandem repeats of mucin

Human mucin1 (MUC1) is a sialylated transmembrane glycoprotein in glandular epithelial cells, and its large highly glycosylated extracellular domain forms a rod-like structure [174, 175]. An apparent feature of the protein is the variable number of tandem repeats in the extracellular region. Tandem repeats (TR) are contiguous regions in which the same DNA sequences are repeated multiple times in order. In human MUC1 every TR consists of 20 amino acids (GSTAPPAHGVTSAPDTRPAP) with five Ser/Thr residues serving as sites for O-linked glycosylation with GalNAc [176, 177]. MUC1 is restricted to the apical surface of the normal glandular epithelium of many organs such as the breast, stomach and salivary. It is shown that the core-glycosylated mucin-like repeats act as an apical targeting signal, contributing to the polarized localization [178, 179]. Specifically, the apical delivery was affected after deleting the TR from wild-type MUC1, and the TR could redirect basolateral protein Tac (interleukin-2 receptor α subunit) to the apical side in polarized epithelial cells. Besides, the blocker against core O-glycan synthesis obstructed the apical delivery of the tandem repeats [178]. Therefore, it is also suggested to use this apical targeting motif (**Figure 1.11B**) to construct new optogenetic actuators in this work.

1.5 The patch clamp technique

The patch clamp technique is one of the main tools for evaluating cellular electrical excitability and the properties of ion channels in electrophysiological research. Shortly, it is achieved by gently attaching a micropipette onto cell membrane followed by applying a suction, so that a patch of cell membrane can be isolated electrically and clamped. The rudiment of patch clamp technique was created in 1952 by Alan Lloyd Hodgkin and Andrew Fielding Huxley who first measured membrane potential with crude glass electrodes to explain action potential [7]. In 1976, Erwin Neher and Bert Sakmann first measured single channel currents by sealing the large-bore pipettes to the cell membrane [180, 181]. In 1981, Hamill et al. refined this technique, enabling people to record currents with high resolution in cells or cell-free membrane patches [182]. Since then, the patch clamp technique has received a lot of attention and widely developed.

Nowadays, there are five basic types of patch clamp recording configurations developed, which are cell-attached configuration, whole cell configuration, perforated configuration, inside-out

configuration, and outside-out configuration [183]. In the cell-attached configuration, the pipette is sealed to the cell membrane, which keeps intact during the recording (**Figure 1.12A**). If the cell membrane is ruptured by applying a strong suction, the electrolyte solution in the pipette is continuous with the interior of the cell, and this is the whole cell configuration (**Figure 1.12B**). If the perforated membrane is achieved by supplementing pore-forming antibiotics in the pipette solution instead of rupturing the membrane by suction, this is the perforated configuration. If the pipette is retracted following the establishment of cell-attach configuration, the membrane around the pipette tip will be excised and the interior side is exposed to the bath solution, which is an inside-out configuration. If the pipette is retracted following the establishment of the whole cell configuration, the torn membrane can reseal the pipette tip, with the exterior membrane side exposed to the bath solution, and this is the outside-out configuration. These techniques can be used for different electrophysiological applications, and certain configurations may have preferable advantages over others for a specific application. For instance, the cell-attached configuration is favorable for evaluating the electrophysiological properties of ion channels while keeping the cell intact, but can not directly control the intracellular environment. The perforated configuration can be used to investigate the regulation of ion channels mediated by intracellular signaling pathways since this method retains the large molecules inside the cell. Therefore, investigators should choose the most suitable method according to their experimental purposes.

Whole cell patch clamp is most widely used for electrophysiological characterization, and it is also adopted in this work. Hence, the general principle is elaborated here, and the practical experimental procedures in detail are presented in Section 2.5. Generally, a recording electrode is inserted into a glass pipette containing electrolyte solution, while a reference electrode is placed in the extracellular patch solution. When the fire-polished glass micropipette tip contacts the cell surface membrane, a high sealing resistance, gigaohm, is formed between the pipette tip and cell membrane so that there is nearly no leaky current flowing through the pipette tip. Then the patched membrane is ruptured by a suction, leading to pipette solution connected with the intracellular solution directly. Therefore, any current or potential changes within the cell will be recorded by the recording electrode, which is connected to an ultra-sensitive amplifier and a feedback loop that allows setting the potential or current to a desired value (**Figure 1.12C**). Thereby the whole cell patch clamp is suitable for recording the summed activity of all channels expressed in the target cell, unlike cell-attached, inside-out and outside-out configurations that can be used for investigating the activity of a few or even a single channel. Two types of patch clamp modes could be used. One is voltage clamp mode, which is recording the current fluxing through cell membrane under a constant voltage. This could be used, for example, to study voltage-gated ion channels. The other one is current clamp mode, which is recording the voltage across cell membrane when injecting a constant current. This could be used, for instance, to detect the resting membrane potential or monitor spontaneous action potentials. Both of them are involved in this work. Besides, there are several advantages of the whole cell patch clamp. For example, the signal recording has a high signal-to-noise ratio as a

result of the implementation of a gigaseal that reduces the background noise significantly. Also the configuration can be performed in various samples such as cultured cells and brain slices. Another merit is that it can measure cell membrane capacitance, which is impossible by using other configurations. Furthermore, the whole cell configuration is powerful especially when combined with other approaches such as optogenetics or pharmacology, as it allows the study of how a specific manipulation (for example, light illumination or drugs) affects the electrical function of a cell or channels in real-time. Overall, the whole cell patch clamp is a versatile tool for lots of applications and the range is still expanding.

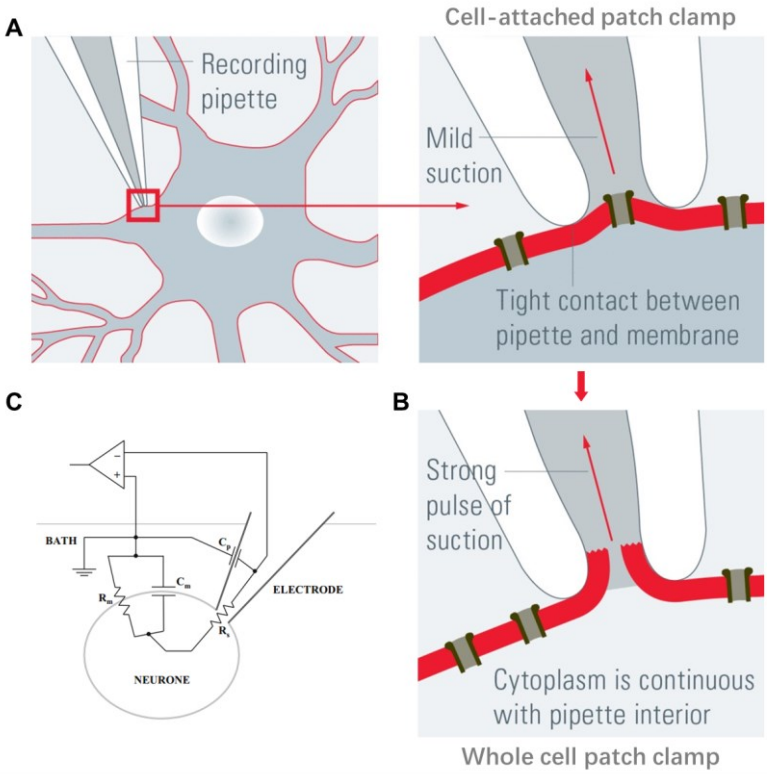

Figure 1.12 The whole cell patch clamp technique. (**A-B**) The basic process to establish the whole cell configuration. Initially, the micropipette is attached to the cell surface by applying a mild suction to create a tight contact (> 1 GΩ, gigaseal) between the pipette and the plasma membrane, which forms a cell-attached configuration (A). Then, a strong suction is applied to rupture the plasma membrane, forming the whole cell configuration where the cytoplasm is continuous with micropipette interior **(**B). (**C**) The equivalent electronic circuit of the whole cell patch configuration. The main components are pipette capacitance (C_p), series resistance (R_s), membrane capacitance (C_m) and membrane resistance (R_m). Images adapted from [184] and [183].

2 Materials and methods

This chapter aims to present detailed information about the experimental techniques and protocols involved in this work. First, the detailed processes of constructing two types of optogenetic actuators by using genetic engineering are provided (**Section 2.1**). Then, the cell culture of different cell types used (**Section 2.2**) and the corresponding gene delivery methods (**Section 2.3**) are presented, as well as the immunofluorescence staining in polarized cells to figure out the subcellular localization of the constructed actuators (**Section 2.4**). Next, the patch clamp technique (**Section 2.5**) and the optogenetic manipulation (**Section 2.6**) are described, followed by the live-cell imaging for observing the proteins trafficking in cells (**Section 2.7**). Finally, the data analysis methodology is introduced (**Section 2.8**).

2.1 Construct optogenetic actuators

2.1.1 TO-ChR2opt-mKATE-AT

ChR2opt is an optimized version of ChR2(H134R) for expression in rodents. Protein ChR2opt-mKATE was encoded by the plasmid TO-ChR2opt-mKATE (6833 bp) constructed in our lab previously. This plasmid was linearized with double restriction endonucleases NheI (FD0973, Thermo Fisher Scientific, Germany) and BamHI (FD0054, Thermo Fisher Scientific). The pure TO-ChR2opt-mKATE fragment was obtained from DNA gel extraction (see Section 2.1.4). After optimizing codons for rodents according to the codon usage database, the double fragments of apical targeting motif containing 32 amino acids from the cytoplasmic tail of human rhodopsin were synthesized by a synthetic biology company (Eurofins, Germany) and was named AT (Apical Targeting). In order to facilitate final DNA assembly, appropriate overlapping ends were designed and flanked on the two sides of AT sequence. The AT fragment was amplified by using PCR with designed primers (see Section 2.1.3) and purified from DNA gel extraction (see Section 2.1.4). In order to avoid interference from adjacent constructs, some amino acids were inserted as a spacer between mKATE and AT. These two fragments, the linearized TO-ChR2opt-mKATE fragment and AT fragment, were assembled by using DNA seamless cloning (see Section 2.1.5). The results were confirmed by DNA sequencing and restriction enzyme digestion.

2.1.2 TO-TR-ChR2XXL-YFP

ChR2XXL (a gift from Dr. Shiqiang Gao) is a D156C variant of ChR2. In order to visualize this protein, a yellow fluorescent protein (YFP) was tagged to its C-terminus, generating the fused protein ChR2XXL-YFP. The ChR2XXL-YFP was encoded by plasmid psc-hSyn-ChR2XXL-YFP (6593 bp) constructed in our lab previously by Dr. Lei Jin [185]. The ChR2XXL-YFP fragment was amplified from this plasmid through PCR (see Section 2.1.3). To facilitate final DNA assembly, appropriate overlapping ends were designed between

adjacent fragments when preparing individual DNA fragments. After performing codon optimization with manual adjustments to code synthesizable DNA, mucin fragments with different tandem repeats flanked with overlaps were synthesized into plasmids as Strings DNA Fragments by synthetic biology companies. Each tandem repeat includes 20 amino acids, which are GSTAPPAHGVTSAPDTRPAP. The subclone encoding 5 tandem repeats (TR5) was synthesized by Eurofins and the subclones encoding TR10 and TR15 were synthesized by Thermo Fisher Scientific. These three TR fragments along with their overlaps were amplified by PCR (see Section 2.1.3). The vector pcDNA4/TO was linearized with the restriction enzyme BamHI (FD0054, Thermo Fisher Scientific), serving as the backbone for generating new optogenetic actuators. The ChR2XXL-YFP fragment, different lengths of tandem repeats and the linearized vector were assembled by using DNA seamless cloning (see Section 2.1.5). In order to avoid interference from adjacent constructs, four amino acids (KLAT) were inserted as a linker between TR and ChR2XXL, and five amino acids (PAAAT) were inserted between ChR2XXL and YFP. The results were confirmed by DNA sequencing and restriction enzyme digestion.

2.1.3 Polymerase chain reaction (PCR)

Polymerase Chain Reaction (PCR) is a technique widely used to amplify a specific target DNA to a large amount within a few hours. The desired DNA sequences were amplified from either previously constructed plasmids or synthesized DNA sequences serving as DNA templates, as claimed in Sections 2.1.1 and 2.1.2. The AccuPrime™ *Taq* DNA Polymerase with high fidelity (5 U/µL; 12346086, Thermo Fisher Scientific) along with 10× AccuPrime™ PCR Buffer were used in the PCR systems. The 10× AccuPrime™ PCR Buffer contains 200 mM Tris-HCl (pH 8.4), 500 mM KCl, 15 mM $MgCl_2$, 2 mM dGTP, 2 mM dATP, 2 mM dTTP, 2 mM dCTP, AccuPrime™ thermostable protein, and 10% glycerin. The PCR reactions were performed in a thermal cycler (Eppendorf Mastercycler ep Gradient S PCR Thermal Cycler).

For the amplification of AT fragment, the forward primer was AGGCTCTGGCCTGAGATC and the reverse primer was GGATATCTGCAGAATTCCACC. The reaction system of PCR amplification is listed in **Table 2.1** and the corresponding procedures are listed in **Table 2.2**.

Table 2.1 The reaction system of PCR amplification for AT fragment.

0.20 µL	Template [APTargChR2opt (60 ng/µl)]
5.00 µL	10× AccuPrime PCR Buffer
0.13 µL	Primer Fwd (10 µM)
0.13 µL	Primer Rev (10 µM)
0.20 µL	AccuPrime *Taq* DNA polymerase
44.34 µL	H_2O
50.00 µL	Total volume

Table 2.2 The procedures of PCR amplification for AT fragment.

Initial denaturation	94℃	2 min	
Denaturation	94℃	30 s	
Annealing	53℃	30 s	30 cycles
Extension	68℃	21 s	
Final extension	68℃	10 min	

For the amplification of the ChR2XXL-YFP fragment, the forward primer was AAGCTTGCCACCATGGATTATGGAG and the reverse primer containing overlapping sequences (with the underline) with downstream linear vector was CGGCCGCCGGCAAGTAAGGATCCACTAGTCCAGTG. The reaction system of PCR amplification is listed in **Table 2.3** and the corresponding procedures are listed in **Table 2.4**.

Table 2.3 The reaction system of PCR amplification for ChR2XXL-YFP fragment.

0.30 μL	Template [psc-hSyn-ChRXXL-YFP (78 ng/μl)]
5.00 μL	10× AccuPrime PCR Buffer
1.00 μL	Primer Fwd (10 μM)
1.00 μL	Primer Rev (10 μM)
0.20 μL	AccuPrime *Taq* DNA polymerase
42.50 μL	H_2O
50.00 μL	Total volume

Table 2.4 The procedures of PCR amplification for ChR2XXL-YFP fragment.

Initial denaturation	94℃	2 min	
Denaturation	94℃	30 s	
Annealing	58℃	30 s	30 cycles
Extension	68℃	100 s	
Final extension	68℃	10 min	

For the amplification of three TR fragments including their overlaps, the forward primer was TAAGCTTGGTACCGAGCTC and the reverse primer was CTCCATAATCCATGGTGGC. The corresponding reaction systems of PCR amplification for TR5, TR10, and TR15 fragments are listed in **Tables 2.5**, **2.7**, and **2.9**, and the corresponding procedures are listed in **Tables 2.6**, **2.8**, and **2.10**, respectively.

Table 2.5 The reaction system of PCR amplification for TR5 fragment.

1.25 µL	Template [(pEX-A128-Mucin5 (20 ng/µl)]
5.00 µL	10× AccuPrime PCR Buffer
1.00 µL	Primer Fwd (10 µM)
1.00 µL	Primer Rev (10 µM)
0.20 µL	AccuPrime *Taq* DNA polymerase
41.55 µL	H_2O
50.00 µL	Total volume

Table 2.6 The procedures of PCR amplification for TR5 fragment.

Initial denaturation	94℃	2 min	
Denaturation	94℃	15 s	
Annealing	52℃	15 s	30 cycles
Extension	68℃	19 s	
Final extension	68℃	10 min	

Table 2.7 The reaction system of PCR amplification for TR10 fragment.

1.25 µL	Template [19ADR7TC_Mucin_07_2019_pMA_RQ (25 ng/µl)]
5.00 µL	10× AccuPrime PCR Buffer
1.00 µL	Primer Fwd (10 µM)
1.00 µL	Primer Rev (10 µM)
0.20 µL	AccuPrime *Taq* DNA polymerase
41.55 µL	H_2O
50.00 µL	Total volume

Table 2.8 The procedures of PCR amplification for TR10 fragment.

Initial denaturation	94℃	2 min	
Denaturation	94℃	15 s	
Annealing	52℃	15 s	30 cycles
Extension	68℃	37 s	
Final extension	68℃	10 min	

Table 2.9 The reaction system of PCR amplification for TR15 fragment.

1.00 µL	Template [19AAPO2C_Mucin_pMK-RQ (25 ng/µl)]
5.00 µL	10× AccuPrime PCR Buffer
1.00 µL	Primer Fwd (10 µM)
1.00 µL	Primer Rev (10 µM)
0.20 µL	AccuPrime *Taq* DNA polymerase
41.80 µL	H_2O
50.00 µL	Total volume

Table 2.10 The procedures of PCR amplification for TR15 fragment.

Initial denaturation	94℃	2 min	
Denaturation	94℃	15 s	
Annealing	52℃	15 s	30 cycles
Extension	68℃	57 s	
Final extension	68℃	10 min	

2.1.4 DNA agarose gel electrophoresis and DNA gel extraction

After restriction enzyme digestion, PCR reaction, or extraction of plasmids, the produced DNAs mixed with DNA Loading Dye (6×, B7024S, New England BioLabs) were loaded into 1% (w/v) agarose gel in TAE buffer for gel electrophoresis. The electric field applied when running the gel is 5-10 V/cm. Red Safe (20000×, #21141, iNtRON Biotechnology, Seongnam, Korea) was used to visualize nucleic acids in an agarose gel under UV illumination in a gel imaging system (Gel Doc XR+ Imaging System, Bio-Rad Laboratories, USA).

Using a standard DNA ladder (Quick-Load® Purple 1 kb Plus DNA Ladder, N0550S; or Quick-Load® Purple 1 kb DNA Ladder, N0552S, New England BioLabs) for identifying the desired DNA band, which was then excised to extract the corresponding DNA. For this, a gel extraction kit (Monarch DNA Gel Extraction Kit, T1020S, New England BioLabs) was used. The steps were conducted according to the protocol provided. Simply, after the gel slice was diluted completely by the addition of four volumes of gel dissolving buffer, the sample was loaded onto the provided column for centrifugation. After washing the column, the DNA was collected with the provided elution buffer in a new tube. DNA concentration was measured in the microvolume UV-Vis spectrophotometer (NanoDrop 1000, Thermo Fisher Scientific, MA, USA) at 260 nm.

2.1.5 DNA seamless assembly

The method of DNA ligation used in this work was DNA seamless assembly with NEBuilder® HiFi DNA Assembly Master Mix (E2621L, New England BioLabs). Overlapping sequences between adjacent DNA fragments were designed when preparing individual fragments. All DNA fragments to be assembled were added into a tube together with the assembly master mix which contains different enzymes, and incubated at 50°C for 15 min. During the incubation, the exonuclease removes nucleotides from the 5' end, leaving single-stranded 3′ overhangs. Then the adjacent fragments with designed complementary ends were annealed. Finally, the polymerase extends the 3' ends and DNA ligase seals the nicks, producing assembled double-stranded DNA.

For the first type of optogenetic actuator, the linearized TO-ChR2opt-mKATE fragment and targeting fragment AT (see Section 2.1.1) were assembled in the reaction system as shown in **Table 2.11**, generating a new plasmid TO-ChR2opt-mKATE-AT (7028 bp).

Table 2.11 The reaction system for assembling TO-ChR2opt-mKATE-AT.

7. 82 μL	H_2O
1.78 μL	TO-ChR2opt-mKATE (45 ng/μl)
0.40 μL	AT (30 ng/μl)
10.00 μL	NEBuilder HiFi DNA Assembly Master Mix
20.00 μL	Total volume

For the second type of optogenetic actuator, the linearized pcDNA4/TO vector, ChR2XXL-YFP fragment, and targeting fragments of different lengths of mucin tandem repeats (TR5, TR10, and TR15, see Section 2.1.2) were assembled in the reaction systems, as shown in **Tables 2.12**, **2.13** and **2.14** respectively, generating three new plasmids TO-TR5-ChR2XXL-YFP (7080 bp), TO-TR10-ChR2XXL-YFP (7380 bp), and TO-TR15-ChR2XXL-YFP (7680 bp).

Table 2.12 The reaction system for assembling TO-TR5-ChR2XXL-YFP.

7.81 μL	H_2O
0.84 μL	pcDNA4/TO (60 ng/μl)
0.33 μL	TR5 (90 ng/μl)
1.02 μL	ChR2XXL-YFP (50 ng/μl)
10.0 μL	NEBuilder HiFi DNA Assembly Master Mix
20.00 μL	Total volume

Table 2.13 The reaction system for assembling TO-TR10-ChR2XXL-YFP.

7.03 μL	H_2O
1.05 μL	pcDNA4/TO (60 ng/μl)
0.65 μL	TR10 (74 ng/μl)
1.27 μL	ChR2XXL-YFP (50 ng/μl)
10.0 μL	NEBuilder HiFi DNA Assembly Master Mix
20.00 μL	Total volume

Table 2.14 The reaction system for assembling TO-TR15-ChR2XXL-YFP.

5.09 μL	H_2O
1.00 μL	pcDNA4/TO (60 ng/μl)
2.70 μL	TR15 (25 ng/μl)
1.21 μL	ChR2XXL-YFP (50 ng/μl)
10.0 μL	NEBuilder HiFi DNA Assembly Master Mix
20.00 μL	Total volume

Assembled structures were collected after undergoing transformation (Section 2.1.6) and extraction of plasmids (Section 2.1.7). The individual fragments before and after assembly were checked by gel electrophoresis, and the corresponding results are shown in Figure A.1. In

addition, the assembled results were confirmed further by DNA sequencing (not shown) and restriction enzyme digestion which can be seen in Figure A.2.

2.1.6 Transformation

The assembled plasmids encoding new optogenetic actuators were transformed into competent *Escherichia coli* (*E.coli*) using the heat shock method for cloning. For plasmid TO-ChR2opt-mKATE-AT, the *E.coli* strain used was One Shot® Top 10 competent cells (C4040-10, Invitrogen). For plasmids TO-TR5-ChR2XXL-YFP, TO-TR10-ChR2XXL-YFP, and TO-TR15-ChR2XXL-YFP, after testing several strains, NEB Stable Competent *E.coli* (C3040H, New England BioLabs) proved suitable for isolation of this kind of plasmid clones containing repeat elements. Before transformation, the Luria Bertani (LB) agar plate containing antibiotics was made in advance. There were 10 g tryptone, 5 g yeast extract, 10 g NaCl and 15 g agar in every 1 Litter of LB liquid medium. After being autoclaved and added with antibiotic Ampicillin (Amp, 100 μg/mL), LB medium was poured into plates which solidified as it cooled. The agar plates were stored upside down at 4℃. The steps of transformation followed the instruction provided by the companies. Simply, add about 2 ng plasmid DNA into the thawed competent *E.coli* cells on ice, followed by incubating the mixture on ice for 30 min. Then, heat shock at 42℃ for exactly 30 s. Next, add pre-warmed S.O.C. medium (15544034, Invitrogen; or B9035, New England BioLabs) into the mixture and shake the vial at 37℃ for exactly 1 h at 225 rpm in a shaking incubator (New Brunswick™ Innova® 42/42R Shaker, Eppendorf AG, Germany). After spreading 80 μL of the mixture on LB agar selection plate, invert the plate and incubate at 37℃ overnight. During the transformation process, sterile techniques should be practiced to avoid contamination. Selections of the colonies and analyses followed.

2.1.7 Extraction of plasmids

After transformation, a single colony was picked from a freshly streaked LB agar selection plate into a 5 mL selective LB medium (Amp, 50 μg/mL) and cultured at 37℃ for approximately 8 h at 225 rpm in a shaking incubator. In order to extract the assembled plasmid for DNA sequencing, the obtained LB-culture was used directly for extracting plasmids with PureLink™ Quick Plasmid Miniprep Kit (K210010, Thermo Fisher Scientific) according to the protocol provided to isolate the sequencing-grade plasmid DNA. For extraction of verified plasmids in large amounts, the 5 mL starter culture was diluted about 1/1000 with a selective LB medium in a flask with a volume of about five times over the volume of the medium. The bacteria were cultured at 37°C at 225 rpm in a shaking incubator for 12-16 h. In order to obtain the transfection-grade plasmids, EndoFree Plasmid Maxiprep Kit (#12362, QIAGEN, Germany) was used. Specifically, after being harvested by centrifuging at 6000 g for 15 min at 4°C and resuspended in 10 mL Buffer P1, the bacteria were lysed by adding 10 mL Buffer P2, an alkaline solution, then were precipitated by adding 10 mL chilled Buffer P3. Next, the crude lysates were filtered by using QIAfilter Cartridge. The endotoxin was removed by adding 2.5 mL Buffer ER. The filtered lysate was then loaded onto the pre-equilibrated anion-exchange resin in QIAGEM-tip. At this step, the plasmid DNAs were selectively bound to the resin under

low-salt conditions. Impurities were removed by washing with 30 mL medium-salt Buffer QC by gravity flow. The ultrapure plasmid DNAs were eluted with 15 mL Buffer QN containing high-salt. 10.5 mL isopropanol was added to concentrate and desalt the plasmids. Finally, resuspending plasmid DNAs in endotoxin-free buffer TE was performed. The yield of plasmid DNA was determined by the microvolume UV-Vis spectrophotometer at 260 nm and quantitative analysis on an agarose gel.

2.2 Cell culture

Three cell types were used in this work and all cell culture works were performed on a sterile bench.

2.2.1 Neurons

The primary cortical neurons were dissected from embryonic day 18 Wistar rat [186] embryos (Janvier Labs, Germany) and transferred to Hank's balanced salt solution without calcium or magnesium ($HBSS^-$; 0.035% sodium bicarbonate, 1mM pyruvate, 10 mM HEPES, 20 mM glucose, pH 7.4; Sigma-Aldrich). Then cortices were mechanically triturated with fire polished, silanized Pasteur pipettes into homogeneous cell solution. Add 2 volumes of $HBSS^+$ solution with calcium or magnesium (Sigma-Aldrich) into the cell suspension. Alternatively, the cell suspension could be prepared by digesting the cortices with 0.05% Trypsin EDTA (Life Technologies) for about 10 min at 37°C followed by mechanical trituration, then cultured as described by Brewer et al. [187]. Incubate at room temperature (RT) for 3 min to let clumps and glia cells settle down. Transfer the supernatant to a new tube. Determine cell density with Trypan blue (Sigma-Aldrich; Trypan blue: NB medium (see below): cell suspension = 1:2:1) in a hemacytometer. Collect the desired number of cells after centrifugation at 200 g for 2 min at 25°C. Neurons were electroporated when desired (see Section 2.3.1). Then neurons were plated onto poly-L-lysine (PLL, 10 µg/mL, Sigma-Aldrich) and extracellular matrix (ECM, 100 µg/mL, Sigma-Aldrich)-coated glass coverslips in a density of 250 cells/mm^2. Cell density is a critical factor for neuronal growth *in vitro*. It can not be too low, as neurons depend on paracrine trophic support from the adjacent cells. Cells were maintained in Neurobasal (NB) Medium (Life Technologies) supplemented with 1% (v/v) B-27 (Gibco), 0.5 mM L-glutamine (Gibco) and 50 µg/mL gentamicin antibiotic (Sigma-Aldrich) in a humidified 5% CO_2, 37 °C incubator. Half of the medium was exchanged with fresh NB medium twice per week.

For treatment with mAb TS2/16 (14-02990-82, Invitrogen), the antibody was supplemented into the general culture media at different final concentrations (0.1, 0.5, 1, 2, 5, or 10 µg/mL) after 1-4 h recovery from electroporation. For the jacalin treatment experiment, glass coverslips were coated with fibronectin (FN) or vitronectin (VN) together with PLL and ECM in advance. The concentrations used were as follows: 8 (or 32), 50, and 10 µg/mL for FN, ECM, and PLL, respectively, or 1.5 (or 10), 50, and 10 µg/mL for VN, ECM, and PLL, respectively. Different final concentration (5, 10, 20, or 30 µg/mL) of jacalin was added to the culture media.

Primary cortical neurons used in this work were obtained according to permit number 81-02.04.2018.A190, approved by the Landesumweltamt für Natur, Umwelt und Verbraucherschutz Nordrhein-Westfalen, Recklinghausen, Germany.

2.2.2 HEK293 cells

Human Embryonic Kidney 293 (HEK293) cells were cultured in Dulbecco's modified Eagle's medium (Sigma-Aldrich) supplemented with 10% FBS (Life Technologies) and 100 U/mL penicillin/streptomycin (Gibco) at 37 °C and 5% CO_2. Stock cells were cultured in a T25 flask and routinely passaged three times per week by trypsinization. These cells were chemically transfected with plasmids one or two days after seeding when desired (see Section 2.3.2). HEK293 cells were cultured on tissue culture plastic (TCP) well plates for determining the transfection efficiencies of channelrhodopsins or on PLL-coated glass coverslips for characterizing electrophysiological features of channelrhodopsins in patch clamp experiments.

2.2.3 MDCK cells

Madin-Darby canine kidney (MDCK) type II cells were maintained in Minimum Essential Medium Eagle (M2279, Sigma-Aldrich) supplemented with 5% fetal bovine serum (FBS, Life Technologies) and 2 mM L-Glutamine (Life Technologies) in T25 flasks at 37 °C and 5% CO_2. Stock cultures were maintained between 20% and 90% confluency, splitting roughly every three days. MDCK cells were chemically transfected with plasmids within two days after plating when desired (see Section 2.3.2). In the experiment for evaluating the transfection level of different channelrhodopsins, MDCK cells were grown on TCP well plates. As for cells used for immunofluorescence staining, they were plated at high density (1×10^5 cells/cm^2) on polycarbonate filters (d = 13 mm, pore size 0.4 μm, 7065292, Whatman® Nuclepore™ Track-Etched Membranes) to grow for about 5 days to allow the development of a tight monolayer.

2.3 Gene delivery

2.3.1 Nucleofection

Nucleofection, a transfection method based on electroporation, enables the transfer of nucleic acids into the nucleus by applying a specific voltage pulse. In this work, primary cortical neurons were nucleofected with Rat Nucleofector™ Kit (VPG-1003, Lonza Cologne GmbH, Germany). First, RPMI (Roswell Park Memorial Institute) base media (Gibco, Grand Island, NY, USA) was supplemented with 1% FBS (Gibco, Grand Island, NY, USA) and 0.5 mM L-glutamine (Gibco, Paisley, UK). The desired number of wells were filled with supplemented RPMI media and preincubated in a 37°C, 5% CO_2 humidified incubator for about 1 h to equilibrate the pH to 7.4. After collection of the appropriate number of primary cortical neurons ($0.2\text{-}6\times10^6$ cells per cuvette) (see Section 2.2.1), the cell pellet was resuspended in 100 μL prewarmed nucleofector solution added with the supplement. Cells should not stay in the nucleofection mixture solution for more than 15 min, since this can decrease cell viability and

transfection efficiency. After the addition of 3 μg plasmid DNA, the tube was gently flicked to mix for about 20 s. The plasmid DNA should be in high quality (A_{260}/A_{280} ratio = 1.7~1.9) without bacterial endotoxin since neurons are quite susceptible cells. The mixture was transferred into a nucleofection cuvette, avoiding generating air bubbles (they reduce transfection efficiency). Then it was placed in the cuvette holder of the nucleofector device (AAD-1001S, Lonza, Germany) and the nucleofection was started with an appropriate program (number G-013, "Neurons, Chicken DRG"). Then 900 μL prewarmed RPMI recovery media was added to the cuvette. The number of live cells was counted using Trypan blue exclusion in a hemacytometer (see Section 2.2.1). The provided plastic pipette was used to gently transfer the required numbers of cells into equilibrated media avoiding shearing forces, followed by plating them onto coated glass coverslips in a well plate at a desired density. After 2-4 h, the recovery media was replaced with fresh NB medium. Half of the medium was exchanged with fresh NB medium every 3-4 days.

2.3.2 Transfection

HEK293 and MDCK cells were chemically transfected with FuGENE® HD Transfection Reagent (E2311, Promega). Cells were plated onto substrates one day before transfection. The transfection media without serum or antibiotics was prewarmed to RT. An appropriate amount of plasmid DNA was added (typically 1 μg per well of a 24-well plate) into the media, and mixed by pipetting completely. The prewarmed FuGENE® HD Regent was added to the middle of the mixture solution directly avoiding contacting the wall of the tube. Here the ratio of transfection reagent and DNA used was 1.5:1. The transfection conditions for other plasmids or cell types may require optimization. After tapping the tube a few times, it was incubated at RT for 10-15 min. 25 μL FuGENE® HD Regent/DNA mixture was added per well to 24-well plates containing 500 μL of seeded cells in culture media. For different well plates, volumes must be scaled accordingly. Plates were mixed by gently shaking, then returned to the standard incubator.

2.4 Immunofluorescence staining and image analysis

Immunostaining is a biological technique based on the specific binding of antigens and antibodies to detect specific target molecules in a biosample. The primary antibody was used to specifically bind to a target molecule, and the fluorophore-conjugated secondary antibody was applied to visualize the primary antibody-target complex and amplify the signal since multiple secondary antibodies can bind to each primary antibody. For sample preparation, cells were fixed with pre-warmed 4% (w/v) paraformaldehyde (Sigma-Aldrich) in phosphate buffered saline (PBS; 137 mM NaCl, 2.7 mM KCl, 8.1 mM Na_2HPO_4, and 1.5 mM KH_2PO_4) for 10 min at RT. Then the fixed cells were permeabilized with 0.3% TritonX-100 (Sigma-Aldrich) in blocking buffer (BB; 1% (w/v) bovine serum albumin and 2% (v/v) heat-inactivated goat serum (Sigma-Aldrich) in PBS) for 10 min at RT. Cells were treated with BB at 4°C in the

dark overnight to block unspecific binding sites. Then the primary and secondary antibodies were applied.

For neurons, the following primary antibodies were used: rabbit anti-MAP2 (Microtubule Associated Protein 2, a dendritic marker; AB5622, Sigma-Aldrich) and mouse anti-Tau1 (an axonal marker; MAB3420, Sigma-Aldrich). The secondary antibodies used in neurons expressing ChR2opt-mKATE and ChR2opt-mKATE-AT were goat anti-rabbit Alexa Fluor 488 (A11034, Life Technologies) and goat anti-mouse Alexa Fluor 350 (A21049, Life Technologies). The secondary antibodies used in neurons expressing ChR2XXL-YFP, TR5-ChR2XXL-YFP, TR10-ChR2XXL-YFP, and TR15-ChR2XXL-YFP were goat anti-rabbit Alexa Fluor 633 (A21071, Life Technologies) and goat anti-mouse Alexa Fluor 350 (A21049, Life Technologies).

As for MDCK cells grown on polycarbonate filters, the primary antibody was mouse anti-Podocalyxin/podxl (an apical protein, 3F2/D8). The Hybridoma developed by SUNY Brooklyn was obtained from the Developmental Studies Hybridoma Bank, created by the NICHD of the NIH and maintained at The University of Iowa, Department of Biology, Iowa City, IA 52242. The secondary antibody used in cells expressing ChR2opt-mKATE and ChR2opt-mKATE-AT was goat anti-mouse Alexa Fluor 488 (A11001, Life Technologies). The secondary antibody used in cells expressing ChR2XXL-YFP, TR5-ChR2XXL-YFP, TR10-ChR2XXL-YFP, and TR15-ChR2XXL-YFP was goat anti-mouse Alexa Fluor 633 (A21052, Life Technologies). Nuclei were stained with 4’,6-diamidino-2-phenylindole (DAPI, Sigma-Aldrich).

Samples were mounted to glass microscope slides in Dako Fluorescence Mounting Medium (S3023, Agilent Technologies) and photographed by using an Axio Imager Z1 equipped with a digital CCD camera AxioCam MR R3 and various objectives. The UV light source illuminator was HXP120 (Osram) and the PC imaging light source was HAL100 Halogen. The slides of immunostained neurons were imaged with a 20× air objective (EC Plan-Neofluar). ApoTome (Carl Zeiss Microscopy GmbH) was an additional slider module, which was used for producing high-resolution digital fluorescent images for thick specimens or constructing the stacked images of samples in z-direction via integrated software function to mimic three-dimensional (3D) structure. Therefore, it was suitable to image the monolayer of MDCK cells seeded on the membrane filter. The immunostained MDCK cells were imaged with 40× oil objective (EC Plan-Neofluar) by using ApoTome. For each sample, xy-stage was fixed, and images were captured every 1 µm in z-stage for 20 µm in total height. The filter set Zeiss 43 HE, excitation 550/25, beam splitter FT 570, and emission BP 605/70 were used for capturing the red fluorescence of mKATE and Alexa Fluor 633. The filter set Zeiss 38 HE, excitation 470/40, beam splitter FT 495, and emission BP 525/50 were used for capturing the yellow fluorescence of YFP and the green fluorescence of Alexa Fluor 488. The filter set Zeiss 49, excitation G365, beam splitter FT 395, and emission BP 445/50 were used for capturing the blue fluorescence of DAPI. The images were processed with ZEN 2012 blue edition.

For quantitative analysis of the immunostaining images, two forms of axon-to-dendrite expression ratio, normalized (ADR) and unnormalized (uADR), were evaluated using Fiji software. The mean amount of fluorescence per pixel (F) was achieved after subtracting the background. The ratio of F in the axon and dendrite of the individual actuator was calculated as the uADR. The normalized ADR was individual uADR divided by the uADR value of nonspecifically localized ChR2opt-mKATE or ChR2XXL-YFP. It is straightforward to evaluate the distribution of protein based on the ADR value. If ADR = 1, the protein is nonspecifically localized; if ADR < 1, the protein is localized to dendrites; and if ADR > 1, the protein is localized to the axon.

2.5 Patch clamp

Electrophysiology was investigated by using the whole cell patch clamp technique. In this work a typical patch clamp setup was used, which mainly consisted of a grounded Faraday cage, a microscope, an amplifier, micromanipulators, pipette-holders, and a computer for controlling stimulation and data acquisition. The patch clamp microscope was placed on a vibration isolation table because the seal between the pipette and cell membrane is easily influenced by vibration. The amplifier used was EPC9 (HEKA Elektronik Dr. Schulze GmbH, Germany), which was controlled by TIDA 5.240 software (HEKA Elektronik Dr. Schulze GmbH). The electrophysiological experiments were performed at room temperature either in neurons between DIV7 (7 days *in vitro*) and DIV20 or HEK293 cells between DPT2 (2 days post transfection) and DPT5. Both of the cells were transfected with corresponding optogenetic actuators as described in Section 2.3. The Ag/AgCl electrode was used owing to its biocompatibility under measurement conditions. One was used as a recording electrode mounted inside the pipette holder, and the other one served as a reference electrode placed in the extracellular patch solution. The components of the extracellular patch solution were 120 mM NaCl, 3 mM KCl, 1 mM $MgCl_2$, 10 mM HEPES, 2 mM $CaCl_2$ (pH 7.3, 248 mosm/kg) for neurons and 140 mM NaCl, 5 mM KCl, 5 mM $MgCl_2$, 10 mM HEPES, 1 mM $CaCl_2$ (pH 7.3, 248 mosm/kg) for HEK293 cells. Lidocaine (100 µM) was added into the extracellular patch solution to inactivate voltage-gated sodium channels when comparing the electrophysiological characteristics of ChR2opt-mKATE-AT and ChR2opt-mKATE in neurons. The components of the intracellular patch solution were 2 mM NaCl, 120 mM KCl, 4 mM $MgCl_2$, 5 mM HEPES, 0.2 mM EGTA, 0.2 mM Mg-ATP (pH 7.3, 255 mosm/kg) for both neurons and HEK293 cells. The intracellular patch solution was filtered with a 0.2 µm pore filter to remove dirt. The glass patch pipettes with a 1-3 µm tip diameter were pulled from fire polished borosilicate glass capillaries (O.D. = 1.5 mm, I.D. = 0.86 mm; Sutter Instrument, USA) in a micropipette puller (P-2000, Sutter Instrument) shortly before starting the patching experiments to avoid blocking the pipette tips by dust in the air. A glass micropipette filled with intracellular patch solution was inserted into a pipette holder. Positive pressure was applied to the pipette via tubing connected to the pipette holder to clear away extracellular debris around the pipette tip. The

pipette was lowered into the extracellular patch solution and moved to the center of the field of view. A test pulse (10 mV, 10 ms) was applied to monitor the resistance of the pipette tip. The resistance should be 3-6 Ω, which meant a proper size of the pipette tip. The size of the pipette tip is critical since if it is too small, it is hard to break into the cell and will lead to a high access resistance, and if it is too big, it is hard to form a good seal. The offset potentials caused by polarization at the electrode or junction potentials between the intracellular patch solution inside the pipette and the extracellular patch solution were compensated. The pipette was maneuvered close to the cell surface membrane until the resistance of the membrane rose about 1 MΩ, which meant good contact between the pipette tip and membrane was formed. The positive pressure was immediately released and a light negative pressure was applied if needed, to form a gigaohm seal (> 1 GΩ). A holding potential to approximately the cell's resting membrane potential was applied. Fast capacitive currents caused by charging the pipette and the sealed membrane were compensated. Suction was applied to rupture the membrane. Slow capacitive currents caused by charging the whole cell membrane and also the series resistance of the cell were compensated along with the leak currents. Experiments were conducted in either voltage clamp mode or current clamp mode with a holding current or a holding potential as indicated in the caption.

2.6 Optogenetic manipulation

The laser source for photostimulation was a 473 nm diode laser (Rapp OptoElectronic GmbH, Germany), which was controlled by UGA40 (Rapp OptoElectronic GmbH). The combination of UGA40 and laser was calibrated each time when started. Laser flashes were triggered electronically by a UGA targeting software with specific pulse time and delay time (as indicated in the individual result part) to achieve precise control of the laser spot position and duration of illumination. An external TTL trigger pulse was applied from the laser input to start data acquisition by HEKA EPC9, which made it possible to achieve signal synchronization for the patch clamp. The light path of the blue laser was guided into a Zeiss Axio Scope upright microscope equipped with an Olympus objective (20×W). An HXP light source (Carl Zeiss AG) with filter set excitation 472/35, Beam splitter 497-505, emission 534/30 was used to identify ChR2XXL-YFP- or TR-ChR2XXL-YFP-positive cells, and filter set Beam splitter FT 580, emission LP 590 was used to identify ChR2opt-mKATE- or ChR2opt-mKATE-AT-positive cells. The excitation filter of red fluorescence was coupled to the light path behind the HXP light source and before the laser source so that the red fluorescence can be effectively used in combination with the blue laser. The AxioCam MRm (Carl Zeiss AG) was attached to the microscope for image acquisition. In the optogenetic manipulation of neurons, if there is no explicit statement, all the blue light stimulation positions and the recording positions were at soma.

The produced photocurrent is related to the number of open channels in the illuminated area. An ideal illumination area, namely the laser spot size, should be small while maintaining

sufficient currents so that the light can be applied much more precisely. The laser spot size was controlled by wheels on the back side of the setup where lasers were attached to the light path. During the pre-experiment, the laser spot size was adjusted by carefully turning the wheel to find the position where the best optogenetic signal could be achieved. Then an image of the best laser spot at minimum laser output power was taken by virtue of a mirror slide on the sample holder. The laser spot size was determined by measuring the diameter of the spot in the image. Here, the definition of laser diameter used is the full width at half-maximum (FWHM). A laser spot size of 12 µm in diameter, that is, a 113 μm^2 illuminated area was proven suitable. Besides, the light output power involved in this work is ranging from 0.015 mW to 3 mW. The light power stated in the present work is the power of the laser beam, which has a Gaussian paraboloid distribution within the spot.

2.7 Live-cell imaging

In order to investigate the underlying mechanism of subcellular localization of protein ChR2opt-mKATE-AT in neurons, the protein trafficking was observed in real-time by performing live-cell imaging. The live-cell imaging setup mainly consisted of an inverted microscope equipped with an incubation chamber, external control panels, a fluorescence unit, and a computer to control the setup. The inverted microscope (Axio Observer.Z1, Zeiss) was equipped with a PCO.edge 5.5 scientific complementary metal-oxide-semiconductor (sCMOS) camera and with various objectives. The incubation chamber (PeCon) could provide cells with a proper *in vitro* culture condition for a long time owing to the equipped temperature, CO_2, and humidity control. It was convenient to use external control panels to, for example, move precisely the xy-stage of the microscope (Merzhäuser). The Colibri fluorescence unit (Zeiss) along with a series of filter sets provided optical devices for taking fluorescent images. The microscope can be controlled with the Zeiss software ZEN 2012 blue edition. Primary neurons were transfected with plasmid encoding protein ChR2opt-mKATE or ChR2opt-mKATE-AT before plating, as described in Section 2.3.1. Neurons on DIV7 were imaged on the microscope with a 40× air objective (LD Plan-Neofluar, 0.6 NA, Ph2, Zeiss). The filter set Zeiss 43 HE DsRed, excitation 538-562, beam splitter 570, and emission 570-640 was used to capture the red fluorescence of mKATE. Images were acquired at 37°C, 5% CO_2, and 100% humidity every 1 min for about 2.5 h. The images were processed with the software ZEN2012 and ImageJ.

For evaluation of the transfection efficiencies of ChR2XXL-YFP and TR-ChR2XXL-YFP in different cell types, HEK293 cells on DPT2, MDCK cells on DPT5, and neurons on DIV4-14 were imaged by using the live-cell imaging setup as well. The phase contrast images and fluorescent images were obtained. The filter set Zeiss 38 HE, excitation 470/40, beam splitter FT 495, and emission BP 525/50 were used to capture the yellow fluorescence of YFP. The images were processed with the software ZEN2012 and ImageJ as well.

2.8 Statistical analyses

Data were processed and analyzed using Excel, Origin, TIDA 5.240, Python, or Matlab software. Data were given as mean ± Standard Error of Mean (mean ± SEM) or mean ± Standard Deviation (mean ± SD) as indicated in the corresponding text and caption. All statistical significance analyses were performed using SPSS software. Shapiro-Wilk test was used to check the normality of samples, and Levene's test was used to check the homogeneity of variance. If these preconditions were met, a One-Way ANOVA or Two-Way repeated ANOVA test was performed for comparison between groups. Otherwise, the Mann-Whitney test was applied for comparison between two groups and the Kruskal-Wallis One-Way ANOVA test was conducted for comparison between multiple groups. The significance level was denoted as $^{*}(p \leq 0.05)$, $^{**}(p \leq 0.01)$ and $^{***}(p \leq 0.001)$.

3 Optogenetic actuator I

This chapter focuses on the first constructed actuator based on a classic channelrhodopsin variant ChR2(H134R) (see Section 1.3.2.1) that was optimized and named ChR2opt. The original protein ChR2opt tagged with a red fluorescence was encoded by plasmid TO-ChR2opt-mKATE, and it has a moderate photocurrent, relatively fast kinetics, and good viability in multiple cell lines [188], so it was chosen as the basic construct to be modified. First, the detailed strategy for constructing ChR2opt-mKATE-AT was described (**Section 3.1**), followed by the investigation of its subcellular localization in polarized cells by using fluorescent immunostaining (**Section 3.2**). Then, the intrinsic electrophysiological properties of actuator-expressing neurons were evaluated in the dark by using the whole patch clamp technique (**Section 3.3**). Next, the electrophysiological characteristics of ChR2opt-mKATE-AT were investigated under different light stimulation conditions (**Section 3.4**) and were also compared with that of ChR2opt-mKATE in different cell types (**Section 3.5**). Besides, the spatial specificity of optogenetic control by using ChR2opt-mKATE-AT was estimated (**Section 3.6**). Finally, the underlying mechanism of subcellular localization was explored by observing the protein trafficking in real time (**Section 3.7**). Portions of this chapter are in preparation for publication.

3.1 Construct generation

As the initial material, I used the leading 315 amino acids sequence of ChR2 with H134R mutation, optimized for the expression in rodent cells named ChR2opt [188]. In order to analyze intracellular localization and expression level as well as minimize the spectral overlap with ChR2 absorption, a red fluorescent protein, mutated Katushka (mKATE) [189], was tagged to the C-terminus of channelrhodopsin. A linker TAVATI was inserted between the channel ChR2opt and mKATE as a spacer to avoid interfering with each other. In order to avoid protein aggregations in the endoplasmatic reticulum (ER), an ER export sequence (FCYENEV) from mammalian inward rectifying potassium channel 2.1 was added to the end [190]. The whole protein construct was named ChR2opt-mKATE, which was inserted into the pcDNA™4/TO mammalian expression vector. A cytomegalovirus (CMV) promoter that can drive the constitutive expression of a gene in mammalian cells was used. A targeting motif, the cytoplasmic tail of human rhodopsin, was then added to these fragments. As mentioned in Section 1.4.2, the short sequence of the last 32 amino acids is an apical sorting signal in polarized epithelial cells. In order to increase the possibility of subcellular targeting, two fragments of this targeting motif in succession were used, and the whole sequence was named AT (Apical Targeting). Detailed protocols are seen in Section 2.1.1. To add the targeting motif AT to the C-terminal domain of ChR2opt-mKATE, DNA seamless assembly was used as described in Section 2.1.5. The produced optogenetic actuator was named ChR2opt-mKATE-

AT. The results were confirmed by DNA sequencing and restriction enzyme digestion (see Figure A.2 A). The schematics of ChR2opt-mKATE and ChR2opt-mKATE-AT are shown in **Figure 3.1**.

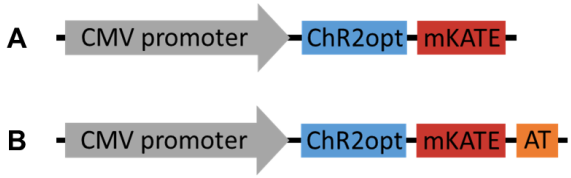

Figure 3.1 The schematics of ChR2opt-mKATE (**A**) and ChR2opt-mKATE-AT (**B**). ChR2opt-mKATE-AT was generated by fusing ChR2opt-mKATE with AT sequence from human rhodopsin at its C-terminus. Cytomegalovirus (CMV) promoter, a strong promoter, drives constitutive expression of genes under its control in mammalian cells; ChR2opt, an optimized ChR2 with H134R mutation; mKATE, a red fluorescent protein; AT, a targeting motif. In order to avoid interference from adjacent constructs, six amino acids (TAVATI) were inserted as a linker between ChR2opt and mKATE, and thirty-one amino acids were left between mKATE and AT.

3.2 Subcellular localization in polarized cells

3.2.1 Subcellular localization in MDCK cells

MDCK cells, another typical polarized cell type, are widely used as models for studying epithelial polarity, trafficking, and tight junctions. Their advantages include the rapid growth rate, clear cell polarity and suitability for use in advanced microscopic techniques [191, 192]. To investigate the subcellular localization of these actuators, MDCK cells were cultured on permeable membrane filters. In this case, MDCK cells can absorb nutrients from the basolateral surface through the membrane pores resulting in much better differentiated and polarized monolayers (10-15 μm tall) than those grown on solid plastic or glass substrates (3-5 μm tall) [193]. MDCK cells were chemically transfected within two days after being plated at high density (1×10^5 cells/cm^2) on the membrane and grew for about 5 days to form a tight monolayer. The cells were subsequently immunostained with a primary antibody against podxl (podocalyxin-like protein 1), also known as gp135, which is a typical apical membrane protein in epithelial cells [194, 195]. The secondary antibody Alexa Fluor 488 was used to visualize protein podxl in the apical membrane surface of MDCK cells. Meanwhile, 4',6-diamidino-2-phenylindole (DAPI) was used to identify nuclei, facilitating the distinction of the individual plasma membrane regions enclosing cells. The images were captured by using fluorescent microscopy equipped with an ApoTome slider module so that the stacked structure of MDCK cells in the z-direction can ultimately be constructed via an integrated software function.

The top view and reconstructed orthogonal slices show the proteins' localization relative to the apical membrane as displayed in **Figure 3.2**. In each image, the top view of MDCK cells is shown in the main window (XY plane). The focus level of the top view is indicated in the

orthogonal view by a blue line. Vertical views of MDCK cells cut at green and red dashed lines are presented in the small green (XZ plane) and red windows (YZ plane), respectively. The orientations of image layers in z-stack were all the same, and the top and bottom layers are marked as T and B respectively in the first image of **Figure 3.2A**. It was found that the red fluorescence was distributed throughout the whole plasma membrane, both the apical side and basolateral side, in **Figure 3.2A**, while it was only located on the apical side in **Figure 3.2B**. The results indicated that ChR2opt-mKATE localized to both the apical and basolateral sides of MDCK cells, while ChR2opt-mKATE-AT primarily targeted to the apical membranes.

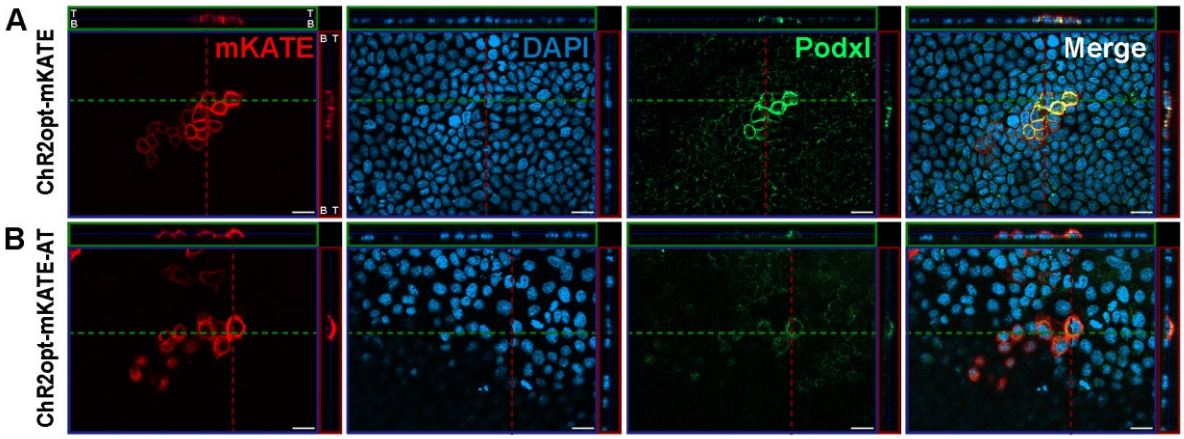

Figure 3.2 The subcellular localization of ChR2opt-mKATE (**A**) and ChR2opt-mKATE-AT (**B**) when expressed in MDCK monolayers. Expressed channelrhodopsins were visualized by mKATE (red). Cell nuclei were identified by DAPI staining (blue). The apical surface of MDCK cells was identified by antibody 3F2/D8 against Podxl (green). Merged images are shown in the last column. In each image, the top view of MDCK cells (at the focus level indicated by the blue line in small windows) is shown in the main window (XY plane), and vertical views of MDCK cells cut at green and red dashed lines are presented in the small green (XZ plane) and red windows (YZ plane), respectively. T, top layer; B, bottom layer. Scale bar, 20 µm.

3.2.2 Subcellular localization in neurons

The neuron is a polarized cell with clear subcellular compartmentalization, typically the somatodendritic and axonal regions. To determine if the newly constructed ChR2opt-mKATE-AT could be applied for subcellular optogenetic investigation, its subcellular localization in primary neurons was first evaluated. Dissociated cortical neurons were taken from embryonic day 18 rat embryos and were cultured on glass coverslips coated with PLL and ECM *in vitro*. Before plating, nucleofection was conducted to deliver the gene encoding ChR2opt-mKATE or ChR2opt-mKATE-AT into the primary neurons. Neurons grew *in vitro* for 5-7 days, then immunostaining was performed. In order to visualize dendrites and axons, antibodies against MAP2, a typical dendritic protein, and Tau1, a typical axonal protein, were used. Then images were captured by using fluorescent microscopy with an appropriate filter set, as shown in **Figure 3.3A**. It could be seen that ChR2opt-mKATE localized to both the somatodendritic region (open arrowheads) and axonal region (filled arrowheads), while ChR2opt-mKATE-AT mainly localized to the somatodendritic region.

Quantitative analysis was conducted as well to figure out to what extent the polarized distribution of ChR2opt-mKATE-AT in primary neurons can be achieved. Two forms of axon-to-dendrite expression ratio, normalized (ADR) and unnormalized (uADR), were calculated (see Section 2.4). The value of uADR for ChR2opt-mKATE (0.60 ± 0.05, mean ± SEM) was approximately two times larger than that of ChR2opt-mKATE-AT (0.36 ± 0.03) (**Figure 3.3B**(a)). The uADR of ChR2opt-mKATE-AT was significantly different from that of ChR2opt-mKATE. It is advantageous to evaluate the localization of a protein according to the ADR value, as ADR = 1 means the protein is nonspecifically localized, ADR < 1 means the protein is localized to dendrites, and ADR > 1 means the protein is localized to the axon. The ADR of ChR2opt-mKATE-AT was 0.69 ± 0.07, indicating this protein was localized to dendrites but not the axon in primary neurons (**Figure 3.3B**(b)). For a further discussion on the subcellular localization of ChR2opt-mKATE-AT in polarized cells, see Section 5.1.1.

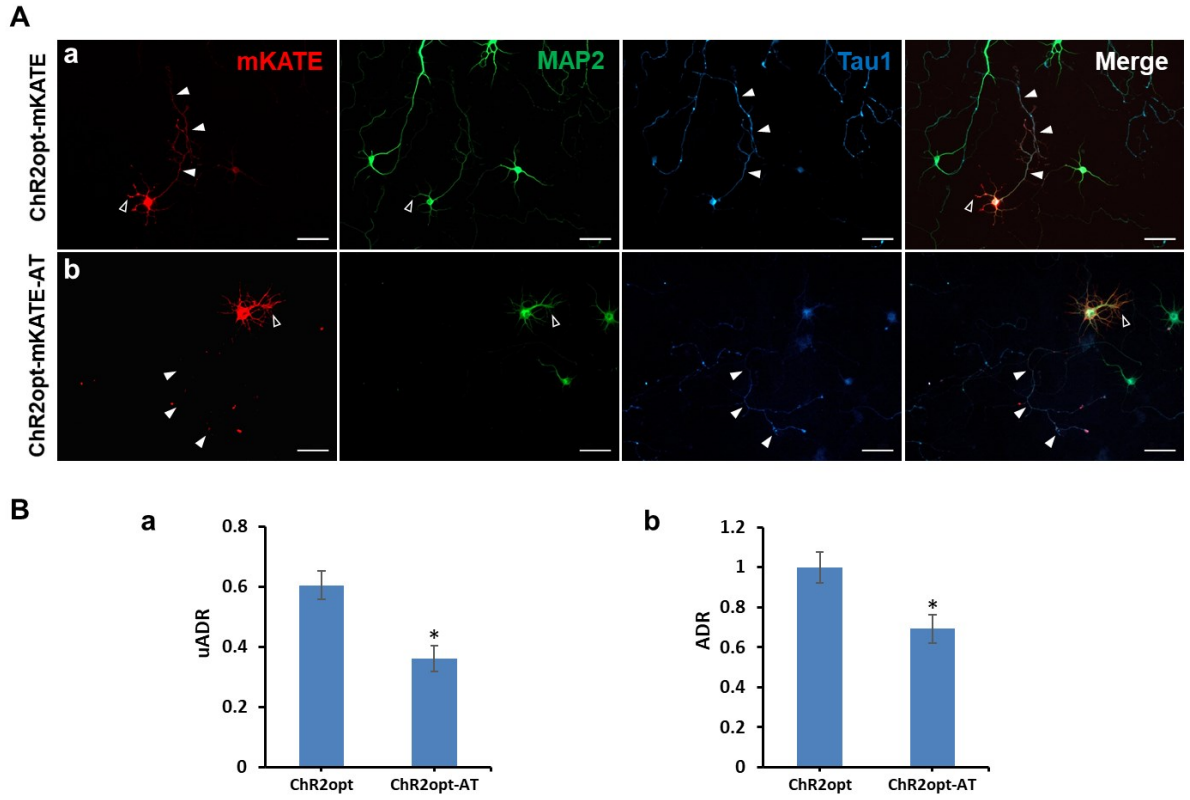

Figure 3.3 The subcellular localization of ChR2opt-mKATE and ChR2opt-mKATE-AT when expressed in neurons.

(**A**) Immunostaining of cortical neurons transfected with ChR2opt-mKATE (a) and ChR2opt-mKATE-AT (b) on 5 days *in vitro* (DIV5). Dendrites were labeled with anti-MAP2 (green) and axons with anti-Tau1 (blue). Filled arrowheads point to the axon; open arrowheads point to the dendrite. Scale bar, 50 µm.

(**B**) The unnormalized and normalized axon-to-dendrite expression ratio (uADR and ADR). Data are presented as mean ± SEM. n = 5 for each group. One-Way ANOVA test, $^{*}p < 0.05$.

3.3 Intrinsic electrophysiological properties of neurons

The introduction and expression of exogenetic channelrhodopsins may result in unexpected problems such as increased energy consumption, protein accumulation or improper protein folding, thereby producing negative effects on membrane properties and cell morphology [196, 197]. Also in neurons the intrinsic electrical properties of the plasma membrane have a strong influence on the level of membrane depolarization and the rate of repolarization. Thus, careful monitoring of these properties is necessary especially when the introduced proteins are driven by a strong promoter like CMV. In order to determine if the properties of neuronal membranes were influenced by the expression of ChR2opt-mKATE-AT, commonly used electrophysiological parameters including resting membrane potential, input resistance, and membrane capacitance [162, 198] were investigated in dark here. Resting membrane potential means the membrane potential of a neuron at a resting state without signaling. The resting potential was recorded without current injection in a current clamp mode immediately after forming the whole cell configuration. As seen in **Figure 3.4A**, the resting potentials of neurons expressing ChR2opt-mKATE and ChR2opt-mKATE-AT were -70.86 ± 1.35 mV and -70.96 ± 0.91 mV (mean ± SEM), respectively, both similar to the nontransfected control group (-67.85 ± 1.73 mV). There was no significant difference in the resting potential of these three groups.

Input resistance, which refers to the resistance of the membrane in response to current injection, can reflect the extent that membrane channels are open at a steady state. Higher resistance means there are fewer open channels, while lower resistance means there are more open channels. The input resistance can be evaluated by the voltage change of a cell divided by the amount of current injected that elicited the voltage change. The values of the input resistance of ChR2opt-mKATE-positive, ChR2opt-mKATE-AT-positive, and wild neurons were 199.38 ± 16.63 MΩ, 182.96 ± 7.67 MΩ, and 184.58 ± 12.51 MΩ (mean ± SEM), respectively (**Figure 3.4B**). No significant difference was observed between these three groups.

Cell membrane capacitance can reflect the ability of a cell membrane to store electric charges. As one of the critical factors, it determines how fast the membrane voltage responds to a changing current. The membrane capacitance is equal to changed charges divided by the amount of a voltage step. The changed charges can be evaluated by integrating the transient current in response to the voltage step. The estimated capacitances for the ChR2opt-mKATE group, ChR2opt-mKATE-AT group, and control group were 56.31 ± 9.29 pF, 52.99 ± 7.74 pF, and 55.58 ± 9.01 pF (mean ± SEM), respectively, and there was no significant difference between these three groups (**Figure 3.4C**).

The excitability of neurons was also investigated, which was reflected by the number of spikes evoked by a series of current injections in the dark. The value of injected currents was from 0 pA to 300 pA at 50 pA intervals. In response to a larger injected current, the number of elicited spikes became more. When injected with a 300 pA current, the numbers of spikes in all three groups were the most. Generally, the spikes evoked in the ChR2opt-mKATE-AT group were

slightly fewer than in the other two groups, but there was no significant difference between these groups (**Figure 3.4D**).

All these results indicated that the intrinsic membrane properties of neurons expressing ChR2opt-mKATE-AT were similar to that of ChR2opt-mKATE-expressing neurons and also the nontransfected control neurons. Overall, the expression of ChR2opt-mKATE-AT did not alter membrane integrity and the cells were as healthy as wild type neurons. For a further discussion, see Section 5.1.2.

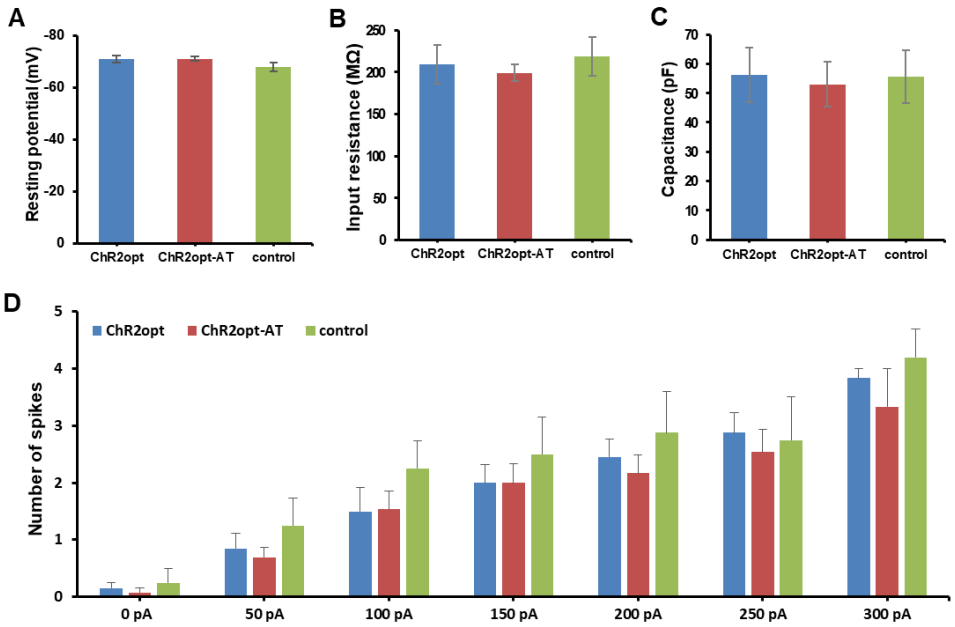

Figure 3.4 The intrinsic electrophysiological properties of neurons expressing ChR2opt-mKATE, ChR2opt-mKATE-AT, and nontransfected control neurons.

(**A-C**) Membrane resting potential (A), input resistance (B), and capacitance (C) of neurons expressing ChR2opt-mKATE, ChR2opt-mKATE-AT, and nontransfected control neurons. Data are presented as mean ± SEM. A, n = 10, 10, and 6; B, n = 13, 16, and 11; C, n = 9, 15, and 6. Kruskal-Wallis One-Way ANOVA test, $p > 0.05$.

(**D**) The number of spikes evoked by a series of current injections ranging from 0 pA to 300 pA at 50 pA intervals lasting 100 ms. Data are presented as mean ± SEM. n = 3-13. Two-Way repeated ANOVA test, $p > 0.05$. In certain figures, ChR2opt-mKATE and ChR2opt-mKATE-AT are shortened as ChR2opt and ChR2opt-AT, respectively, which applies to all figures in this thesis.

3.4 Electrophysiological characterization of ChR2opt-mKATE-AT when expressed in primary neurons

This section focuses on investigating the electrophysiological characteristics of ChR2opt-mKATE-AT when expressed in primary neurons, mainly for two considerations. One is to determine whether the new optogenetic actuator functions well in primary neurons so as to figure out if the electrophysiological properties of channelrhodopsin are affected by the

targeting motif AT. The other one is to find the best illumination conditions that could be used for later optogenetic manipulations. Optimized optogenetic manipulation relies on fine regulation of experimental parameters such as light pulse time, light power intensity, and stimulus frequency.

3.4.1 Pulse time

The first investigated factor that influences the channel's performance was pulse time, which can not be either too short or too long. With an extremely short pulse time there are not enough photons hit on the retinal, so the elicited photocurrent may not be sufficient to depolarize the membrane. With a prolonged pulse time, continuous photocurrents may alter intracellular concentrations of ions such as H^+ and Ca^{2+} that play essential roles in cellular function, thereby resulting in unintended side effects. Here, different pulses (thirteen in total) of blue light ranging from 50 ms to 0.01 ms at 1000 ms interpulse intervals were applied to stimulate neurons expressing ChR2opt-mKATE-AT ten times. The typical six voltage traces recorded by patch clamp in current clamp mode are shown in **Figure 3.5A**. For each pulse time, the first spike is shown in black, and the other nine traces are shown in blue. The results showed that for pulse time longer than 0.01 ms, they all triggered action potentials with high fidelity in ten stimulations and all traces behaved similarly, among which the first one responded fastest. In certain cases of stimulation with a 50 ms pulse time, it even can elicit a second AP. For 0.01 ms pulse time, only two action potentials were triggered in ten stimulations, and their amplitudes were much smaller and the responses were much slower compared with other groups. For the other eight stimulations with the 0.01 ms pulse time, the cell also made responses, but the induced voltage change did not reach the threshold level of the action potential. This was because in such a short time, there were not sufficient ions fluxing through the channels, thereby leading to insufficient depolarization.

Then the slope of depolarization of triggered traces at the beginning of light-on was evaluated. Since in some cases action potentials were triggered when the blue light stimulation lasted more than 3 ms, the voltage traces within the first 3 ms were extracted to analyze the speed of depolarization, which was determined by linearly fitting the voltage trace. Considering that for each pulse time the first spike depolarized much faster than the other nine spikes, the slope of the first depolarization is displayed separately (black bar), and the depolarization values of the other nine spikes were averaged (blue bar), as shown partially in **Figure 3.5B**. When the pulse time was more than 0.5 ms, the rate of depolarization was comparable, roughly staying at 6 mV/ms for the first spike (except that the first one at the very beginning was about 9 mV/ms) and 4.5 mV/ms for the other spikes. When the pulse time was less than 0.5 ms, the speed of depolarization decreased gradually. In the case with 0.01 ms pulse time, the speed was the smallest which was only about 2.5 mV/ms for the first spike and 1.2 mV/ms for the other spikes, which was significantly lower than that with a longer than 1 ms pulse.

Besides, the full width at the half maximum (FWHM) of an induced action potential was compared, which is partially displayed in **Figure 3.5C**. When the pulse time was longer than 1

ms, the FWHM was about 2 ms. With a stimulation shorter than 0.5 ms, the FWHM increased gradually. The FWHMs for stimulation with 0.5 ms, 0.1 ms, and 0.05 ms pulse time were 3.01 ± 0.24 ms, 4.17 ± 0.27 ms, and 5.19 ± 0.32 ms (mean ± SD), respectively, which were significantly different from that with 50 ms pulse time. For 0.01 ms pulse time, the FWHM can be around 9 ms, which is not shown in the histogram. Thus, the pulse time shorter than 0.5 ms widened the full width at the half maximum of evoked action potential compared with using a longer pulse time.

Overall, for neurons expressing ChR2op-mKATE-AT, the pulse time duration needed for inducing APs with high reliability was quite short, and it could be short to 0.1 ms. In some cases, even using a 0.01 ms pulse time of laser could evoke APs although with much smaller amplitudes and much slower kinetics. But for neurons expressing ChR2op-mKATE without AT, it usually needed 5 ms to induce high-fidelity APs in the same condition, and it was also hard to elicit APs when the pulse time was shorter than 1 ms. Thereby, the optogenetic manipulation with ChR2op-mKATE-AT can achieve a higher temporal resolution in neurons (see Section 5.1.2 for discussion).

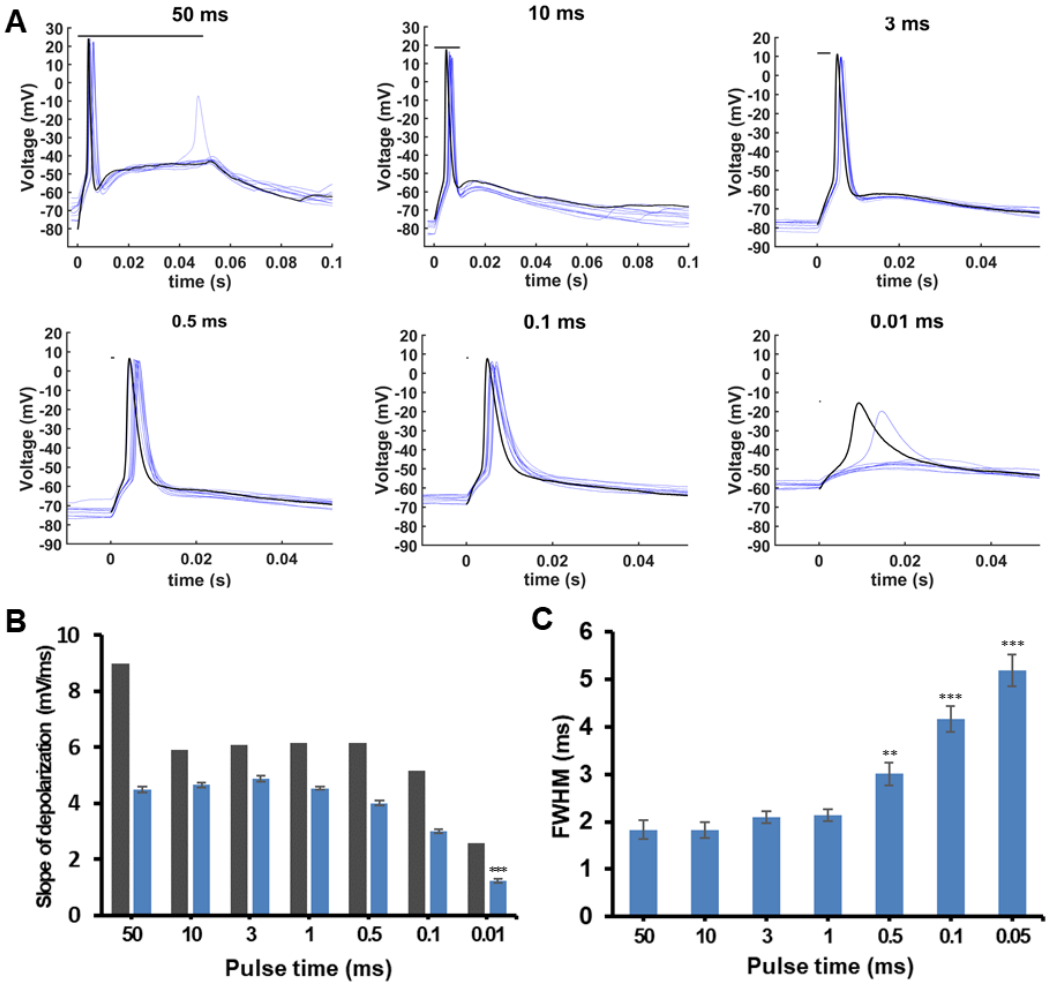

Figure 3.5 Electrophysiological characteristics of ChR2opt-mKATE-AT under a series of light pulses ranging from 50 ms to 0.01 ms in current clamp mode when expressed in primary neurons.

(**A**) Spike trains driven by blue light with a series of light pulses as indicated. Interpulse time was 1000 ms, N = 10. For each pulse time, the first trace is shown in black, and the other nine traces are shown in blue.

(**B**) The slopes of depolarization by blue light, which were determined by linearly fitting the voltage traces within the first 3 ms from the light onset. The histogram shows the value of the first spike (black bar) and the average value of the other nine spikes (blue bar) for each pulse time. The average values are shown as mean ± SD, N = 9.

(**C**) The full width at half maximum (FWHM) of action potentials elicited by different light pulses. The histogram compares the value of the first spike. The data are presented as mean ± SD, N = 10. For (B) and (C), Kruskal-Wallis One-Way ANOVA test, $^{**}p < 0.01$, $^{***}p < 0.001$, against the value in the group with a 50 ms light pulse.

Next, the optogenetic manipulation with another different series of blue light pulses was investigated in ChR2op-mKATE-AT-expressing neurons and the corresponding signals were recorded in voltage clamp mode. The light pulses used this time were in a large range, which were 1000 ms, 500 ms, 100 ms, and 50 ms in order. The optogenetic stimulations were conducted at 1000 ms interpulse intervals for twenty repeats, and the first five current traces are shown in **Figure 3.6A** and the zoom-in image of the second spikes is shown together in

Figure 3.6E. When blue light was switched on, the photocurrents increased rapidly and they triggered voltage-gated sodium currents within a few milliseconds, forming extremely large peak currents. Subsequently, the currents dropped dramatically, then after a slight increase the currents went into plateaus that persisted as long as the light was on. At light-off, the currents decreased promptly along with the closure of the channel. The data showed that optogenetic stimulation with these light pulses can trigger firing with high fidelity and high accuracy in neurons.

The time constant of channel closure (τ_{off}) indicates how fast a channel closes after the light is off, which is critical for the precise depolarization performance. Here the τ_{off} of ChR2op-mKATE-AT after exposing different pulses of blue light were measured. τ_{off} was determined by exponentially fitting the current traces after light-off. The values of individual spikes were plotted in **Figure 3.6B**. When the pulse time of light stimulation was 1000 ms, the duration of closure increased steadily from 13.78 ± 0.01 ms of the first stimulation to 32.39 ± 0.10 ms of the last stimulation, and this was the first round of optogenetic control. For the other three cases of stimulation with 500 ms, 100 ms, and 50 ms light pulses, the duration of closure displayed fluctuations, but all of them were in the range between 19 ms and 33 ms. Thus, the initial dark-adapted channel closed fastest, then the rate gradually slowed down a little. After a series of stimulation like this, the rate of channel closure eventually fluctuated around a stable level.

The average duration of channel closure after illumination with each pulse time was estimated, and the results are shown in **Figure 3.6C**. The values for stimulation with 1000 ms, 500 ms, 100 ms, and 50 ms pulses were 24.79 ± 5.80 ms, 26.28 ± 3.82 ms, 24.16 ± 1.98 ms, and 23.41 ± 2.11 ms (mean ± SD), respectively (**Table 3.1**). The mean τ_{off} under illuminations with these light pulses were all around 25 ms, and there was no significant difference between these groups. Hence, in the investigated range of light pulses, the closure time of channelrhodopsin was not related to the duration of pulse time.

In response to blue light, a peak photocurrent should be elicited first by channelrhodopsin, then it desensitizes to a steady photocurrent. In this experiment, the activated action potential covered up the peak photocurrent, so it was impossible to identify it. Then the steady photocurrents under these light pulses of stimulation were compared. The average values for stimulation with 1000 ms, 500 ms, 100 ms, and 50 ms pulses were 351.24 ± 54.72 pA, 201.19 ± 12.56 pA, 148.62 ± 9.67 pA, and 123.16 ± 10.16 pA (mean ± SD), respectively, as shown in **Figure 3.6D**. The values are summarized in **Table 3.1.** Combined with the amplified spike traces shown in **Figure 3.6E**, these data suggested that in response to this kind of optogenetic manipulation the steady photocurrents decayed slowly over time.

Table 3.1 The τ_{off} and I_{steady} of ChR2op-mKATE-AT upon illumination with different light pulses. Data are presented as mean ± SD, N = 20.

Items \ Pulse time	1000 ms	500 ms	100 ms	50 ms
τ_{off} (ms)	24.79 ± 5.80	26.28 ± 3.82	24.16 ± 1.98	23.41 ± 2.11
I_{steady} (pA)	351.24 ± 54.72	201.19 ± 12.56	148.62 ± 9.67	123.16 ± 10.16

Taken together, the ChR2opt-mKATE-AT has high temporal precision in response to different blue light pulses ranging from submillisecond to second when expressed in primary neurons. Therefore, the targeting motif AT sequence did not affect the temporal accuracy of channelrhodopsin when applied for optogenetic manipulation. For a further discussion, see Section 5.1.2.

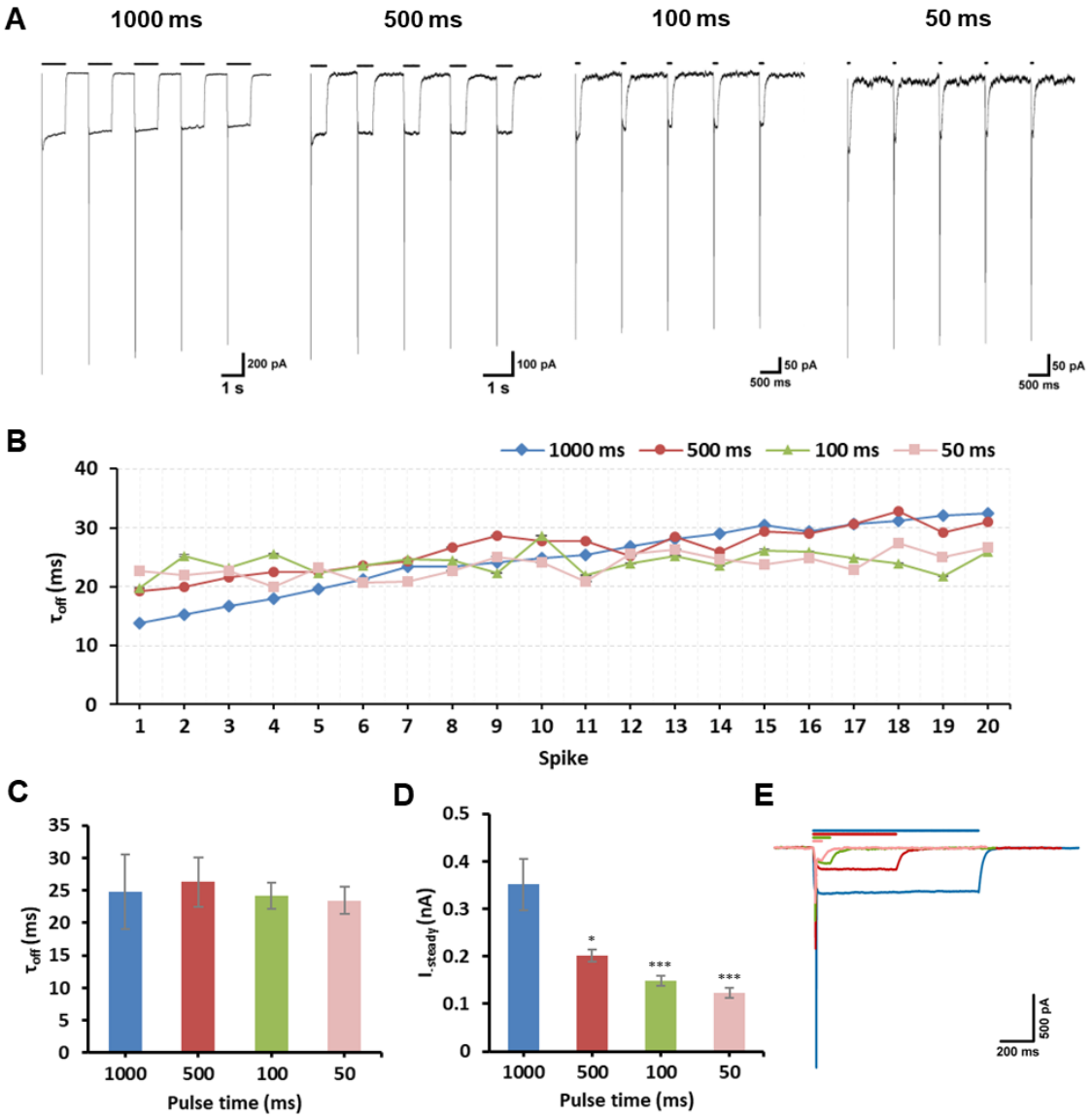

Figure 3.6 Electrophysiological characteristics of ChR2opt-mKATE-AT under a series of light pulses ranging from 1000 ms to 50 ms in voltage clamp mode when expressed in primary neurons.

(**A**) Current traces of ChR2opt-mKATE-AT in response to different blue light pulses, lasting 1000 ms, 500 ms, 100 ms, or 50 ms. Interpulse time was 1000 ms, N = 5/20.

(B) The time constant of channel closure (τ_{off}) of individual spikes after being exposed to different light pulses, which was determined by exponentially fitting the current traces after light-off.

(**C**) The average values of τ_{off} after being exposed to different light pulses. Data are presented as mean ± SD, N = 20. Kruskal-Wallis One-Way ANOVA test, $p > 0.05$.

(**D**) The average values of steady photocurrents in response to different light pulses. Data are presented as mean ± SD, N = 20. Kruskal-Wallis One-Way ANOVA test, $^{*}p < 0.05$, $^{***}p < 0.001$, against the value in the group with a 1000 ms pulse time.

(**E**) The second spike triggered by light stimulation with different light pulses.

3.4.2 Light power intensity

The next critical factor investigated was light power intensity, which can indicate the light sensitivity of channelrhodopsin. The purpose is to find out the optimal light power intensity to ensure a proper number of photons can be delivered to cells. If the applied light power intensity is too low, there are not sufficient channels activated, so it will affect the effectiveness of the operation. But if the intensity is too high, it will produce phototoxicity to cells. Thus, an ideal light power intensity is that it can induce the optical signal effectively with minimal side effects. In this section, the pulse time of blue light used was 20 ms, which was sufficient to trigger action potentials with high fidelity based on the result of the last section. Here, different light output powers ranging from 3 mW to 0.015 mW were used to illuminate neurons expressing ChR2opt-mKATE-AT ten times at 1000 ms interpulse intervals. The power stated here is the power of the laser beam. The diameter of the laser spot size was adjusted to about 12 μm.

The corresponding signals elicited by light illumination were recorded in current clamp mode and are displayed in **Figure 3.7A**. For each light power intensity, the first spike is shown in a black trace, and the other nine traces are shown in blue traces. All of the blue light in different output powers have successfully evoked action potential in ten stimulations. The configurations of all traces triggered by the same light power intensity were similar, and the first spike responded much faster than the other nine spikes.

Then the slopes of depolarization triggered by different powers of blue light illuminations were evaluated. The extracted voltage traces were from the beginning of light-on to the starting point of the rising phase of the action potential. The slope of depolarization was determined by linearly fitting the voltage trace. The results are shown in **Figure 3.7B**. With a higher light output power, the channelrhodopsin depolarized membrane faster. When light output power was 3 mW, the channelrhodopsin depolarized membrane fastest, which were about 7.24 mV/ms and 3.87 mV/ms for the first spike and subsequent spikes, respectively. Even when using a quite low light output power of 0.015 mW, the ChR2opt-mKATE-AT can be activated and APs can be triggered successfully, although the speed of depolarization was much slower compared with that in other cases. When the light output power was 0.015 mW, the rates of depolarization were about 1.56 mV/ms and 0.77 mV/ms for the first spike and subsequent spikes, respectively. The difference in the slopes of depolarization arose from the fact that different numbers of ChR2opt-mKATE-AT were activated under different light power intensities.

Two time parameters, time-to-threshold and time-to-peak, of the voltage traces elicited by light with different power intensities were also compared, which are partially displayed in **Figure 3.7C** and **Figure 3.7D,** respectively. Among them, the values of the first spikes were plotted separately from the other nine spikes, as the first spikes behaved much faster than the others. When illuminating cells with a 3 mW light output power, the voltage required the shortest average time to reach the threshold and peak, which were 6.90 ± 0.40 ms and 8.22 ± 0.43 ms (mean ± SD), respectively. These two time parameters increased slightly when the light output power decreased from 3 mW to 0.5 mW. But when the light output power dropped to 0.015

mW, the response of voltage became noticeably slower. On average it took 17.11 ± 1.31 ms and 20.02 ± 1.23 ms to reach the threshold and peak, respectively. Significant differences were observed when the output powers were larger than 1 mW compared with the group with 3 mW output power. The time-to-threshold and time-to-peak of the first voltage trace showed a similar trend to the average one, except that the time parameters required to reach the threshold and peak value were slightly shorter. In general, the 2 mW output power was suitable to achieve efficient optogenetic manipulation by using ChR2opt-mKATE-AT (see Section 5.1.2 for discussion).

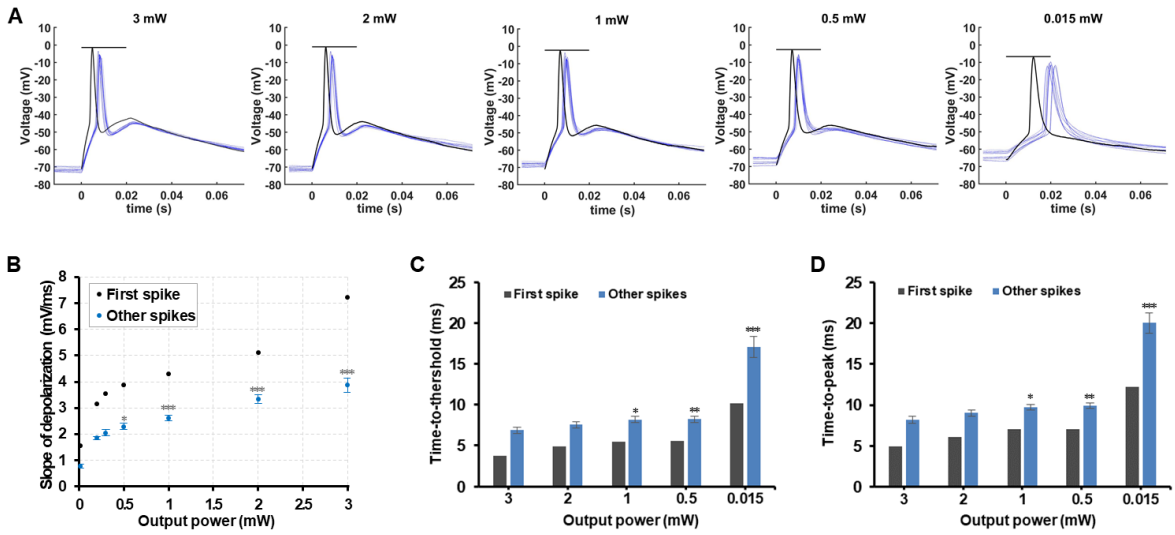

Figure 3.7 Electrophysiological characteristics of ChR2opt-mKATE-AT under light stimulation with a series of output powers ranging from 3 mW to 0.015 mW in current clamp mode when expressed in primary neurons. The diameter of the laser spot size was around 12 µm.

(**A**) The voltage traces driven by light pulses across various output powers as indicated. Pulse time was 20 ms, and interpulse time was 1000 ms. First trace, black line; other nine traces, blue line.

(**B**) The slope of the first depolarization (black) and the average slope of the subsequent nine depolarizations (blue) by blue light with different output powers. The average values of the other nine spikes are presented as mean ± SD, N = 9.

(**C**) The time-to-threshold of the first spike (black) and the average time-to-threshold value of the other nine spikes (blue) induced by light with intensity series.

(**D**) The time-to-peak of the first spike (black) and the average time-to-peak value of the other nine spikes (blue) under different light output powers. For (B-D), the corresponding average values of the nine spikes are presented as mean ± SD, N = 9. Kruskal-Wallis One-Way ANOVA test, $^{*}p < 0.05$, $^{**}p \leq 0.01$, $^{***}p \leq 0.001$, against the value in the group with a 3 mW light output power.

3.4.3 Stimulus frequency

The firing rates of different nerve cells at physiological conditions are in a relatively large range, and the ideal optogenetic operation should match the speeds of various physiological activities to mimic natural firing patterns. The influence of different stimulus frequencies was evaluated here. The pulse time of blue light used was 10 ms, and the interpulse intervals were 990 ms, 90

ms, 40 ms, 23 ms, and 10 ms, leading to 1 Hz, 10 Hz, 20 Hz, 30 Hz, and 50 Hz stimulation frequencies, respectively. The signals of ChR2opt-mKATE-AT evoked by blue light in neurons were recorded in the current clamp mode. The typical configuration of voltage traces in regular-spiking neurons is shown in **Figure 3.8A**. The quantitative analyses were conducted as well and the results are summarized in a histogram as shown in **Figure 3.8B**. When the stimulus frequency was 1 Hz, the probability of triggering an action potential was 100%, indicating that it was always successful to trigger an action potential under 1 Hz stimulus frequency. For 10 and 20 Hz stimulus frequencies, the probabilities of triggering an action potential were 81.67 ± 18.33% and 78.33 ± 21.67% (mean ± SEM), respectively, showing in most cases the action potentials can be evoked under these stimulus frequencies. The percentages of evoked spikes were only 15.00 ± 5% and 5 ± 0% under 30 Hz and 50 Hz stimulus frequencies, respectively, which meant that it was difficult to elicit action potentials with high reliability under these stimulus frequencies. Therefore, the stimulus frequency should be no more than 20 Hz to obtain action potentials with high fidelity in these cells.

The plateau potentials of voltage traces across different stimulus frequencies were investigated as well (**Figure 3.8C**). Plateau potential is the voltage difference from the trough of voltage between pulses to the voltage baseline without stimulation. The plateau potential represents a sustained depolarization state. After light stimulation with 1 Hz frequencies, the plateau potential was around 0.44 ± 0.27 mV (mean ± SEM), which indicated that after each stimulation at this frequency, the potential could go back to the resting potential level. When the light stimulus frequencies were 10 Hz and 20 Hz, the membrane voltages stayed at the level of 7.39 ± 2.22 mV and 21.05 ± 1.36 mV higher than the baselines, respectively. When using higher light stimulus frequencies 30 Hz and 50 Hz, the plateau potentials were blocked at the level of nearly 30 mV. Thus, using the higher light stimulation frequency, the larger the plateau potential would be. This was because the continuous light stimulation resulted in a constant proportion of light-activated channels being open and that blocked the potential in a depolarization state, inactivating voltage-gated sodium channels in regular-spiking neurons during the stimulation period. Also, after light-off the potential was unable to repolarize completely within the short interpulse time under high stimulus frequency, leading to failure to generate further action potentials.

In fact, the induced optogenetic performance is not only related to the properties of the channelrhodopsin but also to the intrinsic firing pattern of the nerve cells. In regular-spiking neurons, the high-frequency stimulation was hard to trigger continuous high-fidelity firings. But in another two firing pattern nerve cells, fast-spiking and burst-spiking neurons [199, 200], the situations were different (see Figure A.3). In fast-spiking nerve cells, the illumination with a high frequency of 50 Hz still could evoke action potentials with high reliability. In burst-spiking neurons, continuous illumination could even evoke multiple action potentials in succession during the illumination time. Therefore, the ChR2opt-mKATE-AT can be used in multiple firing patterns of neurons, but for neurons whose membrane potentials are easily

blocked by depolarization, the high-frequency stimulation is not feasible (see Section 5.1.2 for discussion).

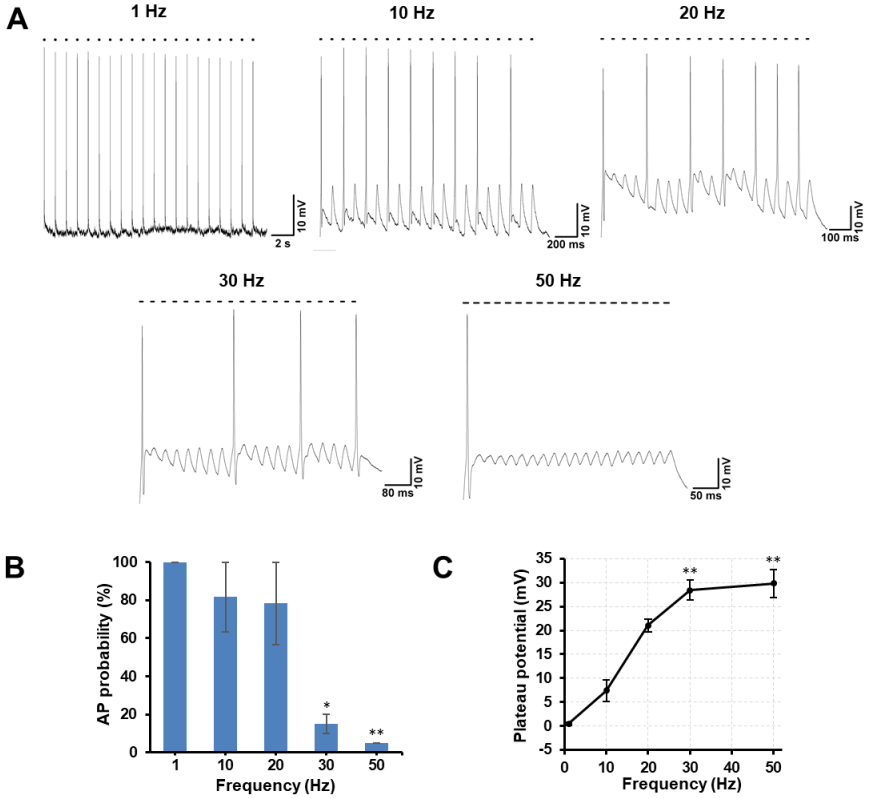

Figure 3.8 Electrophysiological characteristics of ChR2opt-mKATE-AT across light stimulus frequencies from 1 Hz to 50 Hz in current clamp mode when expressed in primary neurons.

(**A**) Voltage traces showing spikes recorded in current-clamped cortical neurons evoked by 1 Hz, 10 Hz, 20 Hz, 30 Hz, and 50 Hz trains of light pulses. Pulse time was 10 ms, and interpulse times were 990 ms, 90 ms, 40 ms, 23 ms, or 10 ms.

(**B**) The proportion of successfully evoked spikes out of twenty stimulations at different stimulus frequencies.

(**C**) The plateau potential amplitudes at different stimulus frequencies. For (B) and (C), data are presented as mean ± SEM, n = 3. Kruskal-Wallis One-Way ANOVA test, $^{*}p < 0.05$, $^{**}p < 0.01$, against the value at 1 Hz.

3.5 Electrophysiological characterization of ChR2opt-mKATE-AT compared with ChR2opt-mKATE

3.5.1 In neurons

To compare the electrophysiological characteristics of ChR2opt-mKATE-AT and ChR2opt-mKATE directly, the performances of ChR2opt-mKATE-AT and ChR2opt-mKATE were compared when expressed in neurons. In this part, voltage-gated sodium channels were inactivated by lidocaine to avoid interference deriving from action potentials, as the large current or voltage amplitude of action potential can cover the relatively small traces of

channelrhodopsins. First, the photocurrents evoked by illumination were evaluated. A representative photocurrent configuration generated by ChR2opt-mKATE-AT upon 1 s continuous blue light illumination is shown in **Figure 3.9A**(b), which displayed a similar shape to that by ChR2opt-mKATE as shown in **Figure 3.9A**(a). In response to blue light, a peak current was generated initially, then it desensitized into a steady current in a few milliseconds. At light-off, the current went back to the original level.

Two current amplitudes, peak current (I_{peak}) and steady current (I_{steady}), are summarized in **Figure 3.9B**(a). The amplitudes of steady currents evoked by ChR2opt-mKATE and ChR2opt-mKATE-AT were 304.39 ± 9.55 pA and 436.78 ± 50.93 pA (mean ± SEM), respectively, whereas the corresponding amplitudes of peak currents were 687.93 ± 38.30 pA and 810.9 ± 22.84 pA (mean ± SEM), respectively. The amplitudes of both steady and peak currents generated by ChR2opt-mKATE-AT were significantly larger than that by ChR2opt-mKATE. The ratios of steady currents to peak currents, also known as the level of desensitization, were comparable in these two cases, and they were 0.55 ± 0.01 and 0.57 ± 0.04 (mean ± SEM) for ChR2opt-mKATE and ChR2opt-mKATE-AT, respectively (**Figure 3.9B**(b)).

The kinetics of ChR2 are critical factors in achieving temporally precise manipulation of membrane potential. The speed of membrane potential change induced by ChR2 is associated with channel kinetics. Thus the kinetics including the time constant of channel opening (τ_{on}), desensitization (τ_{des}), and closing (τ_{off}) were also compared. The time constants of channel opening for ChR2opt-mKATE and ChR2opt-mKATE-AT were 1.48 ± 0.22 ms and 1.13 ± 0.18 ms (mean ± SEM), respectively (**Figure 3.9C**(a)). The desensitization constants of ChR2opt-mKATE and ChR2opt-mKATE-AT were 25.69 ± 2.78 ms and 23.83 ± 2.03 ms, respectively (**Figure 3.9C**(b)). The time constants of channel closing for ChR2opt-mKATE and ChR2opt-mKATE-AT were 17.26 ± 0.67 ms and 18.43 ± 1.38 ms, respectively (**Figure 3.9C**(c)). There was no significant difference between these kinetics in these two groups.

Thus the photocurrents produced by ChR2opt-mKATE-AT were a little larger than that by ChR2opt-mKATE. This may be caused by more distributions of channelrhodopsins at soma regions after being fused with the targeting motif AT. In this case, the illumination with the same spot size on soma would activate more channelrhodopsins, thereby producing larger photocurrents (see Section 5.1.3 for discussion).

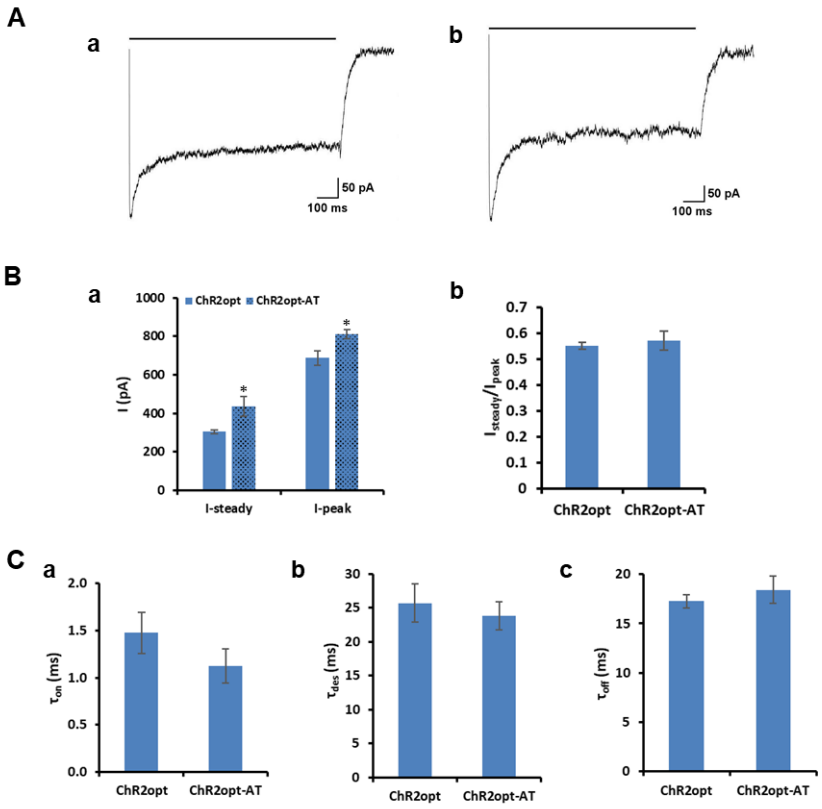

Figure 3.9 Electrophysiological characteristics of ChR2opt-mKATE and ChR2opt-mKATE-AT when expressed in neurons in voltage clamp mode.

(**A**) The representative traces of photocurrents generated by ChR2opt-mKATE (a) and ChR2opt-mKATE-AT (b) in response to a 1 s pulse of continuous blue light.

(**B**) (a) The steady and peak photocurrents of ChR2opt-mKATE and ChR2opt-mKATE-AT. n = 6 for each group. Mann-Whitney test for steady current and One-Way ANOVA test for peak current, $^{*}p < 0.05$, against the ChR2opt-mKATE group. (b) The ratios of steady current to peak current. n = 5 for each group. One-Way ANOVA test, $p > 0.05$.

(**C**) The average values of time constants of channels opening (a, n = 22 and 19), desensitization (b, n = 8 and 7), and closing (c, n = 11 and 7). All data are presented as mean ± SEM. Mann-Whitney test for τ_{on}, One-Way ANOVA test for τ_{des} and τ_{off}, $p > 0.05$.

In addition, the voltage changes elicited by the channel with and without targeting sequence AT were compared as well (see Figure A.4). The results showed that the voltage amplitudes induced by ChR2opt-mKATE-AT were larger than that by ChR2opt-mKATE, and the rate of depolarization was also faster. These data suggested further that there were more ChR2opt-mKATE-AT localized to the somatodendritic region compared with ChR2opt-mKATE when expressed in neurons.

3.5.2 In HEK293 cells

The electrophysiological characteristics of ChR2opt-mKATE-AT and ChR2opt-mKATE were also investigated in another cell type, Human Embryonic Kidney 293 (HEK293) cell. **Figure**

3.10A displays two typical photocurrent traces produced by ChR2opt-mKATE and ChR2opt-mKATE-AT upon 1 s blue light illumination and their configurations were similar. The amplitudes of peak current (I_{peak}) and steady current (I_{steady}) are summarized in a histogram as shown in **Figure 3.10B**(a). The steady current and peak current elicited by ChR2opt-mKATE-AT were 289.25 ± 64.13 pA and 480.04 ± 110.86 pA (mean ± SEM), respectively, which were comparable to the corresponding values of ChR2opt-mKATE (280.93 ± 79.01 pA and 448.05 ± 123.37 pA, respectively). The ratios of the steady current to the peak current were 0.66 ± 0.02 and 0.60 ± 0.02 (mean ± SEM) for ChR2opt-mKATE and ChR2opt-mKATE-AT, respectively, as displayed in **Figure 3.10B**(b). This suggested that the desensitization levels of ChR2opt-mKATE and ChR2opt-mKATE-AT were equal. Besides, their kinetics were compared as seen in **Figure 3.10C**. The time constants of channel opening for ChR2opt-mKATE and ChR2opt-mKATE-AT were 0.51 ± 0.04 ms and 0.49 ± 0.05 ms (mean ± SEM), respectively (**Figure 3.10C**(a)). The desensitization constants of ChR2opt-mKATE and ChR2opt-mKATE-AT were 13.60 ± 1.97 ms and 13.29 ± 2.86 ms, respectively (**Figure 3.10C**(b)). The time constants of channel closing for ChR2opt-mKATE and ChR2opt-mKATE-AT were 15.14 ± 1.07 ms and 13.35 ± 0.87 ms, respectively (**Figure 3.10C**(c)). All these kinetics were at equal levels in the targeted and untargeted groups.

These results showed that both the amplitudes and the kinetics of photocurrents generated by ChR2opt-mKATE and ChR2opt-mKATE-AT were comparable in HEK293 cells. Therefore, these results indirectly indicated that the expression levels of these two proteins were comparable in the HEK293 cells. In addition, the signals recorded in current clamp mode were also investigated (see Figure A.5), which suggested that both the amplitudes and the slopes of depolarization of voltage changes elicited by ChR2opt-mKATE and ChR2opt-mKATE-AT were similar, supporting the above conclusion. For a further discussion on the electrophysiological characteristics of ChR2opt-mKATE-AT, see Section 5.1.2, and see more on expression vs. localization in Section 5.1.3.

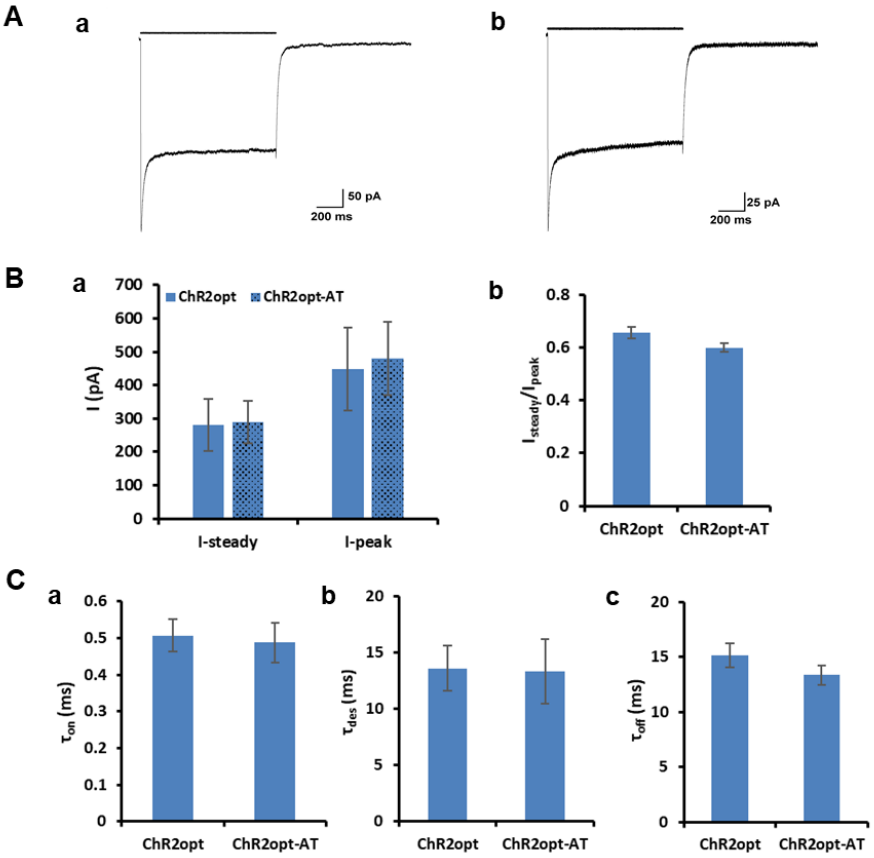

Figure 3.10 Electrophysiological characteristics of ChR2opt-mKATE and ChR2opt-mKATE-AT when expressed in HEK293 cells in voltage clamp mode.

(**A**) The representative traces of photocurrents generated by ChR2opt-mKATE (a) and ChR2opt-mKATE-AT (b) in response to a 1 s pulse of continuous blue light.

(**B**) (a) The steady and peak photocurrents of ChR2opt-mKATE and ChR2opt-mKATE-AT. n =7 and 8. (b) The ratios of steady current to peak currents. n = 9 for each group.

(**C**) The average values of time constants of channels opening (a, n = 8 and 8), desensitization (b, n = 10 and 6), and closing (c, n = 5 and 5). For (B) and (C), all data are presented as mean ± SEM. Mann-Whitney test for τ_{des}, and One-Way ANOVA test for others, $p > 0.05$.

3.6 The spatial specificity gained by using ChR2opt-mKATE-AT compared with ChR2opt-mKATE

After confirming the electrophysiological function of channelrhodopsin was not affected by AT sequence, if the spatial specificity can be achieved by using ChR2opt-mKATE-AT in neurons was determined. The neurons were electroporated with ChR2opt-mKATE or ChR2opt-mKATE-AT before being plated. The electrophysiological experiments were conducted around DIV10.

The corresponding results of neurons expressing ChR2opt-mKATE and ChR2opt-mKATE-AT are shown in **Figure 3.11A** and **Figure 3.11B**, respectively. Neurons in **Figure 3.11**(a) are

the patched cells expressing ChR2opt-mKATE or ChR2opt-mKATE-AT, showing ChR2opt-mKATE was distributed at both dendrites and axons while ChR2opt-mKATE-AT was mainly localized to somatodendrites, which were consistent with the results in Section 3.2.2 (Figure 3.3A). Light stimulation spots were at the soma and three different positions along the axon in each round, and the four positions are denoted in succession in the figures. The whole stimulations of 100 ms light pulse were conducted for twenty rounds at 900 ms interpulse intervals. Light-activated currents were recorded in voltage clamp mode at soma indicated by a triangle in the figure (**Figure 3.11**(a)).

The current traces triggered by light stimulations at four positions in the first round are displayed in **Figure 3.11**(b). For the photocurrents of ChR2opt-mKATE, they decreased gradually in sequence from position 1 to 4 (104.06 pA, 80.94 pA, 63.13 pA, and 60.94 pA in order), whereas for the photocurrents of ChR2opt-mKATE-AT they decreased obviously in the position 2, 3, and 4 (18.13 pA, 12.81 pA, and 16.56 pA in order) compared with that at position 1 (128.44 pA), although the photocurrents generated at position 1 in ChR2opt-mKATE-AT group were even larger than that in ChR2opt-mKATE group.

The individual amplitudes of currents elicited by light stimulations at different positions in twenty rounds are shown in **Figure 3.11**(c). Besides, the amplitudes were all normalized to the amplitude elicited by light stimulation at position 1, and the average values at each position are summarized in the histogram in **Figure 3.11**(d). The overall situations of the photocurrent amplitudes in the subsequent nineteen rounds were all similar to that in the first round in both two groups. The photocurrents of ChR2opt-mKATE decreased generally in sequence from position 1 to 4 in each round, and they all decreased gradually over the stimulation round. The average values were 100 ± 19.40%, 80.99 ± 11.95%, 66.40 ± 15.03%, and 61.13 ± 12.94% (mean ± SD) in sequence, as shown in **Figure 3.11A**(d). But the induced photocurrents of ChR2opt-mKATE-AT at positions 2 to 4 were much smaller (14.65 ± 2.68%, 11.66 ± 2.86%, and 11.61 ± 3.58% in order) than that at position 1 (100 ± 8.40%) in all twenty rounds, and the photocurrents also declined slightly over time (**Figure 3.11A**(d)).

Therefore, the photocurrents of ChR2opt-mKATE-AT evoked by light stimulation at the axon decreased evidently, but not the photocurrents of ChR2opt-mKATE, although the photocurrents elicited by light stimulation at the soma of ChR2opt-mKATE-AT-positive neurons were a little larger.

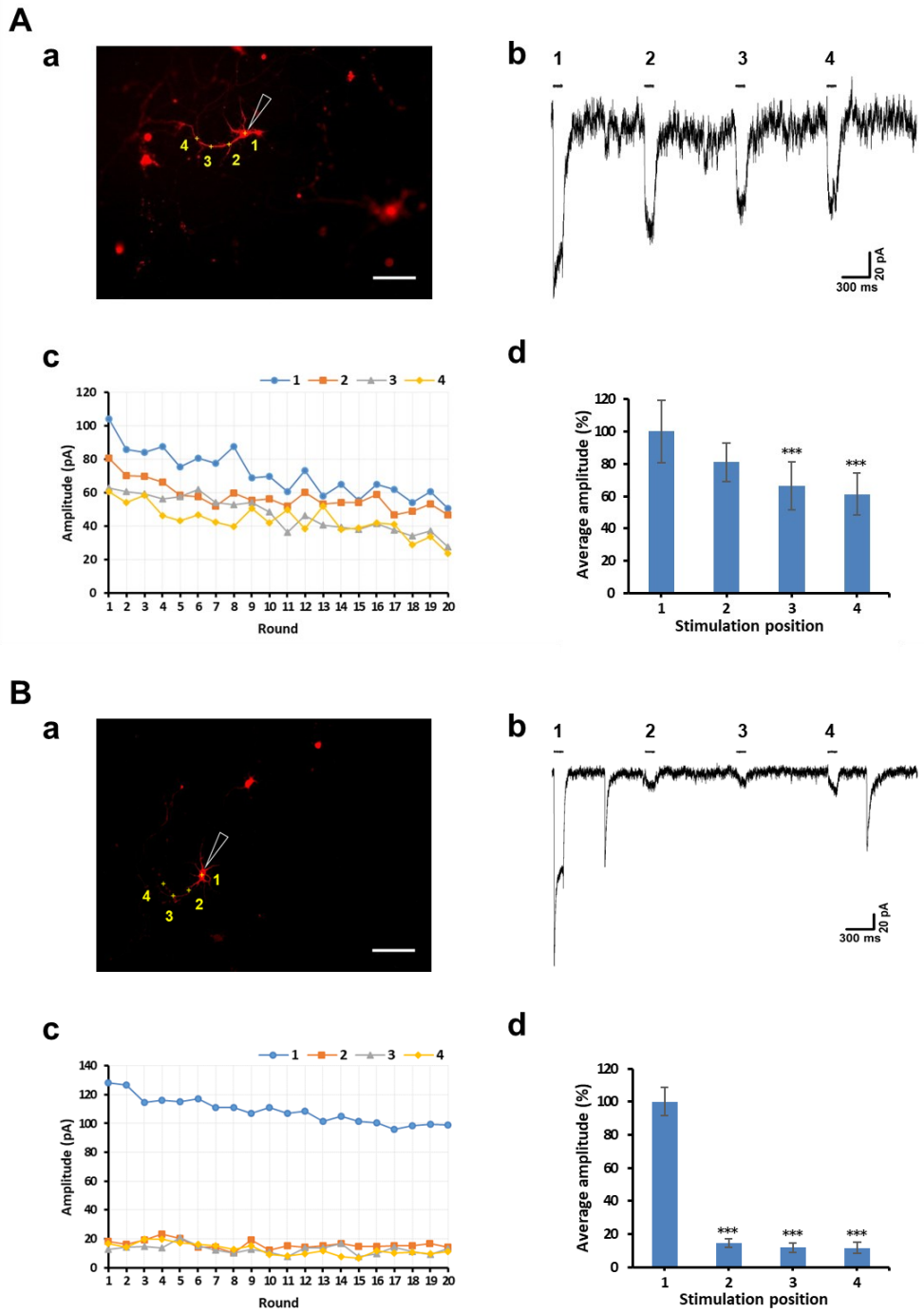

Figure 3.11 The spatial specificity achieved by using ChR2opt-mKATE-AT (**B**) compared with ChR2opt-mKATE (**A**) in neurons. Light stimulations were at the soma and three positions along the axon in each round and ran twenty rounds in total. The pulse time was 100 ms, and the interpulse time was 900 ms. The signals were recorded in voltage clamp mode at soma.

(**a**) The neuron transfected with ChR2opt-mKATE (A) and ChR2opt-mKATE-AT (B). The triangle represents the recording position by patch clamp. The numbers represent laser stimulation positions successively in one round. Scale bar, 100 μm.

(**b**) The current traces triggered by light stimulation at four positions (denoted as 1, 2, 3, and 4 in order) in the first round.

(**c**) The individual amplitudes of currents elicited by light stimulations at different positions in twenty rounds. (**d**) The average normalized amplitudes of currents triggered by light stimulation at each position in twenty rounds. The amplitudes were all normalized to the amplitude elicited by light stimulation at position 1. Data are presented as mean ± SD, N = 20. Kruskal-Wallis One-Way ANOVA test, $^{***}p < 0.001$, against the value at position 1.

The same light stimulation protocols but recorded in current clamp mode were also conducted, and the respective results of ChR2opt-mKATE and ChR2opt-mKATE-AT are shown in **Figure 3.12A** and **Figure 3.12B**. The light stimulation positions and recording positions were the same as described in voltage clamp mode. **Figure 3.12**(a) shows the voltage traces evoked by light illumination at four positions in the first round. The light-activated voltage amplitudes at different positions in twenty rounds are displayed in **Figure 3.12**(b). The average normalized amplitudes at each position are shown in **Figure 3.12**(c). Similar results to that obtained in voltage clamp mode were observed. The voltage amplitudes elicited by stimulation at positions 2 to 4 were regressively lower compared with that at position 1 in the case with ChR2opt-mKATE, whereas they dropped obviously in the case with ChR2opt-mKATE-AT. Hence, it was less likely to activate the neuron expressing ChR2opt-mKATE-AT when light stimulated its axon. In this way, interference from the closely packed axons can be avoided when stimulating a target neuron for mapping a specific neural circuit in a complex network. In summary, these results demonstrated that spatial specificity can be achieved by using ChR2opt-mKATE-AT in a dense neural network (see discussion in Section 5.1.3).

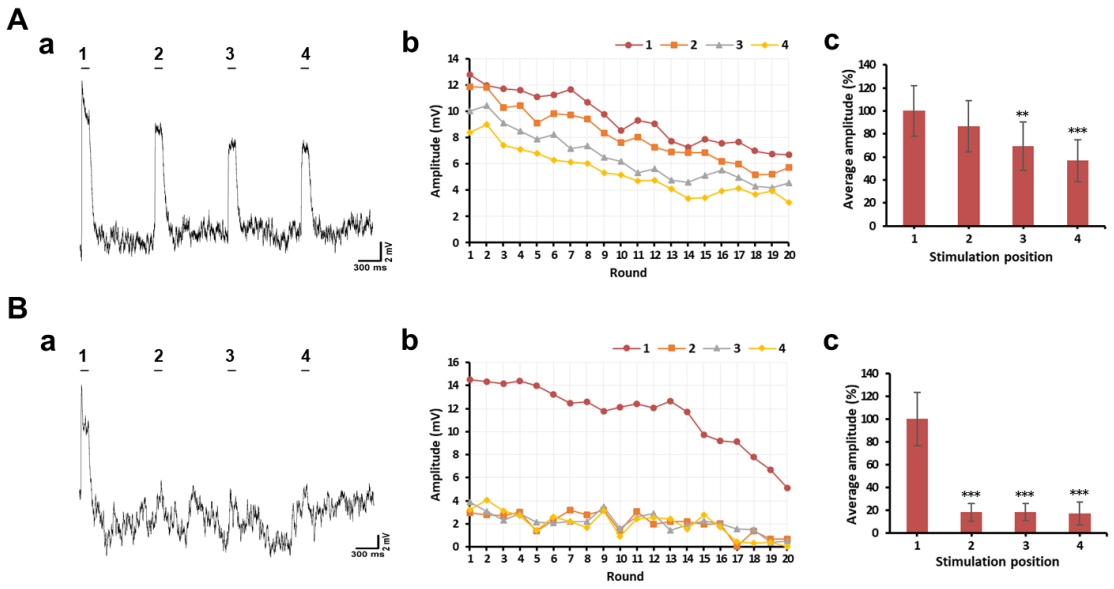

Figure 3.12 The spatial specificity achieved by using ChR2opt-mKATE-AT (**B**) compared with ChR2opt-mKATE (**A**) in neurons. Light stimulations were at the soma and three positions along the axon in each round and ran twenty rounds in total. The pulse time was 100 ms, and the interpulse time was 900 ms. The signals were recorded in the current clamp mode at soma.

(**a**) The voltage traces in response to light stimulation at four positions (denoted as 1, 2, 3, and 4 in order) in the first round.

(**b**) The individual amplitudes of voltages evoked by light stimulations at four positions in twenty rounds.

(**c**) The average normalized amplitudes of light-activated voltages at each position in twenty rounds. The amplitudes were all normalized to the amplitude induced by light stimulation at position 1. Data are presented as mean ± SD, N = 20. Kruskal-Wallis One-Way ANOVA test, $^{**}p < 0.01$, $^{***}p < 0.001$, against the value at position 1.

3.7 The retrograde trafficking of ChR2opt-mKATE-AT

To elucidate the underlying mechanism of the subcellular localization of ChR2opt-mKATE-AT in neurons, the cellular trafficking of both ChR2opt-mKATE and ChR2opt-mKATE-AT was observed in real time by performing live-cell imaging experiments. The cells could survive being monitored under live-imaging microscopy for a long time owing to the setup equipped with an incubation chamber with proper temperature, CO_2, and humidity controls which provide a proper environment for neuronal growth. Images were taken every 1 min for 2.5 h. The neurons captured at the beginning (0 h) and the end (2.5 h) are shown in big pictures on the left of each figure and zoom-in images every half hour are shown in small pictures on the right of each figure (**Figure 3.13**).

In ChR2opt-mKATE expressing neurons, ChR2opt-mKATE was located at both the somatodendrites and axon (**Figure 3.13A**), while in ChR2opt-mKATE-AT expressing neurons, ChR2opt-mKATE-AT primarily localized to the somatodendritic region (**Figure 3.13B**), as

indicated by the red fluorescence of mKATE. The positions of proteins at axon were indicated by blue arrowheads in the images. In **Figure 3.13A**, the indicated two protein positions in the axon at 0 h and 2.5 h were nearly the same. Thus, during the whole observation period, the positions of protein ChR2opt-mKATE were almost stationary in the axon, suggesting ChR2opt-mKATE can be stably present at the axon. While for ChR2opt-mKATE-AT, in the initial period of observation, the proteins were located at the axon far away from the soma (0 h, **Figure 3.13B**). Then the proteins moved gradually toward the soma over time. The longer the observation time, the closer the proteins are to soma. At the end of observation, the proteins moved back to the soma (2.5 h, **Figure 3.13B**). Thus, proteins ChR2opt-mKATE-AT could not stay steadily at the axon, instead they were trafficked back to soma. The speed was evaluated to be 0.0125 ± 0.002 μm/s (mean ± SEM, n = 3). Therefore, during the whole observation period, protein ChR2opt-mKATE can stably present at both somatodendrites and axons, whereas protein ChR2opt-mKATE-AT can only stably present at sometodendrites and the ones located at axons are transported back to soma quickly. For a further discussion, see Section 5.1.4.

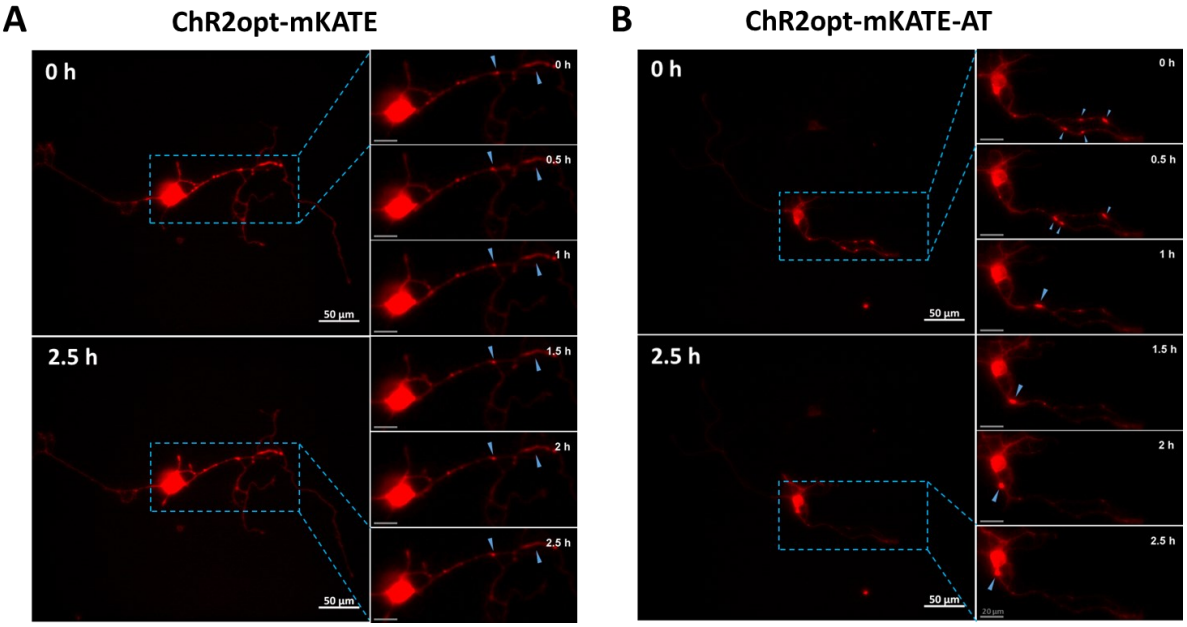

Figure 3.13 Live-cell images of neurons expressing ChR2opt-mKATE (**A**) and ChR2opt-mKATE-AT (**B**). Images were taken every 1 min for 2.5 h. The images captured at the beginning (0 h) and the end (2.5 h) of observation are shown in big pictures on the left. Zoom-in images every half hour are shown in small pictures on the right. The specific time point was indicated in each image. Blue triangles point to protein positions in real time. Scale bar, 50 μm in big pictures (left column), 20 μm in small pictures (right column).

4 Optogenetic actuator II

This chapter is about the second type of optogenetic actuator that was constructed based on the high current channelrhodopsin variant, ChR2XXL (D156C) (see Section 1.3.2.2). First, the specific strategy for the generation of TR5-ChR2XXL, TR10-ChR2XXL, and TR15-ChR2XXL constructs is described (**Section 4.1**). Then, the electrophysiological properties of the membrane in cells expressing these actuators were evaluated by detecting the current-voltage relationship (**Section 4.2.1**). Subsequently, the electrophysiological characteristics of these actuators were investigated with different recording modes (**Section 4.2.2**) or stimulation protocols (**Section 4.2.3**). After exploring the signal configurations under different interval times (**Section 4.2.4**), the light-induced electrical signals and relevant kinetics are compared (**Section 4.2.5**), as well as the currents produced in polarized cells (**Section 4.2.6**). Besides, the subcellular localization of these actuators in polarized cells was determined (**Section 4.3**). Lastly, their transfection efficiencies in different cell types are compared (**Section 4.4**). Portions of this chapter have been submitted for publication.

4.1 Construct generation

In this part, different numbers of tandem repeats (TR5, TR10, and TR15) from the extracellular region of human mucin protein were chosen as targeting motifs, as the TR sequence was proven to be an apical targeting signal in polarized epithelial cells as mentioned in Section 1.4.3. However, because of the high GC content and the highly-repetitive sequences they had, handling with these tandem repeats was challenging. The first problem met was that these mucin genes are hard to artificially synthesize, especially for TR15. Codon optimization was performed several times with manual adjustments to generate DNA that could be synthesized. Then these motifs were attached to the N-terminus of ChR2XXL in an empty vector using seamless cloning. Detailed protocols are seen in Section 2.1.2. The promoter used here was the CMV promoter. In order to identify cells expressing these proteins and assess their subcellular localizations, a yellow fluorescent protein (YFP) was fused to these channelrhodopsins (ChR2XXL-YFP, hereafter ChR2XXL). Another problem was that the generated plasmids with repeat construct were hard to express in *E.coli*. After testing several strains, NEB Stable Competent *E.coli* proved suitable for the isolation of plasmid clones containing repeat elements. Finally, three new plasmids encoding TR5-ChR2XXL-YFP, TR10-ChR2XXL-YFP, and TR15-ChR2XXL-YFP (hereafter TR5-ChR2XXL, TR10-ChR2XXL, and TR15-ChR2XXL, respectively) were obtained. The results were confirmed by DNA sequencing and restriction enzyme digestion (see Figure A.2 B and C). The schematics of these three constructs are shown in **Figure 4.1**.

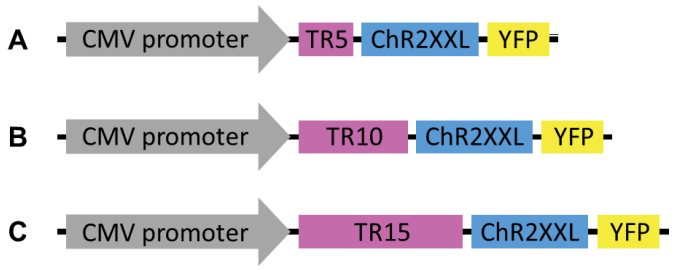

Figure 4.1 Schematics of ChR2XXL-YFP fused with TR5 (**A**), TR10 (**B**), and TR15 (**C**) from human mucin at its N-terminus. CMV promoter, Cytomegalovirus promoter that drives constitutive expression of genes under its control in mammalian cells; YFP, yellow fluorescent protein. In order to avoid interference from adjacent constructs, four amino acids (KLAT) were inserted as a linker between TR and ChR2XXL, and five amino acids (PAAAT) were inserted between ChR2XXL and YFP.

4.2 Electrophysiological characterization of optogenetic actuators when expressed in HEK293 cells

In order to investigate the electrophysiological characteristics of the constructed optogenetic actuators, these actuators were introduced into HEK293 cells. This cell line is a useful system for electrophysiology studies due to its low expression of native channels [201]. The electrophysiological characterizations were determined by using whole cell patch clamp technique, which allows the evaluation of the electrical excitability of cells and the functional properties of ion channels [202]. Since HEK293 cells are not polarized cells, a fixed illumination area could consistently probe comparable areas of channel expression in the membrane.

4.2.1 Current-voltage relationship of the membrane

The introduction of exogenetic channelrhodopsins may produce negative effects on the membrane property and cell morphology. Also the intrinsic cell membrane property strongly influences the level of membrane depolarization. Hence, it is necessary to ensure that the membrane properties are not affected by exogenetic proteins in particular for strong promoter-driven proteins. The membrane's current-voltage relationship can reflect if the properties are affected by the expression of TR-tagged ChR2XXL, so the relationship was investigated in HEK293 cells. **Figure 4.2A** shows a typical voltage trace triggered by current injection from -200 pA to 400 pA at 50 pA intervals in HEK293 cells expressing ChR2XXL. The voltage traces obtained in other groups expressing TR-ChR2XXL were all similar to this (data not shown). The current-voltage relationship was constructed by plotting steady state membrane voltage amplitudes versus injected currents, as shown in **Figure 4.2B**. The relationships in TR-tagged groups were similar to that in the ChR2XXL group, and there was no significant difference between these groups. These results suggested that the TR-ChR2XXL expression did not have an evident influence on the properties of the cell membrane in HEK293 cells.

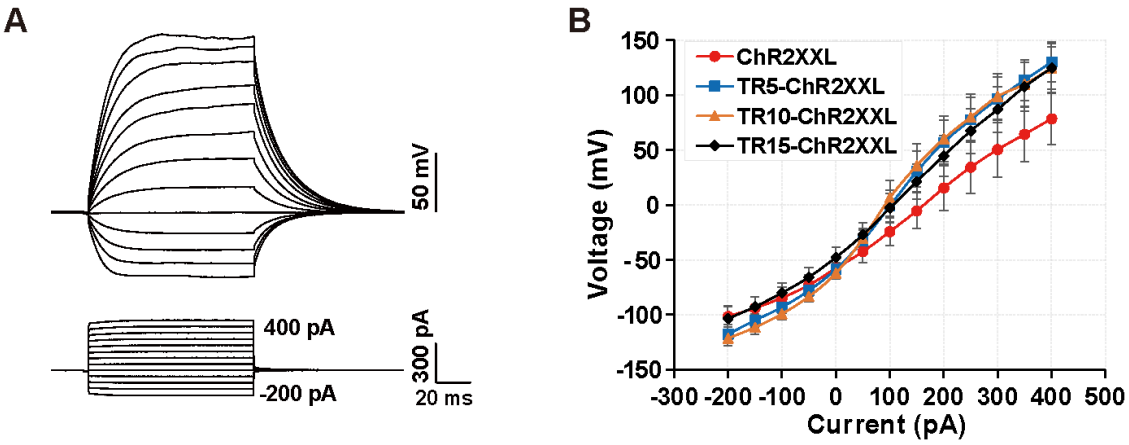

Figure 4.2 The voltage-current relationship of the cell membrane in HEK293 cells expressing ChR2XXL, TR5-ChR2XXL, TR10-ChR2XXL, and TR15-ChR2XXL.

(**A**) A typical voltage profile in HEK293 cells expressing ChR2XXL in response to current injection from -200 pA to 400 pA at 50 pA steps for 100 ms.

(**B**) Current-voltage relationship for HEK293 cells transfected with different optogenetic actuators. Data are presented as mean ± SEM. N = 7, 9, 11, and 8 for ChR2XXL, TR5-ChR2XXL, TR10-ChR2XXL, and TR15-ChR2XXL, respectively. Two-Way repeated ANOVA test, $p > 0.05$.

4.2.2 Record in different clamp modes

For optogenetic manipulation, a targetable laser device was combined with the patch clamp setup. The actuator-expressing HEK293 cells were illuminated with 1000 ms laser pulses for 20 overlays, separated by 1000 ms dark intervals, and recorded in voltage clamp mode. The first three channel activations in typical traces are displayed in **Figure 4.3A**, and the zoom-in picture of the first spikes is shown together in **Figure 4.3B**. Once illuminated, the currents increased rapidly in the very beginning, then gradually went into plateaus. At light-off, a small current increase appeared, making the photocurrents larger than that at light-on. Then the channels close extremely slowly. After a short dark period of 1 s, in response to the second light pulse the currents returned to the original plateau level, leading to decreased current magnitudes. The current traces of different actuators showed similar configurations, which indicated that the electrophysiological characteristics of the channelrhodopsin were not affected by the tandem repeats. The current changes elicited by the second to twentieth light pulses were quantitatively compared with the first additional small current peak produced at light-off. All later current amplitudes were normalized to the first extra current peak. The results are summarized in **Figure 4.3C**, the current changes triggered by later light pulses in HEK293 cells decreased gradually with more stimulations. This indicated a slight loss of the effectivity during this stimulation protocol over time (see also Discussion 5.2.1).

The stimulation was repeated with recordings in current clamp mode. **Figure 4.3D** shows the voltage traces during the first three channel activations, the first of which are zoomed and shown together for comparison in **Figure 4.3E**. The voltages increased rapidly in response to

the blue laser, then became steady in continuous illumination. When the laser was switched off, the voltages rose quickly, then diminished gradually. The laser pulses after 1 s break quenched the voltages to a level similar to the previously observed change in current. All actuators displayed similar voltage changes in response to this stimulation sequence. The voltage changes during the second to twentieth light pulses were normalized to the first small additional voltage peak as percentages, which were plotted in **Figure 4.3F**. These data demonstrated that the TR motifs did not affect the achieved current per area membrane, cell depolarization, nor accumulation of inactive channels of ChR2XXL, which could still introduce a continuous depolarization block to the cell membrane.

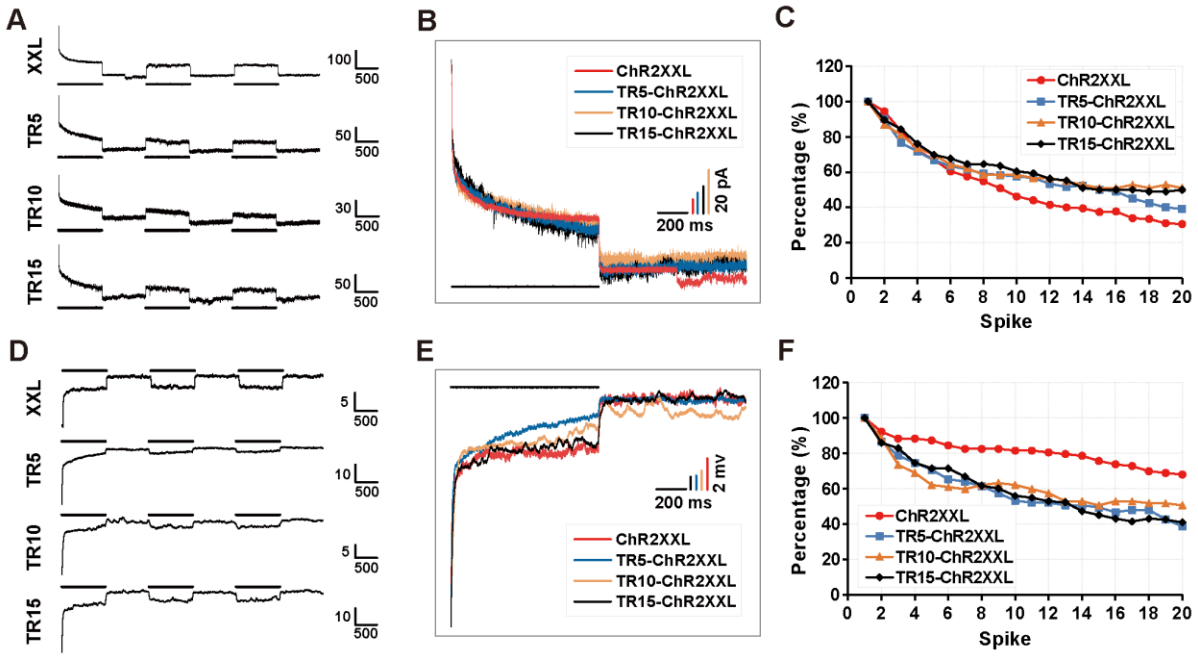

Figure 4.3 Optogenetic manipulation with 1000 ms light pulses at 1000 ms interpulse intervals in HEK293 cells.

(**A**) and (**D**) Current traces (scale pA per ms) and voltage traces (scale mV per ms) recorded from HEK293 cells expressing ChR2XXL, TR5-ChR2XXL, TR10-ChR2XXL, and TR15-ChR2XXL in voltage clamp mode (A) or current clamp mode (D) illuminated with 1000 ms light pulses (dashes), separated by intervals of 1000 ms. V_{hold} = -60 mV (A) and I_{hold} = -60 pA (D). In certain figures, ChR2XXL, TR5-ChR2XXL, TR10-ChR2XXL, and TR15-ChR2XXL are shortened as XXL, TR5, TR10, and TR15, respectively, which applies to all figures in this thesis.

(**B**) and (**E**) The magnified current traces (B) and voltage traces (E) elicited by the first light pulse in (A) and (D), respectively.

(**C**) and (**F**) The ratios of the current (C) or voltage (F) changes elicited by the second to twentieth light pulses to the first small additional peak. Individual current or voltage amplitudes were all normalized to the first small additional peak.

4.2.3 Stimulation at different intervals

Further recordings were made at different optogenetic stimulation intervals to determine the

properties of new constructs. Current traces recorded in HEK293 cells illuminated with 50 ms light pulses at two different interpulse intervals, 1950 ms and 3950 ms, were studied, leading to 0.5 Hz and 0.25 Hz stimulus frequencies, respectively. **Figure 4.4A** and **Figure 4.4D** show the partial current profiles elicited.

The first and second spike traces recorded at 0.5 Hz stimulus frequency (**Figure 4.4A**) are magnified in **Figure 4.4B** and **Figure 4.4C**, respectively, as merged images of four channelrhodopsins. As the plots show, the four traces were nearly accordant with the stimulation program, indicating that all four channelrhodopsins behaved uniformly. For the 0.5 Hz stimulation, the current changes of channelrhodopsins evoked at the beginning of individual light-on (except the first one) were normalized to the small current peak at first light-off, and the normalized percentages were plotted in **Figure 4.4E** (lines with circles). The average percentages for each channel are shown in **Figure 4.4F** (left bars), which were all about 85% of the first additional small spikes. For the 0.25 Hz stimulation, the corresponding results are shown in **Figure 4.4E** (lines with triangles) and **Figure 4.4F** (right bars) as well. The average values were around 65%, a little lower than that at 0.5 Hz stimulation. After staying in dark for 3950 ms, the states of channelrhodopsins were closer to the plateau states when blue light was on, leading to smaller current changes compared to that at 1950 ms interpulse intervals.

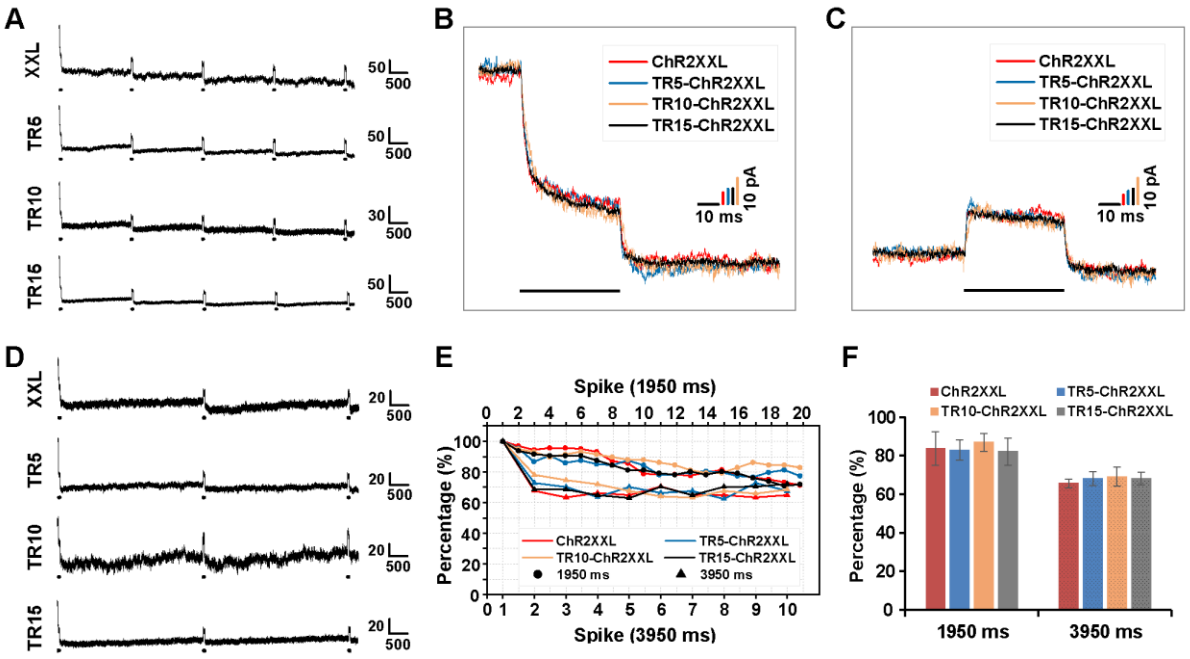

Figure 4.4 Optogenetic manipulation with 50 ms light pulses at 1950 ms or 3950 ms interpulse intervals in HEK293 cells.

(**A**) and (**D**) Current traces (scale pA per ms) recorded from HEK293 cells transfected with ChR2XXL, TR5-ChR2XXL, TR10-ChR2XXL, and TR15-ChR2XXL illuminated with 50 ms light pulses (dashes), separated by intervals of 1950 ms (A) or 3950 ms (D). V_{hold} = -60 mV.

(**B**) and (**C**) The magnified current traces triggered by the first (B) and second (C) light pulse (straight lines in black on the bottom) at 1950 ms interpulse intervals in (A).

(**E**) The ratios of the current changes elicited by light pulses other than the first one to the first small additional peak in (A) or (D). Individual current amplitudes were all normalized to the first small additional peak.

(**F**) The average ratios of other (except the first one) current changes to the first small additional peak in (A) or (D). 1950 ms, left bars; 3950 ms, right bars. Data are presented as mean ± SD, n = 19 for 1950 ms interpulse intervals and n = 9 for 3950 ms interpulse intervals. Kruskal-Wallis One-Way ANOVA test, $p > 0.05$ for both 1950 ms and 3950 ms groups.

4.2.4 Investigation of the interval time

To find out the sufficient interpulse time for channel closure, 50 ms pulse time at different interpulse intervals (4 s, 40 s, and 80 s) were explored with TR15-ChR2XXL, and the results are shown in **Figure 4.5**. In response to the first 50 ms blue light pulse, the photocurrents increased rapidly at first, then gradually went into plateaus. At light-off, a small current increase appeared. Then the channels closed at extremely slow rate. After a short dark period of 4 s, the channel was in a nearly fully open state since the photocurrent almost stayed at the same level as that at the first light-off. In response to the second light pulse the current went back to the original plateau level, leading to an inverse current change to the first light pulse (**Figure 4.5A**). After an intermediate interval time of 40 s, the channel was still in the open state as the photocurrent trace did not go back to the initial level before the first light-on, although in this

case the current was already smaller than that at the plateau. Upon the second illumination, the photocurrent went to the original plateau level as well (**Figure 4.5B**). After a long dark time of 80 s, the channels returned to the closed state as the photocurrent trace reached the initial level before the first light-on. In response to the second light stimulation, the current trace was nearly the same as the first one (**Figure 4.5C**). For all three intervals times, the currents triggered by the later light pulse were the same as the second one. The average current changes evoked by other light pulses except the first one were normalized to the first photocurrent, and the quantitative analysis is summarized in **Figure 4.5D**. The photocurrent in the same direction as the first one is displayed as a positive value, while that in the opposite direction to the first one is shown as a negative value. The normalized average currents elicited by light pulses except the first one were -29 ± 3.6%, 22.95 ± 1.77%, and 96.15 ± 0.75 (mean ± SD) for 4 s, 40 s, and 80 s interval time, respectively. These data showed that the kinetics of the channel closure was extremely slow and it closed completely within 80 s. In addition, these results demonstrated that no matter what state the channel was in before light-on, the photocurrent triggered by blue light always stayed at the same level.

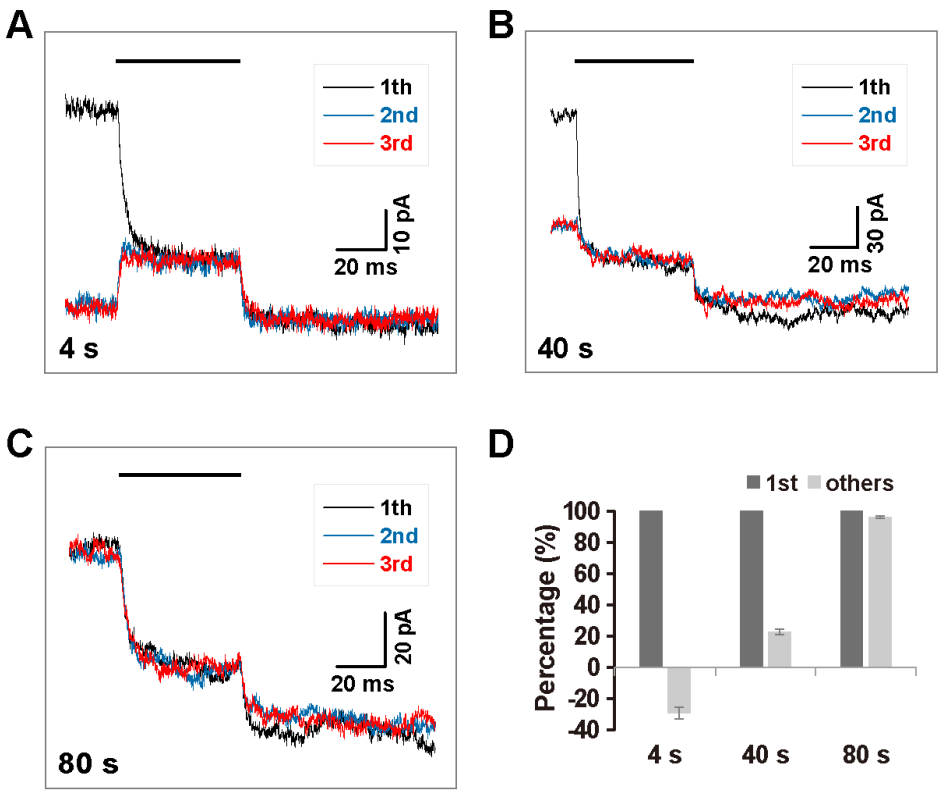

Figure 4.5 Optogenetic manipulation with 50 ms blue light pulses at different interpulse intervals in HEK293 cells.

(**A**-**C**) Current traces recorded from HEK293 cells transfected with TR15-ChR2XXL illuminated with 50 ms blue light pulses (straight lines in black on the top), separated by intervals of 4 s (A), 40 s (B), and 80 s (C).

(**D**) The normalized photocurrents to the current triggered by the first light pulse. Dark gray bars represent normalized first photocurrents. Light grey gray bars represent normalized average currents elicited by other light pulses. The positive value means the direction of the photocurrent is the same as the first one, and the negative value means the direction of the photocurrent is opposite to the first one. Data are presented as mean ± SD.

In Section 4.2.3, the photocurrent traces of ChR2XXL and TR-ChR2XXLs triggered by 50 ms light pulses at relatively short intervals (~ 2 s in Figure 4.4A and ~ 4 s in Figure 4.4D) are displayed and compared. Here the current traces of ChR2XXL and TR15-ChR2XXL illuminated with the same light pulse but at a longer interval time (80 s, **Figure 4.6**) are compared. The whole current traces are shown in **Figure 4.6A** and the zoom-in images at light-on are shown in **Figure 4.6B**. In response to this stimulation protocol, the current traces of these two actuators showed similar configurations. At light-on, the currents were triggered to a plateau level. At light-off, the photocurrents increased transiently, and then the channels closed quite slowly. These data further demonstrated that the electrophysiological characteristics of the channelrhodopsin were not affected by tandem repeats.

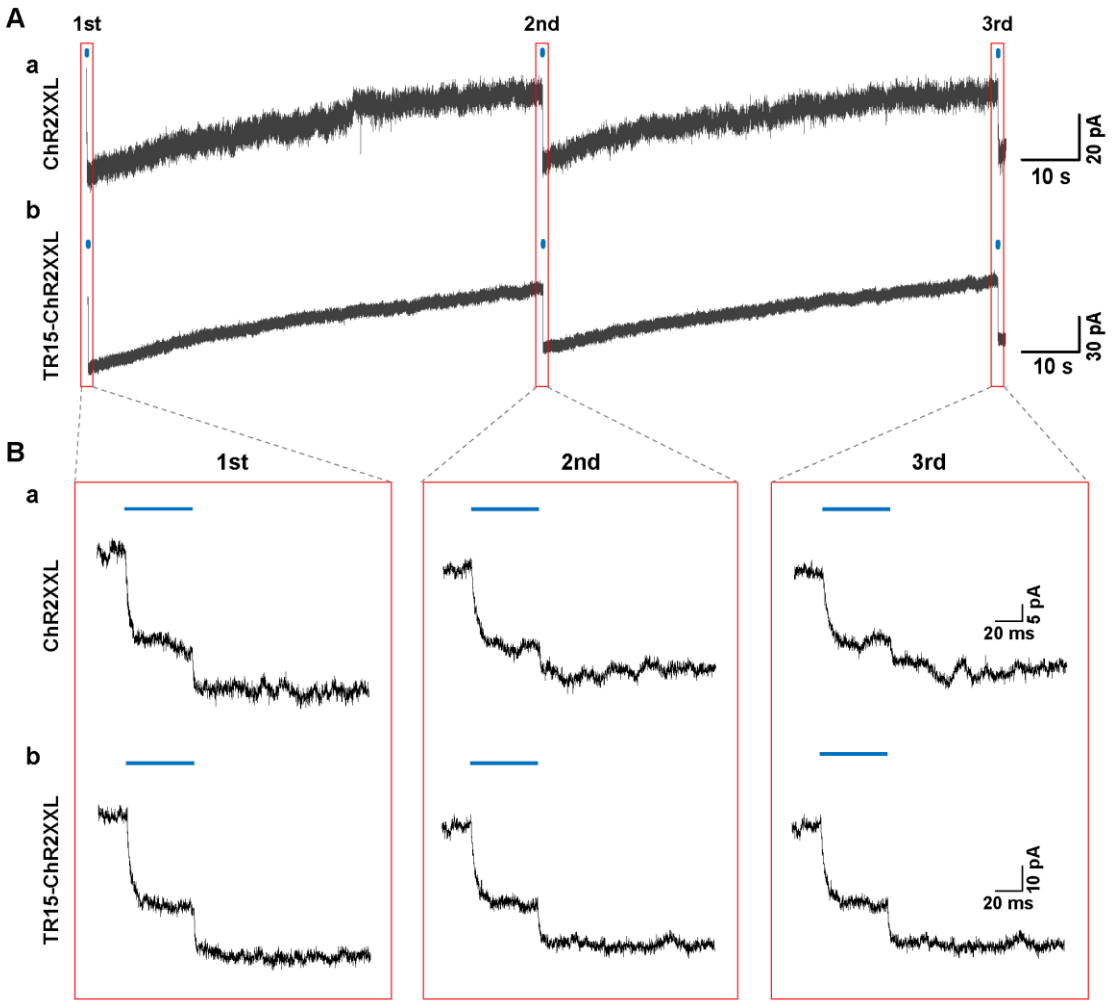

Figure 4.6 Optogenetic manipulation with 50 ms blue light pulse at 80 s interpulse intervals in HEK293 cells.

(**A**) The whole current traces recorded from HEK293 cells transfected with ChR2XXL (a) and TR15-ChR2XXL (b) illuminated with 50 ms blue light pulses (blue dots) at 80 s intervals.

(**B**) The magnified current traces of ChR2XXL (a) and TR15-ChR2XXL (b) triggered by the three light pulses (straight lines in blue) in order in (A).

4.2.5 Kinetics of optogenetic actuators

The photocurrent is a critical factor determining the effectiveness of ChR2 membrane depolarization. Hence, the currents of these channels evoked by blue light were compared. In order to give channels enough time to open and close, the pulse time and wait time here were 10 s and 80 s, respectively. **Figure 4.7A** shows inward photocurrents of four actuators triggered by 10 s of blue light in HEK293 cells recorded in voltage clamp mode. The histogram in **Figure 4.7B** presents the mean photocurrents generated by individual optogenetic tools, which were all normalized to the ChR2XXL group's current. Photocurrents in TR5-ChR2XXL, TR10-ChR2XXL, and TR15-ChR2XXL groups were 87.20 ± 7.58%, 73.54 ± 5.35%, and 88.56 ± 9.47% (mean ± SEM), respectively, all slightly smaller than that in ChR2XXL group (100 ±

17.84%), but there was no significant difference between groups.

The kinetics of channelrhodopsin are also important factors that play crucial roles in achieving precise manipulation of membrane potentials. Also many channelrhodopsin variants are specifically engineered with desired kinetics for different applications, so the effect of TRs on the current onset and offset time constants need to be evaluated. The time constant of channel opening upon light onset (τ_{on}) and the time constant of channel closure after light offset (τ_{off}) were determined by the exponential fit of corresponding rising or decaying photocurrent traces. The τ_{on} of TR5-ChR2XXL, TR10-ChR2XXL, and TR15-ChR2XXL were 3.57 ± 0.25 ms, 3.94 ± 0.26 ms, and 3.88 ± 0.34 ms (mean ± SEM), respectively, all slightly longer than that of ChR2XXL (3.32 ± 0.32 ms) (**Figure 4.7C**). With more TRs, the channel opened a little more slowly, but there was no significant difference between these groups. For the τ_{off} constant, the values of TR5-ChR2XXL, TR10-ChR2XXL, and TR15-ChR2XXL were 34.07 ± 3.25 s, 37.81 ± 2.50 s, and 42.05 ± 2.42 s, respectively (**Figure 4.7D**). The τ_{off} of ChR2XXL was 41.16 ± 2.95 s, which was comparable to other groups. There was no significant difference between these groups. Taken together, the various number of mucin tandem repeats did not have a remarkable impact on relevant kinetic parameters for the current generation.

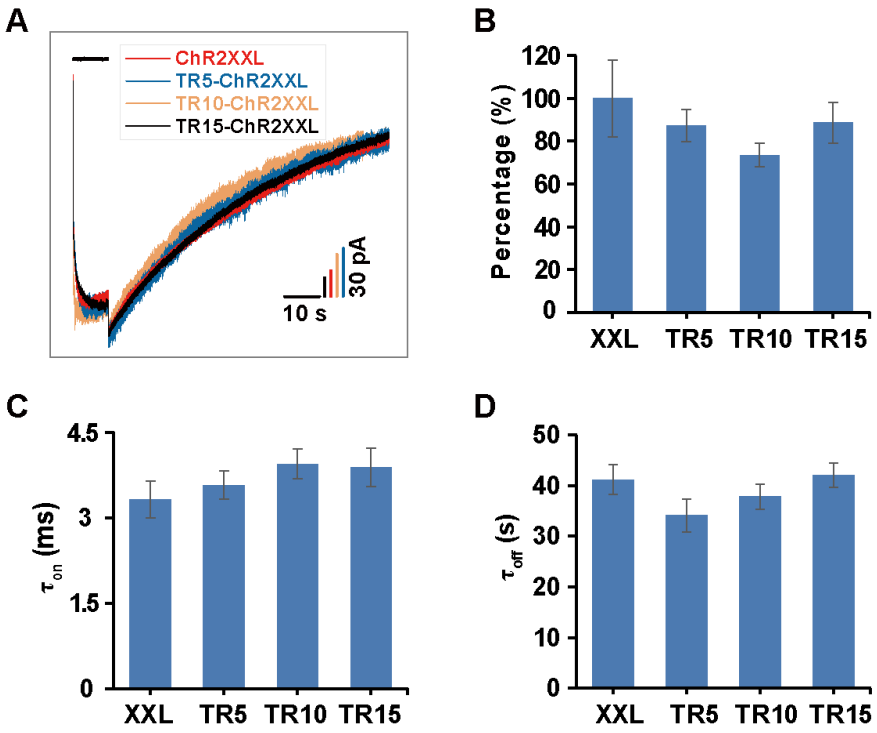

Figure 4.7 Electrophysiological characteristics of optogenetic actuators when expressed in HEK293 cells.

(**A**) Inward currents in voltage-clamped HEK293 cells evoked by 10 s of blue light (straight lines in black on the top). V_{hold} = -60 mV.

(**B**) The mean photocurrents generated by individual optogenetic tools in response to a 10 s blue light pulse were all normalized to the current evoked in the ChR2XXL group. N = 8, 12, 11, and 8. Data are presented as mean ± SEM. Kruskal-Wallis One-Way ANOVA test, $p > 0.05$.

(**C**) The average values for time constants of channel opening (τ_{on}). Data are presented as mean ± SEM. N = 11, 14, 17, and 11. One-Way ANOVA test, $p > 0.05$.

(**D**) The average values for time constants of channel closing (τ_{off}). Data are presented as mean ± SEM. N = 7, 10, 14, and 7. One-Way ANOVA test, $p > 0.05$.

4.2.6 Photocurrents in polarized cells

MDCK cells transfected with each of the constructs were grown on track etch membranes to promote polarization in the cell sheet. Patch clamp recordings in whole cell configuration voltage clamp at -60mV detected light induced currents in the cell illuminated with a small spot of laser light, so that one area of membrane the size of the laser spot should produce current. The produced pico amps per μm^2 of illuminated membrane for TR5-ChR2XXL, TR10-ChR2XXL, and TR15-ChR2XXL were 6.62 ± 2.59, 7.59 ± 1.99, and 4.97 ± 1.28 pA/μm^2 (mean ± SEM), respectively; higher than the current in ChR2XXL group (3.15 ± 2.60 pA/μm^2), although there was no significant difference between these groups. If cells produce equal numbers of proteins but the TR-ChR2XXL is concentrated in the lateral membrane, one spot of illumination may reach more channels. Furthermore, the TR-ChR2XXL currents produced in MDCK cells were generally larger than that in HEK293 cells, which were accordingly 0.95

± 0.12, 0.83 ± 0.17, and 0.64 ± 0.12 pA/μm^2. In each cell group, the currents were all normalized to the current produced in the ChR2XXL group, as shown in **Figure 4.8**. The currents of TR5-ChR2XXL or TR10-ChR2XXL in MDCK cells significantly differed from that of TR15-ChR2XXL in HEK293 cells, likely due to differences in protein density in the illuminated space, and different native ion flows in each cell type. Differences in MDCK current among the constructs is likely due to the number of channels expressed in the illuminated area since channel dynamics were shown to be consistent across constructs.

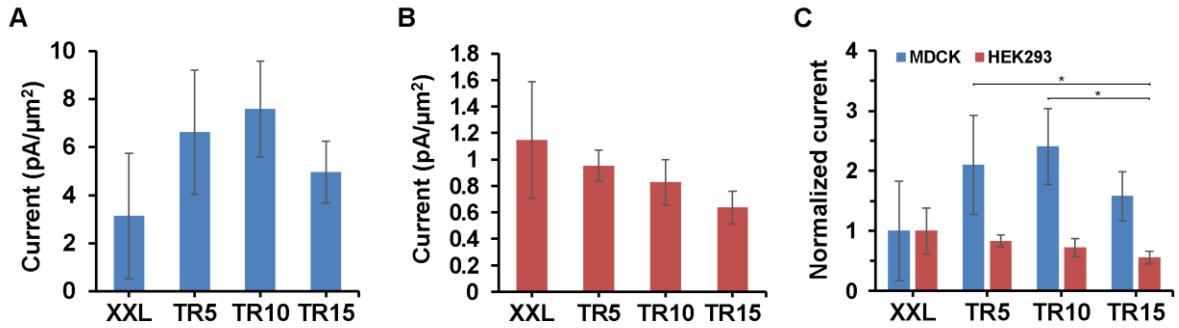

Figure 4.8 The currents produced in polarized and unpolarized cells.

(**A**) The currents of ChR2XXL, TR5-ChR2XXL, TR10-ChR2XXL, and TR15-ChR2XXL elicited by 50 ms light pulses in MDCK cells.

(**B**) The currents of ChR2XXL, TR5-ChR2XXL, TR10-ChR2XXL, and TR15-ChR2XXL evoked by 50 ms light pulses in HEK293 cells.

(**C**) The comparison of currents produced in MDCK and HEK293 cells. In each cell group, the currents were all normalized to the current of the ChR2XXL group. Data are presented as mean ± SEM. Kruskal-Wallis ANOVA test, TR5-ChR2XXL (MDCK) vs. TR15-ChR2XXL (HEK293), $^*p = 0.042 < 0.05$; TR10-ChR2XXL (MDCK) vs. TR15-ChR2XXL (HEK293), $^*p = 0.014 < 0.05$.

4.3 Subcellular localization in polarized cells

4.3.1 Subcellular localization in MDCK cells

The subcellular localization of TR-ChR2XXL in typical polarized MDCK cells was investigated first. The cell culture methods and related principles have been elucidated in Section 3.2.1, so they will not be repeated here. The monolayers of transfected MDCK cells expressing either ChR2XXL or TR-ChR2XXLs after growing for about 5 days were immunostained with Alexa Fluor 633 secondary antibody and primary antibody against podxl, an apical membrane protein [194, 195], to visualize the apical side of MDCK cells. DAPI was utilized to label nuclei, which facilitates the distinction of individual plasma membrane regions surrounding the nuclei.

The results are displayed in **Figure 4.9**. In each image, the top view and reconstructed orthogonal slices show the localization of TR-ChR2XXLs relative to the apical membrane. The orientations of image layers in the z-stack were all the same, and the top and bottom layers are

marked as T and B respectively in the first image of **Figure 4.9A**. The results showed that ChR2XXL localized to both the apical and basolateral sides of the MDCK cells (**Figure 4.9A**), while all TR-ChR2XXLs were surprisingly targeted to the lateral membranes (**Figure 4.9B-D**). These results were unexpected as the TR sequences were supposed to be apical targeting signals in epithelial cells as mentioned in Section 1.4.3.

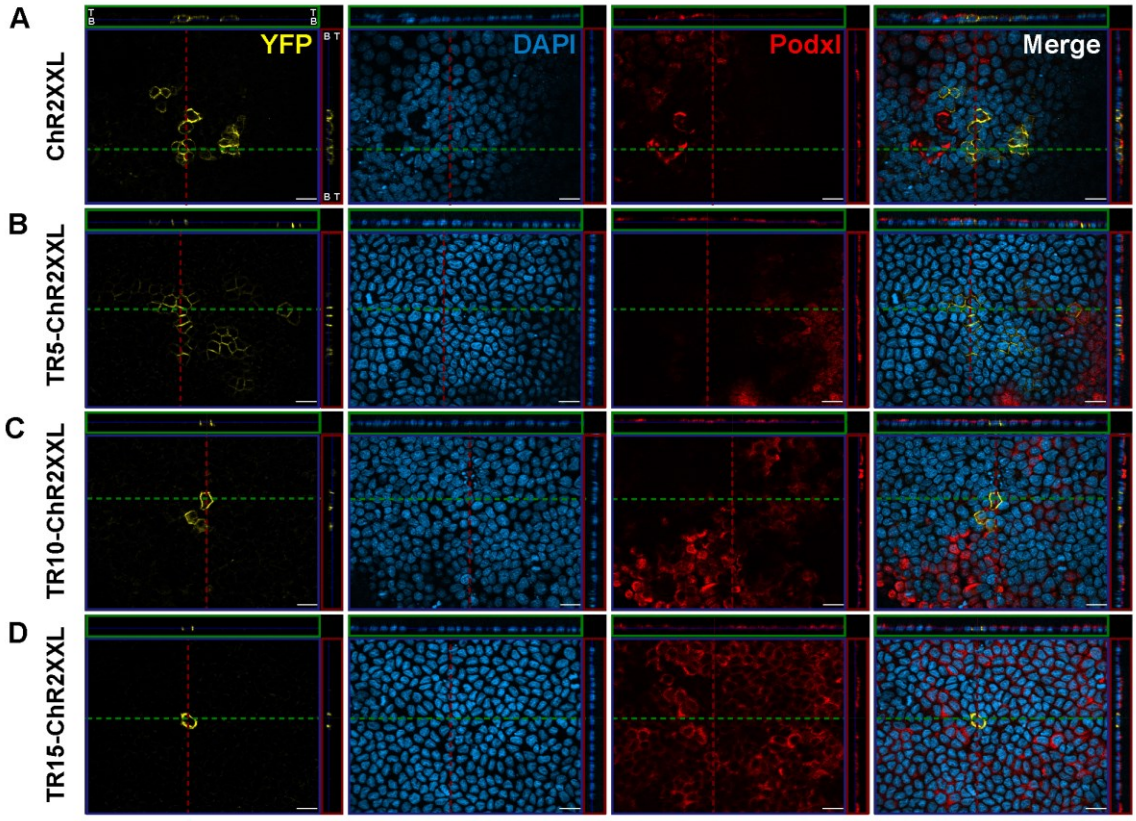

Figure 4.9 The subcellular localization of ChR2XXL (**A**), TR5-ChR2XXL (**B**), TR10-ChR2XXL (**C**), and TR15-ChR2XXL (**D**) when expressed in MDCK monolayers. Expressed channelrhodopsins were visualized by YFP (yellow). Cell nuclei were identified by DAPI staining (blue). The apical surface of MDCK cells was identified by antibody 3F2/D8 against Podxl (red). Merged images are shown in d. In each image, the top view of MDCK cells (at the focus level indicated by the blue line in small windows) is shown in the main window (XY plane), and vertical views of MDCK cells cut at green and red dashed lines are presented in the small green (XZ plane) and red windows (YZ plane), respectively. T, top layer; B, bottom layer. Scale bar, 20 μm.

4.3.2 Subcellular localization in neurons

To determine the subcellular localization of constructed TR-ChR2XXL in primary neurons, nucleofection and fluorescent immunostaining experiments were conducted successively. Dissociated cortical neurons were obtained from embryonic day 18 rat embryos and were cultured *in vitro*. Nucleofection was conducted before plating neurons on glass coverslips coated with PLL and ECM. Neurons grew *in vitro* for 5-7 days, then were immunostained. Antibodies against MAP2 and Tau1 were used to visualize the dendrites and axons, respectively.

Cell images were captured with fluorescent microscopy, and the typical images are shown in **Figure 4.10**. ChR2XXL localized to both dendrites (open arrowheads) and axon (filled arrowheads), while TR5-ChR2XXL and TR10-ChR2XXL mainly targeted to soma and dendrites (**Figure 4.10A**(a-c)). However, the expression of TR15-ChR2XXL produced negative effects on the growth of neurons, such that they could not extend axons and dendrites properly (**Figure 4.10A**(d), inside the dashed circle). Nontransfected neurons in the same culture had normal branched dendrites and well-extended axons, as shown in **Figure 4.10A**(d) (green arrowheads).

To quantitatively analyze the degree of polarized TR-ChR2XXL distribution in cortical neurons, two forms of axon-to-dendrite expression ratio, normalized (ADR) and unnormalized (uADR), were calculated (see Section 2.4). It is advantageous to evaluate the localization of a protein according to the ADR value, as ADR = 1 means the protein is nonspecifically localized, ADR < 1 means the protein is localized to dendrites, and ADR > 1 means the protein is localized to the axon. The value of uADR for ChR2XXL (0.67 ± 0.06, mean ± SEM) was about 3 times larger than that of TR5-ChR2XXL (0.20 ± 0.05) and TR10-ChR2XXL (0.19 ± 0.05) (**Figure 4.10B**(a)). The uADR of ChR2XXL was significantly different from that of either TR5-ChR2XXL or TR10-ChR2XXL. The ADR of TR5-ChR2XXL and TR10-ChR2XXL were 0.30 ± 0.08 and 0.28 ± 0.07, respectively, indicating both were localized to dendrites instead of axons in neurons (**Figure 4.10B**(b)), which were consistent with the statement that the basolateral signal mainly corresponds to the somatodendritic signal, considering the TR motif acted as a basolateral signal for ChR2XXL delivery in the present results. However, there were no such ADRs for TR15-ChR2XXL-positive neurons since these cells did not have extended neurites. These results showed that neurons transfected with TR5-ChR2XXL and TR10-ChR2XXL can grow normally through DIV5-7, and the expression mainly localized to the somatodendritic region, while neuron growth was affected by the expression of TR15-ChR2XXL, perhaps due to the longer projection from the neuron membrane surface by more tandem repeats that blocked neuronal adhesion to the substrates, thus influencing the neuron growth.

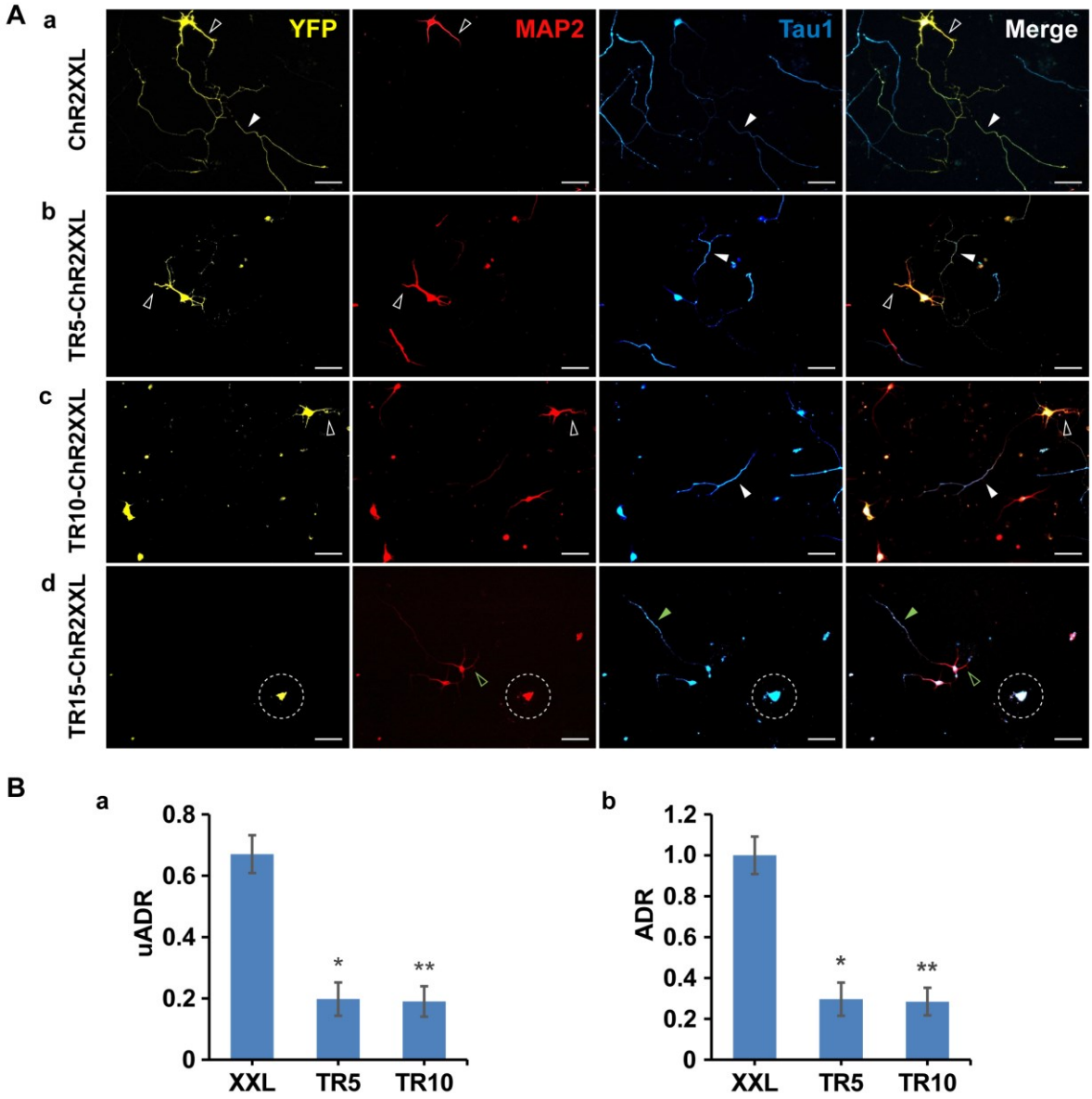

Figure 4.10 The subcellular localization of ChR2XXL, TR5-ChR2XXL, TR10-ChR2XXL, and TR15-ChR2XXL when expressed in neurons.

(**A**) Immunostaining of cortical neurons transfected with ChR2XXL (a), TR5-ChR2XXL (b), TR10-ChR2XXL (c), and TR15-ChR2XXL (d) (DIV5-7). Dendrites were labeled with anti-MAP2 (red) and axons with anti-Tau1 (blue). Filled arrowheads point to the axon; open arrowheads point to the dendrite. White arrowheads mark transfected neurons; in (d) green arrowheads mark nontransfected neurons, and the dashed circle indicates TR15-ChR2XXL-positive neuron. Scale bar, 50 μm.

(**B**) The unnormalized and normalized axon-to-dendrite expression ratio (uADR (a) and ADR (b)). Data are presented as mean ± SEM. N = 6 for each group. Kruskal-Wallis ANOVA test, $^{*}p < 0.05$, $^{**}p < 0.01$, against the value in ChR2XXL group.

4.4 Expression in different cell types

4.4.1 Expression in HEK293 cells

In order to investigate the applicability of these actuators, expression in HEK293 cells was evaluated first. After chemical transfection, HEK293 cells displayed classically pyramidal or rhombic morphology, unaffected by the expression of these actuators (**Figure 4.11**). The transfection efficiencies of TR5-ChR2XXL, TR10-ChR2XXL, and TR15-ChR2XXL in HEK293 cells on DPT2 (2 days post transfection) were 7.95% (12 out of 151 cells), 6.39% (17 out of 266 cells), and 6.88% (11 out of 160 cells), respectively, comparable to ChR2XXL (7.23%, 6 out of 83 cells) (see Table in **Figure 4.14A**). So the influence of various TR numbers on the expression of channelrhodopsin in HEK293 cells was slight (see **Figure 4.14B**).

4.4.2 Expression in MDCK cells

Then the transfection efficiencies of these actuators in MDCK cells were checked. In this part, the purpose was to evaluate the number of expressing cells, so MDCK cells did not need to be plated on membrane filters, instead they were plated at low density on tissue culture plastic well plates mainly for easy operation and observation. The transfected MDCK cells on DPT5 are shown in **Figure 4.12**. Generally, after growing for a certain time on a solid support, MDCK cells form cell islands. Cells in the center usually differentiate more than those at the edges, which remain migratory capability with lamellipodia-like structures [193]. The TR-ChR2XXLs expression did not alter the normal morphology of MDCK cells (**Figure 4.12**). The transfection efficiency of ChR2XXL was 2.65% (3 out of 113 cells), while the efficiency of TR5-ChR2XXL was a little higher (3.14%, 5 out of 159 cells) than this. Whereas the efficiencies of TR10-ChR2XXL and TR15-ChR2XXL were much lower than ChR2XXL, at 1.79% (2 out of 112 cells) and 0.78% (1 out of 128 cells), respectively (see Table in **Figure 4.14A**). Therefore, the channelrhodopsin with 5TR had enhanced transfection efficiency in MDCK cells, while 10TR and 15TR decreased the expression, though only significantly for TR15 (see **Figure 4.14B**).

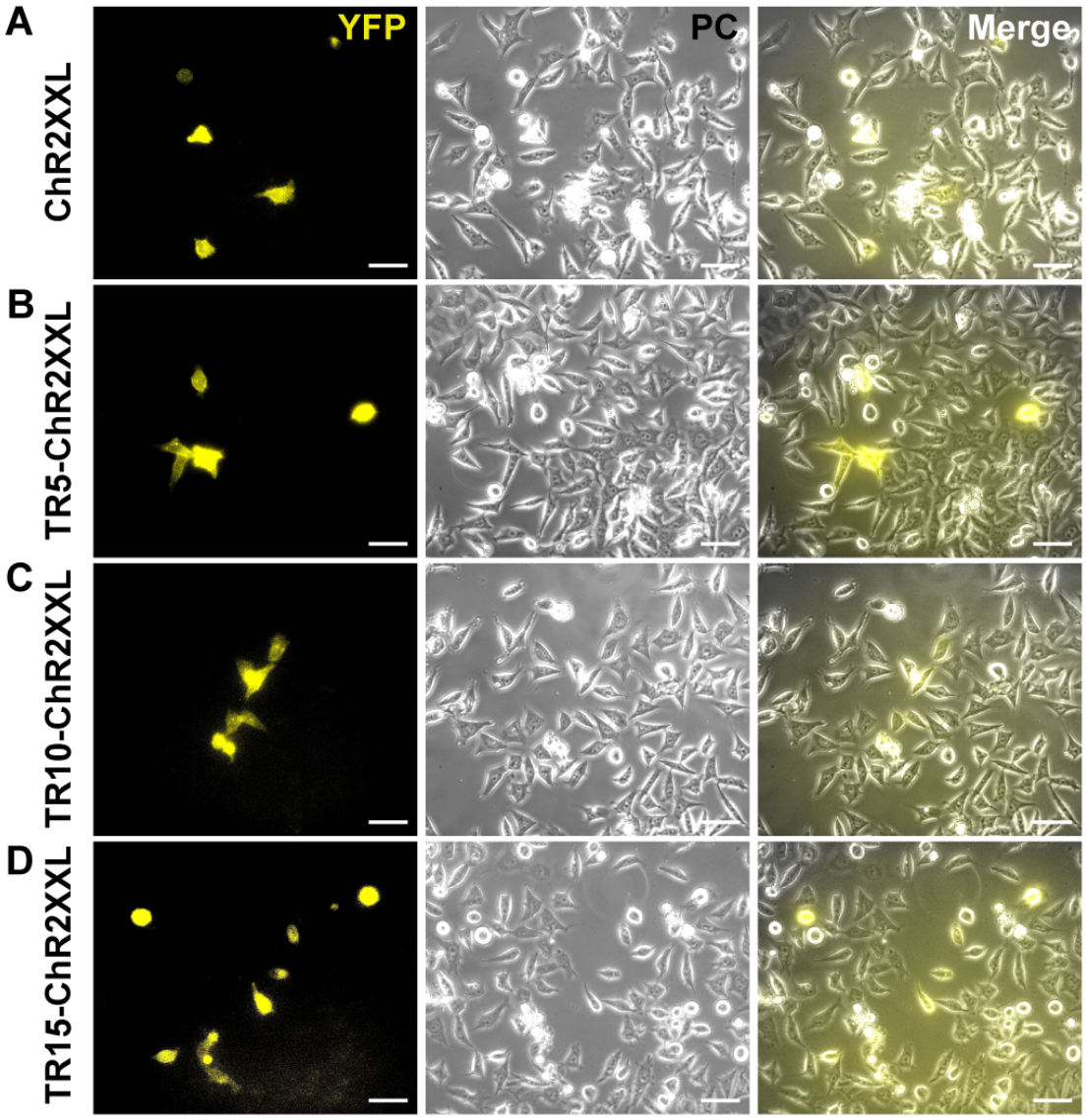

Figure 4.11 The expression of ChR2XXL (**A**), TR5-ChR2XXL (**B**), TR10-ChR2XXL (**C**), and TR15-ChR2XXL (**D**) in HEK293 cells on DPT2. Left column, fluorescent images; middle column, phase contrast (PC) images; right column, merged images. Scale bar, 50 μm.

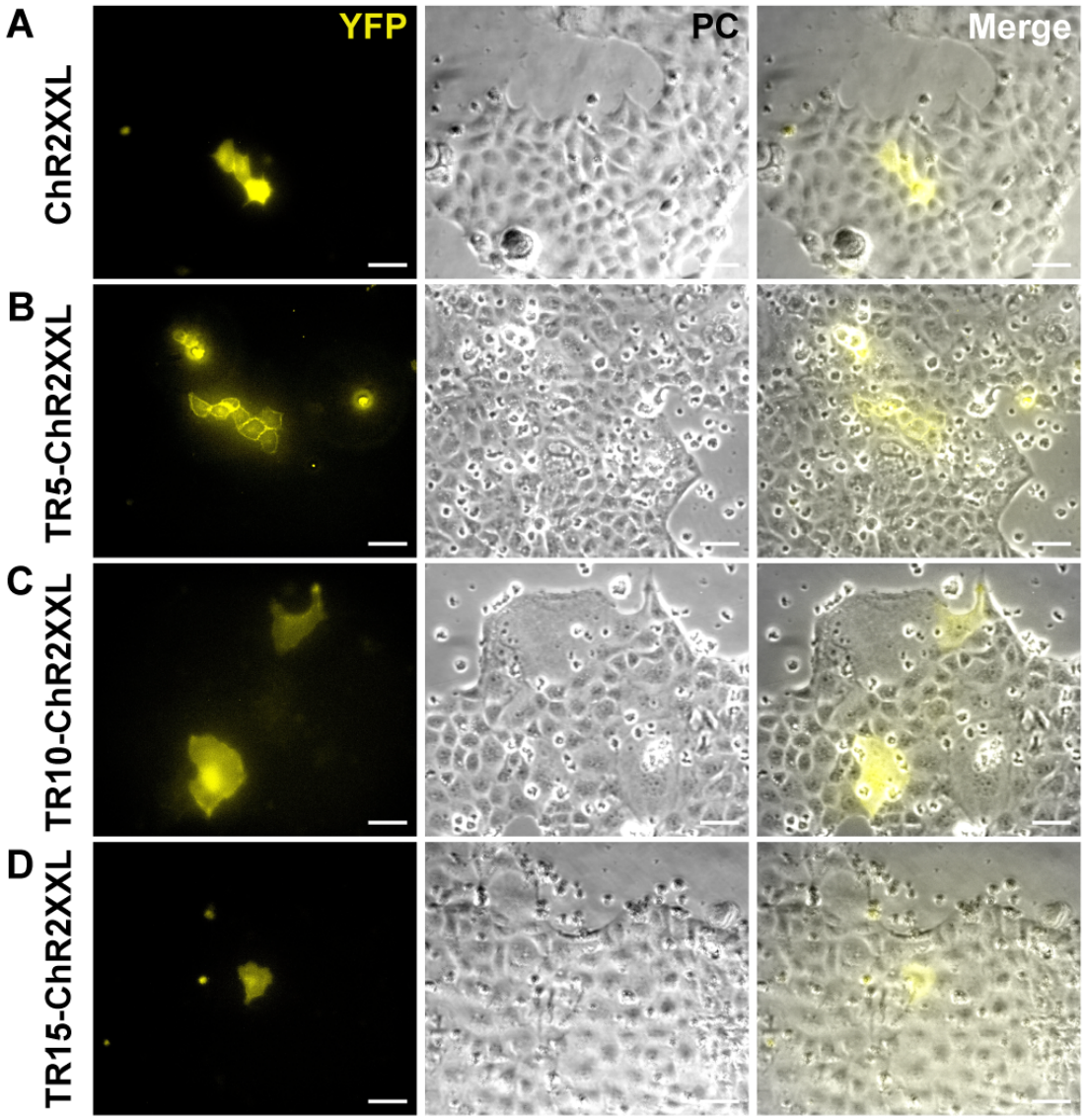

Figure 4.12 The expression of ChR2XXL (**A**), TR5-ChR2XXL (**B**), TR10-ChR2XXL (**C**), and TR15-ChR2XXL (**D**) in MDCK cells on DPT5. Left column, fluorescent images; middle column, phase contrast (PC) images; right column, merged images. Scale bar, 50 μm.

4.4.3 Expression in neurons

As neurons transfected with constructed optogenetic actuators grew *in vitro*, some unexpected changes were observed. *In vitro*, neurons undergo five stages of development characterized according to their morphological changes [203, 204], as mentioned in Section 1.1.1.3. In short, first, neurons form several filopodia shortly after being plated. Second, a few filopodia grow into immature neurites. Third, one neurite extends rapidly, becoming the axon. Fourth, the other neurites elongate and become dendrites. Finally, the axon and dendrites are mature, and synaptic contacts are established, forming a complex neural network. For neurons expressing ChR2XXL, the morphologies from axon formation to maturity were unaffected by the transgene, as shown in the picture (a) of **Figure 4.13A** (DIV4) and **Figure 4.13B** (DIV14),

compared to the nontransfected neurons. **Figure 4.13A** (b) and (c) show the neurons transfected with TR5-ChR2XXL or TR10-ChR2XXL on DIV4, displaying normal morphologies, as well as initial non-homogeneous expression of the channels. However, the neurites of these transfected neurons started shrinking and degenerating roughly on DIV7 to DIV10, at which time the neurons would enter the fifth stage of development. **Figure 4.13B** (b) and (c) show that by DIV14, the expressing neuron showed a deformed soma shape, detached from the substrate and displayed degradation, and the nucleus became no longer visible as a lower fluorescence region, nor in phase contrast images. In the case of neurons transfected with TR15-ChR2XXL, there were rare neurons that could express it, all of which had abnormal morphologies and could not project out neurites properly at any age. **Figure 4.13A** (d) displays a neuron on DIV4 with the best morphology that could be found. The expression of TR15-ChR2XXL was quite low, and even in this case the neuron seemed less healthy than others. Hence, neurons expressing TR5-ChR2XXL or TR10-ChR2XXL can not survive through the fifth stage, while TR15-ChR2XXL-positive neurons were abnormal even at earlier stages (see Section 5.2.2 for discussion).

For quantitative analyses, the transfection efficiencies of these proteins in neurons on DIV7 were evaluated (**Figure 4.14A**). In one typical count, the transfection efficiencies of TR5-ChR2XXL and TR10-ChR2XXL were 9.68% and 3.33%, respectively. However, in the TR15-ChR2XXL group, neurons could hardly express this protein, and the efficiency was only 0.78%, much lower than that of the ChR2XXL group (24.69%). Therefore, the presence of the mucin repeats reduced the number of expressing neurons, and with more tandem repeats at the N-terminus of ChR2XXL, the effects were more obvious (see also Section 4.4.4).

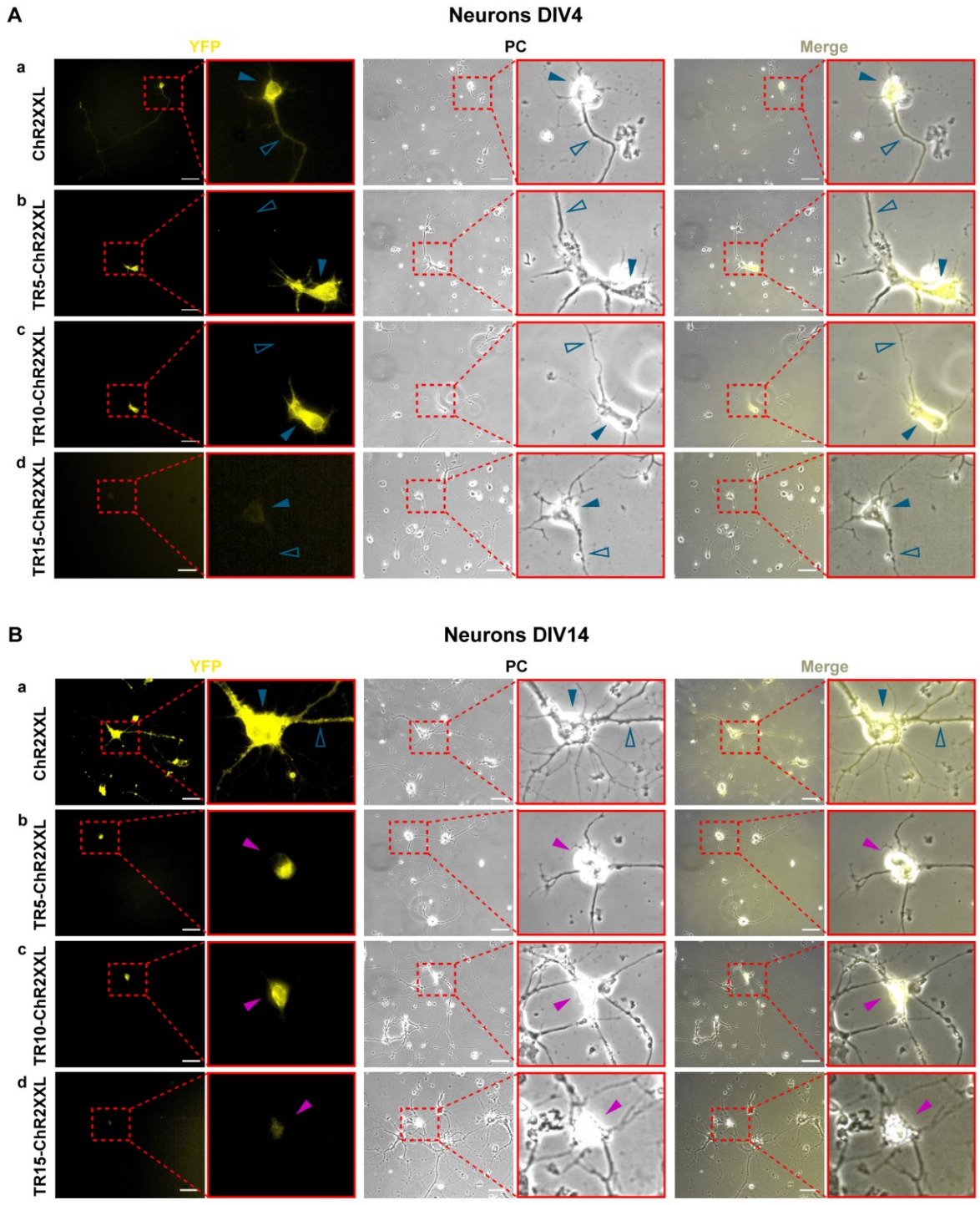

Figure 4.13 Morphological changes of neurons expressing different optogenetic actuators during culture. Neurons expressing ChR2XXL (a), TR5-ChR2XXL (b), TR10-ChR2XXL (c), and TR15-ChR2XXL (d) on DIV4 (A) and DIV14 (B) are displayed. Blue arrowheads point to live expressing neurons (solid arrowhead, soma; open arrowhead, neurite), and magenta arrowheads point to dead formerly expressing neurons. Left column, fluorescent images; middle column, phase contrast (PC) images; right column, merged images. Scale bar, 50 µm.

4.4.4 Comparison of transfection efficiency

To test broader applicability, transfection efficiencies in two more independent cultures were assessed. **Figure 4.14A** shows the typical transfection efficiencies of these proteins in HEK293 cells, MDCK cells, and neurons. The results are summarized in **Figure 4.14B**. Specifically, the individual transfection efficiency was normalized to that of ChR2XXL for each cell type. In neurons, the normalized transfection efficiencies of TR5-ChR2XXL, TR10-ChR2XXL, and TR15-ChR2XXL were 0.34 ± 0.005, 0.11 ± 0.011, and 0.03 ± 0.001 (mean ± SEM), respectively. With more TRs, the transfection efficiency decreased. There was a significant difference between the ChR2XXL group and the TR15-ChR2XXL group. In MDCK cells, the trend was similar, with 1.12 ± 0.046, 0.62 ± 0.102, and 0.24 ± 0.014, which were much higher than in neurons, in particular for TR5-ChR2XXL's transfection efficiency that was even higher than ChR2XXL. There was a significant difference between the TR5-ChR2XXL group and TR15-ChR2XXL group, indicating that the targeting sequence itself in MDCK cells did not reduce TE, but the number of TRs did. However, the transfection efficiencies in HEK293 cells were all near one (1.08 ± 0.107, 0.91 ± 0.050, and 0.97 ± 0.081), and not significantly different from each other. Therefore, the tandem repeats' effects were less obvious in HEK293 cells than in the two polarized cell types, where the channelrhodopsin with more TRs had lower transfection efficiencies. Though both polarized cell types showed a decreasing trend with the specific number of TR, the absolute TE in MDCK cells remained higher. For future implementation, it must be considered how to achieve high expression rates relative to the cell specific TE, for example by enriching initially transfected cells in dividing cell cultures or exploring different plasmid transfection methods.

A

Transfection efficiency (TE)

		ChR2XXL	TR5-ChR2XXL	TR10-ChR2XXL	TR15-ChR2XXL
HEK293	Expressing cells	6	12	17	11
	Total cells	83	151	266	160
	TE (%)	7.23	7.95	6.39	6.88
MDCK	Expressing cells	3	5	2	1
	Total cells	113	159	112	128
	TE (%)	2.65	3.14	1.79	0.78
neuron	Expressing cells	20	9	3	1
	Total cells	81	93	90	129
	TE (%)	24.69	9.68	3.33	0.78

B

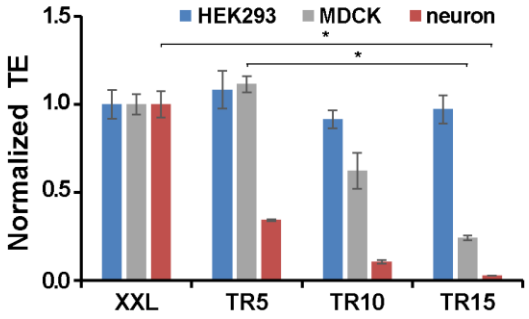

Figure 4.14 The transfection efficiencies of ChR2XXL, TR5-ChR2XXL, TR10-ChR2XXL, and TR15-ChR2XXL in HEK293 cells, MDCK cells, and neurons.

(**A**) The transfection efficiencies of ChR2XXL, TR5-ChR2XXL, TR10-ChR2XXL, and TR15-ChR2XXL in HEK293 cells (DPT2), MDCK cells (DPT5), and neurons (DIV7) in a typical independent culture.

(**B**) The comparison of normalized transfection efficiencies in HEK293 cells, MDCK cells, and neurons. In the same cell type, the individual transfection efficiency was normalized to that of ChR2XXL. Data are presented as mean ± SEM. Three independent cultures for each group. Kruskal-Wallis ANOVA test, MDCK cells, TR5-ChR2XXL vs. TR15-ChR2XXL, $^{*}p < 0.05$; neurons, ChR2XXL vs. TR15-ChR2XXL, $^{*}p < 0.05$.

5 Discussion

This chapter aims to discuss and expand the relevant outcomes in the present work. **Section 5.1** focuses on the discussion on the first part of this work where a cytoplasmic tail of rhodopsin was fused to the C-terminus of ChR2opt followed by a series of investigations. **Section 5.2** presents the discussion on the second part of this work where different numbers of tandem repeats from the extracellular domain of mucin were added to the N-terminus of ChR2XXL and subsequent studies about the built constructs were conducted. At the end of each section, a summary is given.

5.1 Optogenetic actuator I

5.1.1 Subcellular localization of ChR2opt-mKATE-AT in polarized cells

In polarized cells, the sorting mechanisms of subcellular membrane proteins are conserved. It is suggested that both somatodendritic and basolateral sorting signals are frequently located at the cytoplastic tails of transmembrane proteins, while axonal and apical sorting signals are usually at the extracellular or transmembrane domains of proteins [139, 153-157]. In this work, the subcellular localization of new constructed ChR2opt-mKATE-AT was estimated in both polarized MDCK cells and neurons (**Section 3.2**). First, the targeting sequence from the cytoplasmic tail of rhodopsin delivered ChR2opt-mKATE to the apical membrane side in MDCK cells (Figure 3.2). It was expected since this sequence was supposed to be an apical targeting motif, and previous reports demonstrated the cytoplasmic tail can target both basolateral membrane protein CD7 and cytosolic protein glutathione S-transferase to the apical surface of MDCK cells [171], although the cytoplasmic domain of proteins are usually related to basolateral targeting and the apical targeting motifs are usually found in the lumenal domain. In addition, the AT targeting motif transported ChR2opt-mKATE to the somatodendritic region in neurons (Figure 3.3), which indicated that the cytoplastic apical signal corresponds to the somatodendritic signal in this case. Considering it is usually reported that the apical signal from an extracellular region mainly corresponds to the axon signal, perhaps the location where the signal comes from is important.

5.1.2 Electrophysiological characterization of ChR2opt-mKATE-AT

After the successful construction of ChR2opt-mKATE-AT by using genetic engineering, its possible influences on the electrophysiological properties of the membrane were investigated (**Section 3.3**), as the expression of foreign channelrhodopsins may bring unexpected problems to cells. The basic properties including the resting membrane potential, input resistance, and membrane capacitance were evaluated, and the results showed that the group with targeted actuators did not differ from the untargeted and control groups (Figure 3.4A-C). Also, the

assessment of neuronal excitability by injecting various amounts of currents in the dark indicated the same result (Figure 3.4D). These results reflected the expression of ChR2opt-mKATE-AT did not produce evident effects on the native compositions of the membrane, like the number and location of voltage-gated sodium and potassium channels; changes in which would show a detectable influence on the electrophysiological function of the membrane. Besides, the ChR2opt-mKATE-AT-positive neurons had normal morphology and could live as long as the nontransfected neurons did, indicating the expression of ChR2opt-mKATE-AT did not have obvious impacts on neurons overall.

The total photocurrents produced in an optogenetic stimulation are determined by the area of the membrane illuminated, channel density, number of received photons, quantum efficiency, and the conductance of a single channel under a certain membrane voltage. First, the large illuminated membrane area usually covers more channelrhodopsins but would decrease the stimulation specificity. Precise spatial stimulation is especially important for subcellular manipulation. The laser spot size used in this work was 12 μm in diameter, namely a 113 μm^2 illumination area, which is smaller than the laser spot used by most other labs that can cover the whole cell body. In those cases, all channels are inside the spot and have the same state at a given time point. But in my case, the channels inside and outside the spot have different stimulation histories, so upon continuous light illumination the channels could diffuse from dark outside the spot into the spot. The local channel density in small spot size illumination is relatively more important than in whole cell illumination. The channel density affects the number of open channels upon illumination, and it depends on the expression level of the channelrhodopsins in the illuminated area. To try to ensure that the total number of channels in a cell is the same, the same number of plasmids was transfected into a certain number of cells. Besides, the total number of received photons is determined by the number of photons per unit time and the illumination time, which are the light power intensity and the pulse duration, respectively. Additionally, the quantum efficiency is the effectiveness of an absorbed photon to successfully convert the channel from a closed state into an open state. It is an intrinsic property of the chromophore retinal, and it is unaffected by other external factors and hard to be further optimized. But the state the channel starts being illuminated from affects the result. Finally, the conductance of a single channel relies on the ion permeation of the channelrhodopsin at a specific condition. The conductance of a channelrhodopsin is constant when facing specific intracellular and extracellular solutions at a given potential. Taken together, precise and effective optogenetic manipulations depend on the careful optimization of various conditions. In addition to some factors already discussed above, several other controlled experimental parameters including light pulse duration, light power intensity, and stimulus frequency were emphatically investigated in this work (**Section 3.4**) and are discussed below.

First, the ChR2opt-mKATE-AT could react precisely and efficiently in response to light stimulations of various pulse durations ranging from submillisecond to second timescales (Figure 3.5 and Figure 3.6). For ChR2opt-mKATE-AT, the required pulse time was about 0.5 ms in the studied case in a neuron. Within the time shorter than the pulse time required, the

channels could not fully open, and there were not sufficient ions passing through the channels, thereby just producing small and slow spikes or even no spike. In the present result, a pulse time short to 0.1 ms could induce high-fidelity action potentials although with a little slower depolarization rate than that with a longer pulse time. In certain cases, even a 0.01 ms pulse time could elicit action potentials but with much smaller amplitudes and much slower kinetics (Figure 3.5). However, in the same condition it usually required about 5 ms pulse time for ChR2opt-mKATE to generate high-reliability APs, and a shorter than 1 ms pulse time was unlikely to elicit APs. With a 1 ms light pulse wild-type ChR2 also hardly drives spiking reliably [118]. This reflected that with a fixed light stimulation spot size at the soma, light stimulation in neurons expressing ChR2opt-mKATE-AT could produce larger photocurrents than in neurons expressing ChR2opt-mKATE. The experimental data presented in Section 3.5 also directly supported this conclusion, and a detailed explanation will be given in Section 5.1.3. In the experiments with a series of relatively long light pulses, the results showed that the time constant of channel closure did not depend on the pulse time in the range studied. Also, it indicated that the produced photocurrents displayed light adaptation over time (Figure 3.6).

In the investigation of the light power intensity, it was found that the slope of membrane depolarization was positively correlated with the light output power. The power stated in this work is the power of the laser beam. In the range of 0.015 mW to 3 mW light output power, the larger the power, the faster the membrane depolarized, and correspondingly, the shorter the time-to-threshold and time-to-peak (Figure 3.7). With a higher light power intensity, more photons would simultaneously hit the retinal chromophore bound with channelrhodopsins, so the channels were more likely to be activated and more photocurrents were produced. In addition, the signal traces behaved with higher fidelity upon repetitive stimulations at high light power intensity compared with that at lower light power intensity, as the voltage traces at higher light power intensity behaved more uniformly and were with lower standard deviations.

The study of stimulus frequency showed that in regular-spiking neurons the stimulation with 10 ms pulse time in less than 20 Hz frequency can induce action potentials with high reliability, whereas in faster than 30 Hz frequency can not, and membrane potentials were blocked at a depolarization state (Figure 3.8). This meant the stimulus frequency faster than 30 Hz decreased the fidelity of generating action potentials. This was because continuous light stimulation resulted in a constant proportion of light-activated channels being open and that blocked the potential in a depolarization state, inactivating voltage-gated sodium channels in regular-spiking neurons during the stimulation period. Also, after light-off the potential was unable to repolarize completely within the short interpulse time under high stimulus frequency, leading to failure to generate further action potentials. But in fast-spiking and burst-spiking neurons, because of the different types and conductance densities of ion channels in the membrane [205, 206], the spikes caused by light-activated channels can repolarize rapidly after each depolarization, so the continuous action potentials could be triggered (Figure A.3). Overall, the optogenetic manipulation with ChR2opt-mKATE-AT is effective in multiple firing

patterns of neurons, but high-frequency stimulation is not feasible for neurons whose membrane potentials are easily blocked by depolarization.

5.1.3 The spatial specificity gained by using ChR2opt-mKATE-AT

The properties of ChR2opt-mKATE-AT and ChR2opt-mKATE in response to light illumination with a fixed spot size at the cell body were compared in both neurons and HEK293 cells (**Section 3.5**). The results in neurons indicated that the amplitudes of produced peak and steady photocurrents of ChR2opt-mKATE-AT were larger than that of ChR2opt-mKATE (Figure 3.9). However, in HEK293 cells the induced photocurrents of these two constructs were comparable (Figure 3.10). Considering that the photocurrents were determined by the number of open channels and the conductance of a single channel at a given potential, and the later parameter of ChR2opt-mKATE-AT should be the same as ChR2opt-mKATE since the structural parts that are directly related to the ion permeation were not modified, the different results in neurons arose from the difference of the number of open channels. So there were more ChR2opt-mKATE-AT localized at soma compared with ChR2opt-mKATE. The similar signals produced in HEK293 cells showed that the amounts of these two constructs in the illuminated area were equal. In addition, a little faster time constant of channel opening of ChR2opt-mKATE-AT in neurons meant that more channels were activated simultaneously, suggesting more channels existed at soma as well.

The ChR2opt-mKATE can be used to map neuronal circuits in complex neural networks. An example is given in Figure A.6. By comparing the response time and the strength of received signals, a small microcircuit can be established. In this case, the stimulation at position 2 can trigger a signal at the soma of the recorded neuron 1. But it is uncertain whether the signal is from the soma of neuron 2 or the neurites of neuron 1. Hence, the universal distribution of actuators is not sufficient for precisely mapping all microcircuits, and the spatial specificity needs to be improved. The spatial specificity of using ChR2opt-mKATE-AT was estimated by stimulations at the soma and positions along the axon (**Section 3.6**). The induced photocurrents of ChR2opt-mKATE-AT upon light stimulations at the axon were all significantly lower than that at the soma, whereas in the case with ChR2opt-mKATE the photocurrents elicited by stimulations at the axon displayed a gradual and slight decreasing trend compared with that at the soma (Figure 3.11). This suggested fewer ChR2opt-mKATE-AT than ChR2opt-mKATE were located at the axon, given that the amplitudes of evoked photocurrents correlated positively with the amounts of the expressed channelrhodopsins. Besides, the recorded signals in the form of voltage also showed the same results (Figure 3.12). These results indicated that it was less likely to activate a neuron expressing ChR2opt-mKATE-AT by illuminating its axon, thereby the higher spatial specificity can be achieved by using ChR2opt-mKATE-AT in neurons. In the mentioned case above, if using the actuator ChR2opt-mKATE-AT, the possibility that the induced signal was from the axon of neuron 1 was low as the expression of ChR2opt-mKATE-AT was excluded from the axon.

5.1.4 The retrograde trafficking of ChR2opt-mKATE-AT

Elucidating the underlying mechanism of subcellular localization of ChR2opt-mKATE-AT in neurons will benefit us to construct more useful constructs for subcellular applications. In the observation of protein trafficking (**Section 3.7**), it was found that during the whole observation period, protein ChR2opt-mKATE can stably present at both somatodendrites and axons, whereas protein ChR2opt-mKATE-AT can only stably present at sometodendrites and the ones located at the axon would be transported back to soma quickly (Figure 3.13). It is speculated that this polarized protein trafficking may be related to the function of dyneins. The dynein, a microtubule motor, moves towards the minus-end of microtubules, and a light chain Tctex-1 is located at its tail domain [207]. In rod photoreceptors, rhodopsin is synthesized in the inner segment, then vectorially transported into the outer segment. During this process, the cytoplasmic tail acts as a targeting motif that binds to the dynein light chain Tctex-1. The last five amino acids QVAPA of the cytoplasmic sequence play a critical role in their recognition [168]. The dynein translocates rhodopsin-bearing vesicles along microtubules whose minus-ends point to the basal bodies that are located at a connecting region between the inner segment and the outer segment [208, 209]. Similarly, in MDCK cells, the polarized distribution of rhodopsin is also reported to be regulated by the interaction of rhodopsin's cytoplasmic tail and the dynein light chain Tctex-1 [210, 211]. As the minus-ends of microtubules point to the apical surface of MDCK cells [212], it makes sense that dynein carries the rhodopsin towards the apical membrane side. At the axon of neurons, microtubules have a uniform plus-end out orientation, that is, the minus-ends of the microtubules point to soma [213]. Therefore, perhaps it is also dynein that transports the ChR2opt-mKATE-AT back to soma. But this still needs to be investigated further.

5.1.5 The genetic and optical targeting strategies

In this work, the genetic targeting strategy was adopted to achieve optogenetic control at subcellular resolution. The goal can also be realized by using an optical targeting strategy, two-photon activation. Conventional illumination methods will activate the channelrhodopsins all along the light pathway, including those above and below the focal plane of interest, whereas the two-photon illumination can only activate the channelrhodopsins in the focal plane, enabling better spatial specificity [96]. Besides, two-photon illumination can provide deeper penetration in scattering tissue, as it utilizes a near-infrared laser that tissue absorbs less and scatters less. However, some considerations should be taken into account. First, the single channel conductance of ChR2 is relatively low (50-250 fS), so the generation of substantial neuronal depolarization requires large numbers of channelrhodopsins to open simultaneously. But the volume that two-photon excitation could illuminate is quite small (~2-5 μm^3), so only a small number of channels could be activated at once [214]. As a result, the depolarization induced by two-photon excitation of ChR2 may be not sufficient to trigger action potentials in neurons. This limitation is overcome currently by extending the illumination area, primarily by either scanning or parallel illumination [215, 216]. Nevertheless, this will compromise the

temporal or spatial resolution. The actuators with slow off-kinetics like C1V1 (τ_{off} = ~120 ms) are preferable for this application [217], as the slow closure of the channel allows more ions to flow through the ion permeation pore, thereby producing larger photocurrents. In addition, the two-photon excitation setups are expensive, so it is not suitable for the reality of using a tool beyond scientific performance. Compared with the optical targeting strategy, the subcellularly-localized optogenetic actuators realized by adopting the genetic targeting strategy face fewer these problems. The constructed ChR2opt-mKATE-AT in this work can ensure substantial membrane depolarization performance while having higher spatial specificity.

5.1.6 Summary

In this part, an apical targeting (AT) motif from rhodopsin was fused to the C-terminus of ChR2opt, an optimized version of Channelrhodopsin-2 variant ChR2(H134R), by using seamless cloning. First, the investigation of the subcellular localization in polarized cells by using fluorescent immunostaining showed that the AT motif delivered ChR2opt-mKATE to the apical membrane side in MDCK cells, whereas it primarily targeted to the somatodendritic compartment in neurons. Then, the measurements of intrinsic electrophysiological properties, such as the resting membrane potential, input resistance, and membrane capacitance, suggested that the expression of ChR2opt-mKATE-AT had not produced obvious negative effects on neurons. Even a low power intensity of light stimulation in a short pulse time can induce high-fidelity action potentials (Figure A.7). Also, ChR2opt-mKATE-AT can be used in multiple firing patterns of neurons, but for neurons whose membrane potentials are easily blocked by depolarization, the high-frequency stimulation is not feasible. Besides, assuming the total amount of channelrhodopsins expressed in a neuron is constant, more channelrhodopsins would localize at somatodendrites of a neuron expressing ChR2opt-mKATE-AT than that expressing ChR2opt-mKATE, as a result of the targeting effect of AT motif. Therefore, light stimulation with a fixed spot size at the soma would evoke a stronger electrical signal in a neuron expressing ChR2opt-mKATE-AT than that expressing ChR2opt-mKATE. Furthermore, the obviously decreased light-induced signals at the axon of the neurons expressing ChR2opt-mKATE-AT confirmed that the spatial specificity of optogenetic manipulations by using this actuator can be enhanced. Additionally, the retrograde trafficking of ChR2opt-mKATE-AT from axon to cell body observed at the axon was proposed to be related to the function of dyneins. Taken together, a subcellular targeted optogenetic actuator was constructed and it could be used to probe neuronal functions with increased spatial resolution. For instance, one could localize the channelrhodopsin to dendrites while avoiding the expression in axons so that when exciting the dendrites with light the closely packed neighboring axons are not activated, which could be applied to map neural circuits in a dense neural network.

5.2 Optogenetic actuator II

5.2.1 Electrophysiological characterization of TR-ChR2XXL

5.2.1.1 The depolarization properties of TR-ChR2XXL

The three new optogenetic actuators TR-ChR2XXLs created in this work behaved similarly to ChR2XXL in terms of electrophysiological functions (Figure 4.2-4.4 and Figure 4.7, **Section 4.2**). They all had slow off-kinetics and extended open state lifetime, resulting in high light-evoked currents. During rapid illumination, photocurrents induced a long-lasting depolarization block of the membrane (Figure 4.3 and Figure 4.4) due to insufficient repolarization resulting from the slow closing rate of ChR2XXL. In response to repetitive stimulations, the photocurrents decayed a little from one stimulation to the next. Comparatively, photocurrents at a long pulse time and a short recovery time decayed a little more than that at a shorter pulse time and a longer recovery time (Figure 4.3C and Figure 4.4E). Nevertheless, this did not influence their continuous depolarization effect. With these high long currents, TR-ChR2XXLs are suitable for subcellularly precise optogenetic manipulation avoiding off-target effects, especially when light delivery is limiting or long-lasting depolarization without continuous illumination is needed, for instance, in behavioral research. This also suggested that the N-terminal of channelrhodopsins can be utilized for protein modifications, even if the new group added substantial bulk to the molecule, which opens a way to the novel expansion of the optogenetic toolbox.

5.2.1.2 The extra transient current peak

In this work, all channelrhodopsins showed an additional small transient current peak upon light-off in voltage clamp mode (Figure 4.3-4.7, **Section 4.2**), which meant a larger number of open channels were accumulated transiently. This observation is related to the photocycle of ChR2XXL, which is a complex process and is still under debate. The photocycle involves several intermediates (D470 $\xrightarrow{①}$ P500 $\xrightarrow{②}$ P390 $\overset{③}{\longleftrightarrow}$ P520 $\xrightarrow{④}$ P480 $\xrightarrow{⑤}$ D470) with different conduction abilities and kinetics (see Section 1.3.1.2). There are two possible explanations for the transient peak at light-off. The first is that the small increased current arises from the photoactivation of intermediate P480 [134, 218, 219]. P480 itself is shown to be photoactive, and it forms at a late state in the photocycle (transition 4, above), probably during channel closure [220]. Another explanation is considered from the aspect of the equilibrium modulator. The elicited currents at light-on result from the accumulation of the conducting intermediate P520, which is in equilibrium with earlier nonconducting intermediate P390 (transition 3, above). When light is off, the intermediate P520 is unable to convert into the later nonconducting P470 instantaneously, but there are still some earlier P390 that continue using already absorbed photons to photoconvert to P520 (transition 3 continues to fill state P520, while transition 5 is slower) [133]. In a word, an additional transient current appears in the photocurrent of ChR2(D156C) in response to light off. In addition, this transient current has also been observed in ChR2(C128S) by Berndt et al. [133] and in ChR2(D156A) by Bamann et al. [134] and Perny et al. [136]. These observations all occur in the mutants within the

hydrogen bonded DC pair. Overall, our work and these works together confirm that the hydrogen bond between C128 and D156 is an important structural determinant of the channel's closing character.

5.2.1.3 The repetitive ChR2XXL activation

Furthermore, since the creation of ChR2XXL [127], it has been applied in behavioral investigations, mainly in Drosophila, such as circadian clock [131], locomotor behavior [130], and spatial learning [132]. Recently, its applications even have extended from the animal into plant research fields [62, 63]. But the electrophysiological characterization of the channel has not been fully explored yet. Unlike comparable variants such as ChR2(C128A), ChR2(C128S), and ChR2(D156A) that are well characterized [133-136], few studies are about the specific electrophysiological behavior of ChR2XXL(D156C) in response to different stimulation protocols. This work has shown that the ChR2XXL dynamics allow illumination sequences that increase or decrease currents based on when in the closing process channels are re-activated. Thereby these investigations help to fill in this gap and provide an important base for studying the intricate photocycle of channelrhodopsin.

5.2.1.4 Currents in MDCK cells

Currents produced by TR-ChR2XXLs in polarized MDCK cells were generally larger per μm^2 than that in HEK293 cells (Figure 4.8, **Section 4.2**), which likely involves the membrane geometry, native background ion currents, and TR-ChR2XXLs channel distribution. Nevertheless, the trend of normalized currents in each cell type was largely due to the effect of different TRs. Unlike the slightly decreased currents in the TR-tagged group compared to the untagged group in HEK293 cells, the currents in MDCK cells were larger, reflecting more TR-ChR2XXLs in the illuminated area in MDCK cells. The more collective location in the lateral membrane meant that more precise optogenetic currents can be achieved in epithelial cells.

The importance of plasma membrane potential of nonexcitable cells is far more than the role as an energetic driving force [221]. It participates in diverse cellular processes to establish and maintain morphological and functional features of epithelial cells, such as the regulation of cytoskeletal organization [222, 223], cell volume [224, 225], and wound healing [226, 227]. The most common depolarization approaches used in epithelial cells are chemical biology, such as the addition of drugs (like gramicidin, valinomycin, forskolin, etc.) [222, 228, 229], blockers of ion channels (like phenamil, barium, amiloride, etc.) [228, 230, 231], and modifications of the extracellular saline composition [222, 230]. However, these methods do not have spatial specificity, as they can change the potentials of both the apical and basolateral membranes synchronously. Besides, it takes some time to form the expectant depolarization by using these methods. For instance, using the gramicidin can only achieve its maximum depolarization 30 min after addition [224]. Nevertheless, the utilization of TR-ChR2XXLs can improve the spatial specificity of depolarization and drastically reduce the time required for depolarization. This will help to explore more functional roles played by basolateral membrane depolarization in biological processes.

5.2.2 Expression of TR-ChR2XXL in different cell types

5.2.2.1 The influence of promoter

One thing that should be noted in this work is that the protein ChR2XXL without TR used as a control was under the control of the human synapsin (hSyn) promoter, which is a neuron promoter, whereas the TR-tagged proteins were controlled by the CMV promoter that drives strong expression of genes in mammalian cells. Part of the different expression levels in different cell types may be attributed to the promoter. For example, the expressions of TR5-ChR2XXL driven by CMV promoter were a little higher in MDCK (1.12 ± 0.046) and HEK293 (1.08 ± 0.107) cells compared to that of ChR2XXL controlled by hSyn promoter (1 ± 0.059 in MDCK cells; 1 ± 0.080 in HEK293 cells) (Figure 4.14B, **Section 4.4**), which arose from the relatively weak function of hSyn promoter in these two cells [232]. However, according to the current knowledge and our experience, the genes driven by CMV promoter could express even better than hSyn promoter driven genes in neurons, since when neurons were transfected in parallel with CMV driven TO-ChR2opt-mKATE and hSyn driven TO-ChR2XXL-YFP, the TO-ChR2opt-mKATE expressed much better and faster than TO-ChR2XXL-YFP. So the obviously decreased expression of TR-ChR2XXLs in neurons (Figure 4.14) was not because of the promoter difference but caused by the mucin tandem repeats.

5.2.2.2 Expression of a specific TR-ChR2XXL in different cell types

As mentioned in Section 1.4.3, the mucin tandem repeats are highly glycosylated proteins. Their glycosylation is highly heterogeneous. First, it depends on the cell type in which the protein is expressed. The specific sugar chains and the number added to the peptide core depend on the cell type and the profile of glycosyltransferases expressed in that cell [175, 177, 233]. This may contribute to the different expressions of a specific protein in different cell types. For instance, TR15-ChR2XXL expressed much better in HEK293 cells than in neurons and MDCK cells (Figure 4.14). This difference may also result from the distinct capabilities of supporting the increased energy consumption caused by expressing exogenous proteins in different cells. In our experience, neurons are more susceptible to the metabolic stress of expressing a transgene than other cell types. Second, the glycosylation is developmentally regulated [177]. Glycosylation level, varying from 50% to 100% of available sites, depends on the context, such as the physiological state, which changes over time as the neuron matures *in vitro*. This may explain the phenomenon that TR5-ChR2XXL and TR10-ChR2XXL transfected neurons grew normally with well-extended dendrites and axons at the early stages, but gradually displayed abnormal morphologies like shrunken soma and degraded neurites at later stages, resulting in ultimate death (Figure 4.13).

5.2.2.3 Expression of TR-ChR2XXL in a specific cell type

Mucins are reported to participate in integrin-mediated cell adhesion to ECM. Integrins are transmembrane receptors that facilitate cell-ECM adhesion. Integrin is approximately 20 nm long. The extracellular domain of most membrane molecules does not extend more than 30 nm above the plasma membrane [234, 235]. However, in our cases the tandem repeats may project

out 25 nm, 50 nm, and 75 nm, respectively from cell surfaces, assuming a wormlike chain with a length of 2.5Å per amino acid [236]. It is reported that there is a delicate balance between adhesion and anti-adhesion forces in mucin-expressing cells [237-239]. The function mainly depends on the length of the mucin-like domain. Initially, the more tandem repeats, the weaker the cell adhesion to ECM, but if the tandem repeat is long enough, it will activate integrin clustering, leading to an increased cell adhesion on ECM [240-242]. In the present cases, when ChR2XXL was fused with more tandem repeats, it was more likely to hinder the interaction of integrin with ECM, but the tandem repeats used here were not sufficient to indirectly activate the integrin clustering. This provides an explanation for the observations that in neurons and polarized MDCK cells there were fewer expressing cells in the cases of channelrhodopsin with more tandem repeats since the ones that were not adhered well die or are washed off.

5.2.3 Subcellular localization of TR-ChR2XXL in polarized cells

The subcellular localization of all TR-tagged ChR2XXL constructs was in the lateral membrane in MDCK cells (Figure 4.9, **Section 4.3**), which was unexpected. Since previous reports indicated the ectodomain of MUC1 could rather confer apical localization on the basolateral CD2 molecule [243], and in Carol L. Kinlough's work, the addition of the targeting motif TR to Tac enhanced its apical delivery, but not basolateral delivery [178]. Probably, it was ChR2XXL that interacted with the TR motif leading to the change of the TR targeting pathway. Moreover, somatodendritic sorting signals are frequently encoded in the cytoplasmic tails of transmembrane proteins while axonal sorting signals are usually at the extracellular or transmembrane domains of proteins [158, 244]. However, in this work, the targeting motifs from extracellular domains unexpectedly directed ChR2XXL to the somatodendritic domain instead of the axonal domain in neurons (Figure 4.10), indicating we still need to understand the complex underlying mechanisms of polarized trafficking.

5.2.4 Strategies tried to improve the usability

Since the subcellular localization of the constructed optogenetic actuators was obvious, if the negative adhesion/viability issues that TRs produced in neurons could be solved, these new optogenetic tools could be used for more applications. Actually, two strategies were tried to solve the problem. The first strategy was to activate integrin by using anti-β1 stimulatory antibody TS2/16. In Jelle Wesseling et al.'s work [237], the reduction of adhesion induced by mucin can be reversed by mAb TS2/16 [245, 246]. But this antibody did not work in the present cases (data not shown). The difference between their work and this work is the number of tandem repeats used. The number they used is about 40, which is more than 15, the most tandem repeats number used in this work. So it is probable that the number of tandem repeats is critical in antibody TS2/16-mediated activation. The second one was the treatment of neurons with jacalin, which is a tetrameric lectin, a class of carbohydrate-binding proteins. It was reported that the treatment of jacalin promoted cell adherence within minutes due to the enhanced expression of integrin β3 [247]. From another aspect, jacalin can be used for isolating mucin

core-1type O-glycopeptides due to its ability to bind mucin-type O-glycans specially [233, 248, 249]. It was proposed that jacalin maybe can solve the problem. To figure out this, the transfected neurons were treated with jacalin. To achieve a better effect, vitronectin or fibronectin was additionally added to the normal coating medium when preparing glass coverslips since these two proteins are the main ECM receptors for integrin β3 [250, 251]. After 2-4 h recovery from electroporation, jacalin was added to the culture medium. However, unfortunately, these treatments did not improve the viability of these optogenetic actuators-expressing neurons (data not shown). Therefore, pending further improvements to the construct, the use of TR-tagged ChR2 is better suited to epithelia.

Besides, when culturing cells on substrates coated with ECM containing fibronectin, some phenomena were observed. The neurons had abnormal morphology and are aligned in a parallel array at the later growth stage. For MDCK cells, the cells at the edge of cell islands displayed elongation morphology. These observations were consistent with the founding that the fibronectin-matrix had elongation and alignment effects on cells since fibronectin fibers may guide the cell contact on the substrates by acting as a physical contact cue [252]. Interestingly, it seems that jacalin could relieve this effect, since with the higher concentration of jacalin, the elongation effect was slighter (Figure A.8 and Figure A.9). But this is beyond the topic of this work, and further investigation is needed.

5.2.5 Summary

In this part, three new optogenetic actuators (TR5-ChR2XXL, TR10-ChR2XXL, and TR15-ChR2XXL) were produced by adding different numbers of tandem repeats (TR5, TR10, and TR15) from mucin protein to the N-terminal domain of ChR2XXL. Despite the large and likely glycosylated TRs, the optical activation still generated high currents with kinetics similar to un-tagged ChR2XXL. In general, the construct expression in HEK293 cells was better than that in polarized cells but was also not subcellularly localized. Currents could be optically triggered in both HEK293 and polarized MDCK cells. In MDCK cells, all three actuators were localized to the lateral membrane, while in neurons those that expressed (TR5-ChR2XXL and TR10-ChR2XXL) were localized to the soma and dendrites. Expression differences were observed between cell types and within a cell type according to TR length, as well as depending on culture maturity. In polarized cells, the channelrhodopsins with more TRs had lower TE. In expressing neurons, TR5-ChR2XXL and TR10-ChR2XXL were somatodendritically targeted, but the expressing neurons did not survive through the fifth stage, while TR15-ChR2XXL neurons were abnormal even at early stages.

Overall, among these three actuators TR5-ChR2XXL has the best performance in cells, which could be used in particular research questions where optogenetics have as yet not been suitable. Modification of the membrane potential is critical not only in excitable cells like neurons, but also in nonexcitable cells like epithelia since membrane potential is involved in various biological processes [221, 231, 253]. Currents across epithelia need to be directional, therefore

spatial specificity in epithelia opens the use of optogenetics in various new cell types. For example, investigators could depolarize the basolateral membrane specifically while leaving the apical membrane potential unaffected, which could be utilized to explore the novel functional roles of basolateral membrane depolarization. Furthermore, optogenetic tools like CRY2/CIBN and iLID/SspB are used in research on cell migration, cell cycle, and cellular signaling pathway in epithelia [254-257], but most focus on the activity at the cellular level. If the TR targeting motifs are fused to these proteins, more precise subcellular manipulation in complex tissues could be achieved, which would expand remarkably the applications of optogenetics in biological research. Extending classical optogenetics, the constructed actuator can be applied for more precise spatial control of neural activities. This could be applied, for example, to map the subcellular neural circuits related to the establishment of cell polarity in early neuronal development.

Conclusion and outlook

Precise manipulation of complex neural networks is a pursued approach all the time in neuroscience, which benefits us to understand brain functions and thereby treat relevant diseases. The ideal manipulation should possess high spatiotemporal precision, non-invasiveness, and deep tissue penetration. Generally, optogenetics is still the most precise and efficient method that has profoundly revolutionized the neuroscience field. It can be applied at different levels of brain function, ranging from behavior to a single neuron. Considering the ultimate applications have to be transferred from simple model systems to higher multicellular organisms, higher standards are required. One of the requirements is finer spatial specificity because of the more complex neuronal networks and functions in higher organisms.

The higher spatial specificity of optogenetic manipulation can be achieved either by targeting the expression to a specific cellular compartment or by delivering the light to a specific region. The work presented focused on improving the subcellular specificity of optogenetic actuators by adopting the former strategy. Drawing on the natural subcellular targeting mechanisms of proteins in cells, the sorting motifs were utilized in this work to modify the classic optogenetic actuator, channelrhodopsin-2, in the hope to improve the spatial specificity. The first one was constructed by fusing a cytoplasmic tail of rhodopsin to the C-terminus of an optimized channelrhodopsin variant ChR2(H134R), whereas the second type was built by adding different numbers of tandem repeats from the extracellular domain of mucin to the N-terminus of the high current channelrhodopsin variant ChR2XXL. This work demonstrated that the fusion of the targeting motif to the optogenetic actuator is an effective way to confer new localization properties to the channelrhodopsin. These two types of actuators have different kinetics and characteristics, so they can be used for different applications. ChR2opt-AT can be used when moderate stimulation is needed, while TR-ChR2XXLs are useful for inducing prolonged depolarization without continuous illumination due to their slow off-kinetics. Overall, two types of subcellularly-localized optogenetic actuators were constructed in this work, and they could be used to probe cellular functions with increased spatial resolution.

Illustrating the underlying mechanisms of subcellular targeting of optogenetic actuators is valuable. Clear targeting mechanisms will provide guidance for designing more effective optogenetic actuators. This work proposed a potential mechanism for AT motif-guided targeting, but further investigation is still needed. Comparatively, TR motifs-guided targeting seems more complex, as they produced different impacts on different cell types, and the effects were also related to the length of TR. Taken together, both the apical targeting motifs in polarized epithelial cells, either from the C-terminus or N-terminus, primarily delivered channelrhodopsin to the somatodendrites of neurons. Since the majority of the subcellularly-localized channelrhodopsins are modified in their C-terminus, the present work on the modification of the N-terminus opens more possibilities to use N-terminal targeting motifs. In

addition, so far most of the known subcellularly plasma membrane-targeted optogenetic works have focused on utilizing neuron-specific targeting motifs, whereas this work verifies for the first time to our knowledge that epithelial targeting motifs can also be used for compartment-specific optogenetic actuators. In this way, the engineered subcellularly-localized actuators can be used not only in neurons, but also in non-neuronal cell types. In this case, the more precise optogenetic manipulation would promote our understanding of the subcellular function of the neurons and epithelium, and even on the whole of polarized cells.

Based on the promising outcomes in this work, further efforts could be done. I explored the intracellularly targeting issues with classic blue light-activated channelrhodopsins in this work, since they are available in our laboratory, along with the desired equipment. However, considering the scattering effect and limited penetration capability of blue light in practical applications, red light-activated channelrhodopsins are preferable. One can replace the ChR2opt or ChR2XXL with red light sensitive actuators, such as C1V1 and VChR1. Additionally, the modified optogenetic actuators in the present work were both excitatory tools. In fact, inhibitory actuators with subcellular specificity are also desired. The substitution of cationic ChR2 by inhibitory actuators could be a promising direction. But pending further improvements to the constructs, the use of TR-tagged actuators is better suited to epithelia. Also the existing suppressive tools have varying deficiencies, such as the requirement of high protein expression or high light power, or introduction of damage to the expressed cells or to the membrane properties [115, 258, 259]. So constructing effective subcellularly-localized inhibitory actuators will be challenging.

Moreover, this work focused on the subcellular targeting of optogenetic actuators for modulating the membrane potential. Meanwhile, subcellular targeting of various optogenetic tools for controlling other cellular parameters, like membrane composition, gene expression, and organelle localization [98, 99], are also thriving not only in neuroscience but also in other biological research. The past two decades have witnessed a fast-expanding period of the field of optogenetics. More refined optogenetic tools for solving specific optogenetic tasks will be a desired direction in the future. These tools will greatly advance our understanding of various biological processes and accelerate the progress of potential treatment of diseases with optogenetic approaches.

References

[1] Ganesh, S., et al., Cellular sociology regulates the hierarchical spatial patterning and organization of cells in organisms. Open Biol, 2020. 10(12): p. 200300.

[2] Piroli, M.E., J.O. Blanchette, and E. Jabbarzadeh, Polarity as a physiological modulator of cell function. Front Biosci (Landmark Ed), 2019. 24(3): p. 451-462.

[3] Lisa A. Urry, M.L.C., Steven A. Wasserman, Peter V. Minorsky, Rebecca B. Orr, Neil A. Campbell., Campbell biology. 2016.

[4] Thomson, W., On the Theory of the Electric Telegraph. Royal Society, 1854: p. 382-399.

[5] MichaelBeierlein, Cable Properties and Information Processing in Dendrites. 2014: p. 509-529.

[6] https://quizlet.com/42389859/synaptic-integration-flash-cards/.

[7] Hodgkin, A.L. and A.F. Huxley, A quantitative description of membrane current and its application to conduction and excitation in nerve. J Physiol, 1952. 117(4): p. 500-44.

[8] Letourneau, P.C., Possible roles for cell-to-substratum adhesion in neuronal morphogenesis. Developmental Biology, 1975. 44(1): p. 77-91.

[9] Banker, G., The Development of Neuronal Polarity: A Retrospective View. J Neurosci, 2018. 38(8): p. 1867-1873.

[10] Takano, T., et al., Neuronal polarization. Development, 2015. 142(12): p. 2088-93.

[11] Yogev, S. and K. Shen, Establishing Neuronal Polarity with Environmental and Intrinsic Mechanisms. Neuron, 2017. 96(3): p. 638-650.

[12] Arimura, N. and K. Kaibuchi, Neuronal polarity: from extracellular signals to intracellular mechanisms. Nat Rev Neurosci, 2007. 8(3): p. 194-205.

[13] Rodriguez-Boulan, E. and W.J. Nelson, Morphogenesis of the polarized epithelial cell phenotype. Science, 1989. 245(4919): p. 718-25.

[14] Caplan, K.S.M.M.J., Epithelial Cell Structure and Polarity. 2013: p. 3-43.

[15] Daly., H.K.D.T., Histology, Epithelial Cell. 2021.

[16] Riga, A., V.G. Castiglioni, and M. Boxem, New insights into apical-basal polarization in epithelia. Curr Opin Cell Biol, 2020. 62: p. 1-8.

[17] Yeaman, C., K.K. Grindstaff, and W.J. Nelson, New perspectives on mechanisms involved in generating epithelial cell polarity. Physiol Rev, 1999. 79(1): p. 73-98.

[18] Kim, C.K., A. Adhikari, and K. Deisseroth, Integration of optogenetics with complementary methodologies in systems neuroscience. Nat Rev Neurosci, 2017. 18(4): p. 222-235.

[19] Lee, C., et al., Light Up the Brain: The Application of Optogenetics in Cell-Type Specific Dissection of Mouse Brain Circuits. Front Neural Circuits, 2020. 14: p. 18.

[20] Atasoy, D. and S.M. Sternson, Chemogenetic Tools for Causal Cellular and Neuronal Biology. Physiol Rev, 2018. 98(1): p. 391-418.

[21] Roth, B.L., DREADDs for Neuroscientists. Neuron, 2016. 89(4): p. 683-94.

[22] Sternson, S.M. and B.L. Roth, Chemogenetic tools to interrogate brain functions. Annu Rev Neurosci, 2014. 37: p. 387-407.

[23] Honda, T., Optogenetic and thermogenetic manipulation of defined neural circuits and behaviors in Drosophila. Learn Mem, 2022. 29(4): p. 100-109.

[24] Ermakova, Y.G., et al., Thermogenetic neurostimulation with single-cell resolution. Nat Commun, 2017. 8: p. 15362.
[25] Bernstein, J.G., P.A. Garrity, and E.S. Boyden, Optogenetics and thermogenetics: technologies for controlling the activity of targeted cells within intact neural circuits. Curr Opin Neurobiol, 2012. 22(1): p. 61-71.
[26] Del Sol-Fernandez, S., et al., Magnetogenetics: remote activation of cellular functions triggered by magnetic switches. Nanoscale, 2022. 14(6): p. 2091-2118.
[27] Nimpf, S. and D.A. Keays, Is magnetogenetics the new optogenetics? EMBO J, 2017. 36(12): p. 1643-1646.
[28] Wheeler, M.A., et al., Genetically targeted magnetic control of the nervous system. Nat Neurosci, 2016. 19(5): p. 756-761.
[29] Stanley, S.A., et al., Bidirectional electromagnetic control of the hypothalamus regulates feeding and metabolism. Nature, 2016. 531(7596): p. 647-50.
[30] Rabut, C., et al., Ultrasound Technologies for Imaging and Modulating Neural Activity. Neuron, 2020. 108(1): p. 93-110.
[31] Azadeh, S.S., et al., Ultrasound and Sonogenetics: A New Perspective for Controlling Cells with Sound. Iran J Pharm Res, 2021. 20(3): p. 151-160.
[32] Wang, S., et al., Ultrasonic Neuromodulation and Sonogenetics: A New Era for Neural Modulation. Front Physiol, 2020. 11: p. 787.
[33] Kolesov, D.V., et al., Molecular Tools for Targeted Control of Nerve Cell Electrical Activity. Part I. Acta Naturae, 2021. 13(3): p. 52-64.
[34] Kolesov, D.V., et al., Molecular Tools for Targeted Control of Nerve Cell Electrical Activity. Part II. Acta Naturae, 2021. 13(4): p. 17-32.
[35] Yang, X., et al., Nanotechnology Enables Novel Modalities for Neuromodulation. Adv Mater, 2021. 33(52): p. e2103208.
[36] Li, X., et al., Nanotransducers for Wireless Neuromodulation. Matter, 2021. 4(5): p. 1484-1510.
[37] Faminzin, A.S., Die Wirkung des Lichtes auf die Bewegung der Chlamidomonas pulvisculus Ehr., Euglena viridis Ehr. Und Oscillatoria insignis Tw. In Melanges Biologiques tires du Bulletin de l'Ácademie Imperial des Sciences De St.-Petersbourg. 1866: p. 73–93.
[38] Crick, F.H., Thinking about the brain. Scientific American, 1979. 219–232: p. 219–232.
[39] Yizhar, O., et al., Optogenetics in neural systems. Neuron, 2011. 71(1): p. 9-34.
[40] Zemelman, B.V., et al., Selective photostimulation of genetically chARGed neurons. Neuron, 2002. 33(1): p. 15-22.
[41] Nagel, G., et al., Channelrhodopsin-1: a light-gated proton channel in green algae. Science, 2002. 296(5577): p. 2395-8.
[42] Nagel, G., et al., Channelrhodopsin-2, a directly light-gated cation-selective membrane channel. Proc Natl Acad Sci U S A, 2003. 100(24): p. 13940-5.
[43] Boyden, E.S., et al., Millisecond-timescale, genetically targeted optical control of neural activity. Nat Neurosci, 2005. 8(9): p. 1263-8.
[44] Li, X., et al., Fast noninvasive activation and inhibition of neural and network activity by vertebrate rhodopsin and green algae channelrhodopsin. Proc Natl Acad Sci U S A, 2005. 102(49): p. 17816-21.
[45] Nagel, G., et al., Light activation of channelrhodopsin-2 in excitable cells of Caenorhabditis elegans triggers rapid behavioral responses. Curr Biol, 2005. 15(24): p. 2279-84.

[46] Bi, A., et al., Ectopic expression of a microbial-type rhodopsin restores visual responses in mice with photoreceptor degeneration. Neuron, 2006. 50(1): p. 23-33.
[47] Ishizuka, T., et al., Kinetic evaluation of photosensitivity in genetically engineered neurons expressing green algae light-gated channels. Neurosci Res, 2006. 54(2): p. 85-94.
[48] Deisseroth, K., et al., Next-generation optical technologies for illuminating genetically targeted brain circuits. J Neurosci, 2006. 26(41): p. 10380-6.
[49] Adamantidis, A.R., et al., Neural substrates of awakening probed with optogenetic control of hypocretin neurons. Nature, 2007. 450(7168): p. 420-4.
[50] Oesterhelt, D. and W. Stoeckenius, Rhodopsin-like protein from the purple membrane of Halobacterium halobium. Nat New Biol, 1971. 233(39): p. 149-52.
[51] Matsuno-Yagi, A. and Y. Mukohata, Two possible roles of bacteriorhodopsin; a comparative study of strains of Halobacterium halobium differing in pigmentation. Biochemical and Biophysical Research Communications, 1977. 78(1): p. 237-243.
[52] Deisseroth, K., Optogenetics. Nat Methods, 2011. 8(1): p. 26-9.
[53] Boyle, P.M., T.V. Karathanos, and N.A. Trayanova, Cardiac Optogenetics: 2018. JACC Clin Electrophysiol, 2018. 4(2): p. 155-167.
[54] Koopman, C.D., et al., Cardiac optogenetics: using light to monitor cardiac physiology. Basic Res Cardiol, 2017. 112(5): p. 56.
[55] Entcheva, E. and M.W. Kay, Cardiac optogenetics: a decade of enlightenment. Nat Rev Cardiol, 2021. 18(5): p. 349-367.
[56] Kleinlogel, S., et al., Emerging Approaches for Restoration of Hearing and Vision. Physiol Rev, 2020. 100(4): p. 1467-1525.
[57] Baker, C.K. and J.G. Flannery, Innovative Optogenetic Strategies for Vision Restoration. Front Cell Neurosci, 2018. 12: p. 316.
[58] Roska, B. and J.A. Sahel, Restoring vision. Nature, 2018. 557(7705): p. 359-367.
[59] Bryson, J.B., et al., Restoring motor function using optogenetics and neural engraftment. Curr Opin Biotechnol, 2016. 40: p. 75-81.
[60] Weitz, A.J. and J.H. Lee, Probing Neural Transplant Networks In Vivo with Optogenetics and Optogenetic fMRI. Stem Cells Int, 2016. 2016: p. 8612751.
[61] Keshmiri Neghab, H., et al., The state of the art of biomedical applications of optogenetics. Lasers Surg Med, 2022. 54(2): p. 202-216.
[62] Reyer, A., et al., Channelrhodopsin-mediated optogenetics highlights a central role of depolarization-dependent plant proton pumps. Proc Natl Acad Sci U S A, 2020. 117(34): p. 20920-20925.
[63] Zhou, Y., et al., Advances and prospects of rhodopsin-based optogenetics in plant research. Plant Physiol, 2021. 187(2): p. 572-589.
[64] https://www.geg-tech.com/services/optogenetics/.
[65] Rost, B.R., et al., Optogenetic Tools for Subcellular Applications in Neuroscience. Neuron, 2017. 96(3): p. 572-603.
[66] Kato, H.E., Structure-Function Relationship of Channelrhodopsins. Adv Exp Med Biol, 2021. 1293: p. 35-53.
[67] Shichida, Y. and T. Matsuyama, Evolution of opsins and phototransduction. Philos Trans R Soc Lond B Biol Sci, 2009. 364(1531): p. 2881-95.

[68] Koyanagi, M. and A. Terakita, Diversity of animal opsin-based pigments and their optogenetic potential. Biochim Biophys Acta, 2014. 1837(5): p. 710-6.
[69] Ernst, O.P., et al., Microbial and animal rhodopsins: structures, functions, and molecular mechanisms. Chem Rev, 2014. 114(1): p. 126-63.
[70] Dennis Eickelbeck, R.K., Stefan Herlitze1, Katharina Spoida, Optogenetic Approaches for Controlling Neuronal Activity and Plasticity. Handbook of In Vivo Neural Plasticity Techniques, 2019.
[71] Karra, D. and R. Dahm, Transfection Techniques for Neuronal Cells. Journal of Neuroscience, 2010. 30(18): p. 6171-6177.
[72] Kim, T.K. and J.H. Eberwine, Mammalian cell transfection: the present and the future. Anal Bioanal Chem, 2010. 397(8): p. 3173-8.
[73] Gerits, A. and W. Vanduffel, Optogenetics in primates: a shining future? Trends Genet, 2013. 29(7): p. 403-11.
[74] Barnett, S.C., et al., Optogenetic stimulation: Understanding memory and treating deficits. Hippocampus, 2018. 28(7): p. 457-470.
[75] Zeitelhofer, M., et al., High-efficiency transfection of mammalian neurons via nucleofection. Nat Protoc, 2007. 2(7): p. 1692-704.
[76] Potter, H. and R. Heller, Transfection by Electroporation. Curr Protoc Mol Biol, 2018. 121: p. 9 3 1-9 3 13.
[77] AnnetteGärtnerLudovicCollinGiovannaLalli, Nucleofection of Primary Neurons. Methods in Enzymology, 2006. 406: p. 374-388.
[78] Zeitelhofer, M., et al., Transfection of cultured primary neurons via nucleofection. Curr Protoc Neurosci, 2009. Chapter 4: p. Unit4 32.
[79] Arenkiel, B.R., et al., In vivo light-induced activation of neural circuitry in transgenic mice expressing channelrhodopsin-2. Neuron, 2007. 54(2): p. 205-18.
[80] Hagglund, M., et al., Activation of groups of excitatory neurons in the mammalian spinal cord or hindbrain evokes locomotion. Nat Neurosci, 2010. 13(2): p. 246-52.
[81] Atasoy, D., et al., A FLEX switch targets Channelrhodopsin-2 to multiple cell types for imaging and long-range circuit mapping. J Neurosci, 2008. 28(28): p. 7025-30.
[82] Madisen, L., et al., A toolbox of Cre-dependent optogenetic transgenic mice for light-induced activation and silencing. Nat Neurosci, 2012. 15(5): p. 793-802.
[83] Repina, N.A., et al., At Light Speed: Advances in Optogenetic Systems for Regulating Cell Signaling and Behavior. Annu Rev Chem Biomol Eng, 2017. 8: p. 13-39.
[84] Towne, C. and K.R. Thompson, Overview on Research and Clinical Applications of Optogenetics. Curr Protoc Pharmacol, 2016. 75: p. 11 19 1-11 19 21.
[85] Bansal, A., S. Shikha, and Y. Zhang, Towards translational optogenetics. Nat Biomed Eng, 2022.
[86] Zhang, Y., et al., Battery-free, lightweight, injectable microsystem for in vivo wireless pharmacology and optogenetics. Proc Natl Acad Sci U S A, 2019. 116(43): p. 21427-21437.
[87] Gradinaru, V., et al., Targeting and readout strategies for fast optical neural control in vitro and in vivo. J Neurosci, 2007. 27(52): p. 14231-8.
[88] Zhang, F., et al., Optogenetic interrogation of neural circuits: technology for probing mammalian brain structures. Nat Protoc, 2010. 5(3): p. 439-56.
[89] MattCarterJenniferShieh, Electrophysiology. 2015: p. 89-115.

[90] Spira, M.E. and A. Hai, Multi-electrode array technologies for neuroscience and cardiology. Nat Nanotechnol, 2013. 8(2): p. 83-94.
[91] Zhou, Y., et al., Optical Electrophysiology: Toward the Goal of Label-Free Voltage Imaging. J Am Chem Soc, 2021. 143(28): p. 10482-10499.
[92] Passaro, A.P. and S.L. Stice, Electrophysiological Analysis of Brain Organoids: Current Approaches and Advancements. Frontiers in Neuroscience, 2021. 14.
[93] Lee, J.H., et al., Global and local fMRI signals driven by neurons defined optogenetically by type and wiring. Nature, 2010. 465(7299): p. 788-92.
[94] Takata, N., et al., Optogenetic astrocyte activation evokes BOLD fMRI response with oxygen consumption without neuronal activity modulation. Glia, 2018. 66(9): p. 2013-2023.
[95] Zalocusky, K. and K. Deisseroth, Optogenetics in the behaving rat: integration of diverse new technologies in a vital animal model. Optogenetics, 2013. 1: p. 1-17.
[96] Packer, A.M., B. Roska, and M. Hausser, Targeting neurons and photons for optogenetics. Nat Neurosci, 2013. 16(7): p. 805-15.
[97] Zhang, Y.P. and T.G. Oertner, Optical induction of synaptic plasticity using a light-sensitive channel. Nat Methods, 2007. 4(2): p. 139-41.
[98] Kichuk, T.C., C. Carrasco-Lopez, and J.L. Avalos, Lights up on organelles: Optogenetic tools to control subcellular structure and organization. WIREs Mech Dis, 2021. 13(1): p. e1500.
[99] Manoilov, K.Y., V.V. Verkhusha, and D.M. Shcherbakova, A guide to the optogenetic regulation of endogenous molecules. Nat Methods, 2021. 18(9): p. 1027-1037.
[100] Garrido, J.J., et al., A targeting motif involved in sodium channel clustering at the axonal initial segment. Science, 2003. 300(5628): p. 2091-4.
[101] Grubb, M.S. and J. Burrone, Channelrhodopsin-2 localised to the axon initial segment. PLoS One, 2010. 5(10): p. e13761.
[102] Zhang, Z., et al., Targeted Expression of Channelrhodopsin-2 to the Axon Initial Segment Alters the Temporal Firing Properties of Retinal Ganglion Cells. PLoS One, 2015. 10(11): p. e0142052.
[103] Rost, B.R., et al., Optogenetic acidification of synaptic vesicles and lysosomes. Nat Neurosci, 2015. 18(12): p. 1845-1852.
[104] Hegemann, P., Vision in microalgae. Planta, 1997. 203(3): p. 265-74.
[105] Schneider, F., C. Grimm, and P. Hegemann, Biophysics of Channelrhodopsin. Annu Rev Biophys, 2015. 44: p. 167-86.
[106] N.G.A.Tan，W.Wu，A.M.Seifalian, Optogenetics: lights, camera, action! A ray of light, a shadow unmasked. Applications of Nanoscience in Photomedicine, 2015.
[107] Wietek, J. and M. Prigge, Enhancing Channelrhodopsins: An Overview. Methods Mol Biol, 2016. 1408: p. 141-65.
[108] Grossman, N., et al., Modeling study of the light stimulation of a neuron cell with channelrhodopsin-2 mutants. IEEE Trans Biomed Eng, 2011. 58(6): p. 1742-51.
[109] Lin, J.Y., A user's guide to channelrhodopsin variants: features, limitations and future developments. Exp Physiol, 2011. 96(1): p. 19-25.
[110] Williams, J.C., et al., Computational optogenetics: empirically-derived voltage- and light-sensitive channelrhodopsin-2 model. PLoS Comput Biol, 2013. 9(9): p. e1003220.
[111] Zhang, F., et al., The microbial opsin family of optogenetic tools. Cell, 2011. 147(7): p. 1446-57.
[112] Kato, H.E., et al., Crystal structure of the channelrhodopsin light-gated cation channel. Nature, 2012. 482(7385): p. 369-74.

[113] Deisseroth, K. and P. Hegemann, The form and function of channelrhodopsin. Science, 2017. 357(6356).
[114] Zhang, F., et al., Red-shifted optogenetic excitation: a tool for fast neural control derived from Volvox carteri. Nat Neurosci, 2008. 11(6): p. 631-3.
[115] Prigge, M., et al., Color-tuned channelrhodopsins for multiwavelength optogenetics. J Biol Chem, 2012. 287(38): p. 31804-12.
[116] Lin, J.Y., et al., ReaChR: a red-shifted variant of channelrhodopsin enables deep transcranial optogenetic excitation. Nat Neurosci, 2013. 16(10): p. 1499-508.
[117] Klapoetke, N.C., et al., Independent optical excitation of distinct neural populations. Nat Methods, 2014. 11(3): p. 338-46.
[118] Gunaydin, L.A., et al., Ultrafast optogenetic control. Nat Neurosci, 2010. 13(3): p. 387-92.
[119] Lin, J.Y., et al., Characterization of engineered channelrhodopsin variants with improved properties and kinetics. Biophys J, 2009. 96(5): p. 1803-14.
[120] Pan, Z.H., et al., ChR2 mutants at L132 and T159 with improved operational light sensitivity for vision restoration. PLoS One, 2014. 9(6): p. e98924.
[121] Berndt, A., et al., Structure-guided transformation of channelrhodopsin into a light-activated chloride channel. Science, 2014. 344(6182): p. 420-4.
[122] Berndt, A., et al., Structural foundations of optogenetics: Determinants of channelrhodopsin ion selectivity. Proc Natl Acad Sci U S A, 2016. 113(4): p. 822-9.
[123] Wietek, J., et al., Conversion of channelrhodopsin into a light-gated chloride channel. Science, 2014. 344(6182): p. 409-12.
[124] Wietek, J., et al., An improved chloride-conducting channelrhodopsin for light-induced inhibition of neuronal activity in vivo. Sci Rep, 2015. 5: p. 14807.
[125] John Y. Lin, P.M.K.a.A.M., Discovery and Development of Spectrally Diverse Channelrhodopsins (ChR) for Neurobiological Applications. New Techniques in Systems Neuroscience, 2015.
[126] Alexander M. Herman, J.M.P., and Benjamin R. Arenkiel, Optogenetic Approaches to Investigating Brain Circuits. 2017.
[127] Dawydow, A., et al., Channelrhodopsin-2-XXL, a powerful optogenetic tool for low-light applications. Proc Natl Acad Sci U S A, 2014. 111(38): p. 13972-7.
[128] Lorenz-Fonfria, V.A., et al., Transient protonation changes in channelrhodopsin-2 and their relevance to channel gating. Proc Natl Acad Sci U S A, 2013. 110(14): p. E1273-81.
[129] Higgins, J., et al., Considerations in repetitive activation of light sensitive ion channels for long-term studies: Channel rhodopsin in the Drosophila model. Neurosci Res, 2017. 125: p. 1-10.
[130] Mattingly, M., et al., Hyperpolarization by activation of halorhodopsin results in enhanced synaptic transmission: Neuromuscular junction and CNS circuit. PLoS One, 2018. 13(7): p. e0200107.
[131] Selcho, M., et al., Central and peripheral clocks are coupled by a neuropeptide pathway in Drosophila. Nat Commun, 2017. 8: p. 15563.
[132] Meda, N., et al., Searching for relief: Drosophila melanogaster navigation in a virtual bitter maze. Behav Brain Res, 2020. 389: p. 112616.
[133] Berndt, A., et al., Bi-stable neural state switches. Nat Neurosci, 2009. 12(2): p. 229-34.
[134] Bamann, C., et al., Structural guidance of the photocycle of channelrhodopsin-2 by an interhelical hydrogen bond. Biochemistry, 2010. 49(2): p. 267-78.

[135] Prakash, R., et al., Two-photon optogenetic toolbox for fast inhibition, excitation and bistable modulation. Nat Methods, 2012. 9(12): p. 1171-9.
[136] Perny, M., et al., Chronic activation of the D156A point mutant of Channelrhodopsin-2 signals apoptotic cell death: the good and the bad. Cell Death Dis, 2016. 7(11): p. e2447.
[137] Mostov, K.E., M. Verges, and Y. Altschuler, Membrane traffic in polarized epithelial cells. Current Opinion in Cell Biology, 2000. 12(4): p. 483-490.
[138] Arnold, D.B., Actin and microtubule-based cytoskeletal cues direct polarized targeting of proteins in neurons. Sci Signal, 2009. 2(83): p. pe49.
[139] Lasiecka, Z.M., et al., Compartmentalizing the neuronal plasma membrane from axon initial segments to synapses. Int Rev Cell Mol Biol, 2009. 272: p. 303-89.
[140] Bentley, M. and G. Banker, The cellular mechanisms that maintain neuronal polarity. Nat Rev Neurosci, 2016. 17(10): p. 611-22.
[141] von Bartheld, C.S., Axonal transport and neuronal transcytosis of trophic factors, tracers, and pathogens. J Neurobiol, 2004. 58(2): p. 295-314.
[142] Lasiecka, Z.M. and B. Winckler, Mechanisms of polarized membrane trafficking in neurons -- focusing in on endosomes. Mol Cell Neurosci, 2011. 48(4): p. 278-87.
[143] Radler, M.R., A. Suber, and E.T. Spiliotis, Spatial control of membrane traffic in neuronal dendrites. Mol Cell Neurosci, 2020. 105: p. 103492.
[144] Ohnishi, A.T.a.S.-i., Restriction of the Lateral Motion of Band 3 in the Erythrocyte Membrane by the Cytoskeletal Network: Dependence on Spectrin Association State1. Biochemistry, 1986(25): p. 6133-6139.
[145] Winckler, B., P. Forscher, and I. Mellman, A diffusion barrier maintains distribution of membrane proteins in polarized neurons. Nature, 1999. 397(6721): p. 698-701.
[146] Kiebler, M.A. and G.J. Bassell, Neuronal RNA granules: movers and makers. Neuron, 2006. 51(6): p. 685-90.
[147] Hengst, U. and S.R. Jaffrey, Function and translational regulation of mRNA in developing axons. Semin Cell Dev Biol, 2007. 18(2): p. 209-15.
[148] Doyle, M. and M.A. Kiebler, Mechanisms of dendritic mRNA transport and its role in synaptic tagging. EMBO J, 2011. 30(17): p. 3540-52.
[149] Sahoo, P.K., et al., Axonal mRNA transport and translation at a glance. J Cell Sci, 2018. 131(8).
[150] Hong, W., SNAREs and traffic. Biochim Biophys Acta, 2005. 1744(2): p. 120-44.
[151] Jareb, M. and G. Banker, The Polarized Sorting of Membrane Proteins Expressed in Cultured Hippocampal Neurons Using Viral Vectors. Neuron, 1998. 20(5): p. 855-867.
[152] Pietrini, G., et al., The axonal gamma-aminobutyric acid transporter GAT-1 is sorted to the apical membranes of polarized epithelial cells. J Biol Chem, 1994. 269(6): p. 4668-74.
[153] Farias, G.G., et al., Signal-mediated, AP-1/clathrin-dependent sorting of transmembrane receptors to the somatodendritic domain of hippocampal neurons. Neuron, 2012. 75(5): p. 810-23.
[154] Yap, C.C., et al., Pathway selection to the axon depends on multiple targeting signals in NgCAM. J Cell Sci, 2008. 121(Pt 9): p. 1514-25.
[155] Wisco, D., et al., Uncovering multiple axonal targeting pathways in hippocampal neurons. J Cell Biol, 2003. 162(7): p. 1317-28.
[156] Francesconi, A. and R.M. Duvoisin, Alternative splicing unmasks dendritic and axonal targeting signals in metabotropic glutamate receptor 1. J Neurosci, 2002. 22(6): p. 2196-205.

[157] Dotti, C.G. and K. Simons, Polarized sorting of viral glycoproteins to the axon and dendrites of hippocampal neurons in culture. Cell, 1990. 62(1): p. 63-72.
[158] West, A.E., R.L. Neve, and K.M. Buckley, Identification of a Somatodendritic Targeting Signal in the Cytoplasmic Domain of the Transferrin Receptor. The Journal of Neuroscience, 1997. 17(16): p. 6038-6047.
[159] Odorizzi, G. and I.S. Trowbridge, Structural requirements for basolateral sorting of the human transferrin receptor in the biosynthetic and endocytic pathways of Madin-Darby canine kidney cells. J Cell Biol, 1997. 137(6): p. 1255-64.
[160] Lewis, T.L., Jr., et al., Myosin-dependent targeting of transmembrane proteins to neuronal dendrites. Nat Neurosci, 2009. 12(5): p. 568-76.
[161] Lewis, T.L., Jr., T. Mao, and D.B. Arnold, A role for myosin VI in the localization of axonal proteins. PLoS Biol, 2011. 9(3): p. e1001021.
[162] Baker, C.A., et al., Cellular resolution circuit mapping with temporal-focused excitation of soma-targeted channelrhodopsin. Elife, 2016. 5.
[163] Schuck, S. and K. Simons, Polarized sorting in epithelial cells: raft clustering and the biogenesis of the apical membrane. J Cell Sci, 2004. 117(Pt 25): p. 5955-64.
[164] Rodriguez-Boulan, E., G. Kreitzer, and A. Musch, Organization of vesicular trafficking in epithelia. Nat Rev Mol Cell Biol, 2005. 6(3): p. 233-47.
[165] Deretic, D., et al., Rhodopsin C terminus, the site of mutations causing retinal disease, regulates trafficking by binding to ADP-ribosylation factor 4 (ARF4). Proc Natl Acad Sci U S A, 2005. 102(9): p. 3301-6.
[166] Wang, J. and D. Deretic, Molecular complexes that direct rhodopsin transport to primary cilia. Prog Retin Eye Res, 2014. 38: p. 1-19.
[167] Thuenauer, R., et al., Four-dimensional live imaging of apical biosynthetic trafficking reveals a post-Golgi sorting role of apical endosomal intermediates. Proc Natl Acad Sci U S A, 2014. 111(11): p. 4127-32.
[168] Deretic, D., et al., Regulation of sorting and post-Golgi trafficking of rhodopsin by its C-terminal sequence QVS(A)PA. Proc Natl Acad Sci U S A, 1998. 95(18): p. 10620-5.
[169] Deretic, D., A role for rhodopsin in a signal transduction cascade that regulates membrane trafficking and photoreceptor polarity. Vision Res, 2006. 46(27): p. 4427-33.
[170] Palczewski, K., G protein-coupled receptor rhodopsin. Annu Rev Biochem, 2006. 75: p. 743-67.
[171] Chuang, J.Z. and C.H. Sung, The cytoplasmic tail of rhodopsin acts as a novel apical sorting signal in polarized MDCK cells. J Cell Biol, 1998. 142(5): p. 1245-56.
[172] Kaur, S., et al., Mucins in pancreatic cancer and its microenvironment. Nat Rev Gastroenterol Hepatol, 2013. 10(10): p. 607-20.
[173] Pittler, S.J., S.J. Fliesler, and W. Baehr, Primary structure of frog rhodopsin. FEBS Letters, 1992. 313(2): p. 103-108.
[174] Lamblin, G., et al., Human airway mucin glycosylation: a combinatory of carbohydrate determinants which vary in cystic fibrosis. Glycoconj J, 2001. 18(9): p. 661-84.
[175] Gendler, S.J., MUC1, the renaissance molecule. J Mammary Gland Biol Neoplasia, 2001. 6(3): p. 339-53.
[176] Gendler, S.J., et al., Molecular cloning and expression of human tumor-associated polymorphic epithelial mucin. J Biol Chem, 1990. 265(25): p. 15286-93.

[177] Hattrup, C.L. and S.J. Gendler, Structure and function of the cell surface (tethered) mucins. Annu Rev Physiol, 2008. 70: p. 431-57.
[178] Kinlough, C.L., et al., Core-glycosylated mucin-like repeats from MUC1 are an apical targeting signal. J Biol Chem, 2011. 286(45): p. 39072-81.
[179] Zheng, X. and J.E. Sadler, Mucin-like domain of enteropeptidase directs apical targeting in Madin-Darby canine kidney cells. J Biol Chem, 2002. 277(9): p. 6858-63.
[180] Neher, E. and B. Sakmann, Noise analysis of drug induced voltage clamp currents in denervated frog muscle fibres. J Physiol, 1976. 258(3): p. 705-29.
[181] Neher, E., B. Sakmann, and J.H. Steinbach, The extracellular patch clamp: a method for resolving currents through individual open channels in biological membranes. Pflugers Arch, 1978. 375(2): p. 219-28.
[182] Hamill, O.P., et al., Improved patch-clamp techniques for high-resolution current recording from cells and cell-free membrane patches. Pflugers Arch, 1981. 391(2): p. 85-100.
[183] Bell, M.D., Patch Clamp Electrophysiology. 2021.
[184] Sophie Veitinger , D., The Patch-Clamp Technique. 2011.
[185] Jin, L., Optical control of primary rat cortical neural activity in vitro. 2016.
[186] Clause, B.T., The Wistar Rat as a right choice: establishing mammalian standards and the ideal of a standardized mammal. J Hist Biol, 1993. 26(2): p. 329-49.
[187] Brewer, G.J., et al., Optimized survival of hippocampal neurons in B27-supplemented Neurobasal, a new serum-free medium combination. J Neurosci Res, 1993. 35(5): p. 567-76.
[188] Maybeck, V., Tools for non-invasive communication with electrogenic cells: optogenetic stimulation and diamond recording devices. 2011.
[189] Shcherbo, D., et al., Bright far-red fluorescent protein for whole-body imaging. Nat Methods, 2007. 4(9): p. 741-6.
[190] Gradinaru, V., et al., Molecular and cellular approaches for diversifying and extending optogenetics. Cell, 2010. 141(1): p. 154-165.
[191] Gaush, C.R., W.L. Hard, and T.F. Smith, Characterization of an established line of canine kidney cells (MDCK). Proc Soc Exp Biol Med, 1966. 122(3): p. 931-5.
[192] Dukes, J.D., P. Whitley, and A.D. Chalmers, The MDCK variety pack: choosing the right strain. BMC Cell Biol, 2011. 12: p. 43.
[193] Zegers, M.M.P., et al., Epithelial polarity and tubulogenesis in vitro. Trends in Cell Biology, 2003. 13(4): p. 169-176.
[194] Meder, D., et al., Gp135/podocalyxin and NHERF-2 participate in the formation of a preapical domain during polarization of MDCK cells. J Cell Biol, 2005. 168(2): p. 303-13.
[195] Ojakian, G.K. and R. Schwimmer, The polarized distribution of an apical cell surface glycoprotein is maintained by interactions with the cytoskeleton of Madin-Darby canine kidney cells. J Cell Biol, 1988. 107(6 Pt 1): p. 2377-87.
[196] Zou, P., et al., Bright and fast multicoloured voltage reporters via electrochromic FRET. Nat Commun, 2014. 5: p. 4625.
[197] Zimmermann, D., et al., Effects on capacitance by overexpression of membrane proteins. Biochem Biophys Res Commun, 2008. 369(4): p. 1022-6.
[198] Chow, B.Y., et al., High-performance genetically targetable optical neural silencing by light-driven proton pumps. Nature, 2010. 463(7277): p. 98-102.

[199] Connors, B.W. and M.J. Gutnick, Intrinsic firing patterns of diverse neocortical neurons. Trends in Neurosciences, 1990. 13(3): p. 99-104.
[200] Saito, Y. and T. Isa, Electrophysiological and morphological properties of neurons in the rat superior colliculus. I. Neurons in the intermediate layer. J Neurophysiol, 1999. 82(2): p. 754-67.
[201] Thomas, P. and T.G. Smart, HEK293 cell line: a vehicle for the expression of recombinant proteins. J Pharmacol Toxicol Methods, 2005. 51(3): p. 187-200.
[202] Karmazinova, M. and L. Lacinova, Measurement of cellular excitability by whole cell patch clamp technique. Physiol Res, 2010. 59 Suppl 1: p. S1-S7.
[203] Tahirovic, S. and F. Bradke, Neuronal polarity. Cold Spring Harb Perspect Biol, 2009. 1(3): p. a001644.
[204] Dotti, C.G., C.A. Sullivan, and G.A. Banker, The establishment of polarity by hippocampal neurons in culture. The Journal of Neuroscience, 1988. 8(4): p. 1454-1468.
[205] Bower, J.M., Beeman, D., Ion Channels in Bursting Neurons. The Book of GENESIS, 1998.
[206] Zhang, W., et al., Axonal sodium and potassium conductance density determines spiking dynamical properties of regular- and fast-spiking neurons. Nonlinear Dynamics, 2018. 95(2): p. 1035-1052.
[207] Xiao, Q., et al., Cytoskeleton Molecular Motors: Structures and Their Functions in Neuron. Int J Biol Sci, 2016. 12(9): p. 1083-92.
[208] Tai, A.W., et al., Rhodopsin's Carboxy-Terminal Cytoplasmic Tail Acts as a Membrane Receptor for Cytoplasmic Dynein by Binding to the Dynein Light Chain Tctex-1. Cell, 1999. 97(7): p. 877-887.
[209] Rosenbaum, J.L. and G.B. Witman, Intraflagellar transport. Nat Rev Mol Cell Biol, 2002. 3(11): p. 813-25.
[210] Tai, A.W., J.Z. Chuang, and C.H. Sung, Cytoplasmic dynein regulation by subunit heterogeneity and its role in apical transport. J Cell Biol, 2001. 153(7): p. 1499-509.
[211] Yeh, T.Y., et al., Regulatory dissociation of Tctex-1 light chain from dynein complex is essential for the apical delivery of rhodopsin. Traffic, 2006. 7(11): p. 1495-502.
[212] Jacob, S.Z.a.R., Tubulin Detyrosination in Epithelial Cells. 2015: p. 187–194.
[213] Sferra, A., F. Nicita, and E. Bertini, Microtubule Dysfunction: A Common Feature of Neurodegenerative Diseases. Int J Mol Sci, 2020. 21(19).
[214] Papagiakoumou, E., et al., Scanless two-photon excitation of channelrhodopsin-2. Nat Methods, 2010. 7(10): p. 848-54.
[215] Oron, D., et al., Two-photon optogenetics. Prog Brain Res, 2012. 196: p. 119-43.
[216] Papagiakoumou, E., E. Ronzitti, and V. Emiliani, Scanless two-photon excitation with temporal focusing. Nat Methods, 2020. 17(6): p. 571-581.
[217] Packer, A.M., et al., Simultaneous all-optical manipulation and recording of neural circuit activity with cellular resolution in vivo. Nat Methods, 2015. 12(2): p. 140-6.
[218] Saita, M., et al., Photoexcitation of the P4(480) State Induces a Secondary Photocycle That Potentially Desensitizes Channelrhodopsin-2. J Am Chem Soc, 2018. 140(31): p. 9899-9903.
[219] Becker-Baldus, J., et al., Enlightening the photoactive site of channelrhodopsin-2 by DNP-enhanced solid-state NMR spectroscopy. Proc Natl Acad Sci U S A, 2015. 112(32): p. 9896-901.
[220] Becker-Baldus, J., et al., The Desensitized Channelrhodopsin-2 Photointermediate Contains 13 -cis, 15 -syn Retinal Schiff Base. Angew Chem Int Ed Engl, 2021. 60(30): p. 16442-16447.

[221] Olivotto, M., et al., Electric fields at the plasma membrane level: a neglected element in the mechanisms of cell signalling. Bioessays, 1996. 18(6): p. 495-504.
[222] Chifflet, S., et al., Nonspecific depolarization of the plasma membrane potential induces cytoskeletal modifications of bovine corneal endothelial cells in culture. Exp Cell Res, 2003. 282(1): p. 1-13.
[223] Chifflet, S. and J.A. Hernandez, The plasma membrane potential and the organization of the actin cytoskeleton of epithelial cells. Int J Cell Biol, 2012. 2012: p. 121424.
[224] Hernandez, J.A. and E. Cristina, Modeling cell volume regulation in nonexcitable cells: the roles of the Na+ pump and of cotransport systems. Am J Physiol, 1998. 275(4): p. C1067-80.
[225] Lang, F., et al., Functional significance of cell volume regulatory mechanisms. Physiol Rev, 1998. 78(1): p. 247-306.
[226] Reid, B. and M. Zhao, The Electrical Response to Injury: Molecular Mechanisms and Wound Healing. Adv Wound Care (New Rochelle), 2014. 3(2): p. 184-201.
[227] Chifflet, S. and J.A. Hernandez, The Epithelial Sodium Channel and the Processes of Wound Healing. Biomed Res Int, 2016. 2016: p. 5675047.
[228] Paulmichl, M., G. Gstraunthaler, and F. Lang, Electrical properties of Madin-Darby canine kidney cells. Effects of extracellular potassium and bicarbonate. Pflugers Arch, 1985. 405(2): p. 102-7.
[229] Breuer, W.V., E. Mack, and A. Rothstein, Activation of K+ and Cl- channels by Ca2+ and cyclic AMP in dissociated kidney epithelial (MDCK) cells. Pflugers Arch, 1988. 411(4): p. 450-5.
[230] Paulmichl, M., F. Friedrich, and F. Lang, Electrical properties of Madin-Darby-canine-kidney cells. Effects of extracellular sodium and calcium. Pflugers Arch, 1986. 407(3): p. 258-63.
[231] Chifflet, S., J.A. Hernandez, and S. Grasso, A possible role for membrane depolarization in epithelial wound healing. Am J Physiol Cell Physiol, 2005. 288(6): p. C1420-30.
[232] Fomicheva, A., et al., Engineering Adenylate Cyclase Activated by Near-Infrared Window Light for Mammalian Optogenetic Applications. ACS Synth Biol, 2019. 8(6): p. 1314-1324.
[233] Tachibana, K., et al., Elucidation of binding specificity of Jacalin toward O-glycosylated peptides: quantitative analysis by frontal affinity chromatography. Glycobiology, 2006. 16(1): p. 46-53.
[234] Hynes, R.O., Integrins: versatility, modulation, and signaling in cell adhesion. Cell, 1992. 69(1): p. 11-25.
[235] Becker, J.W., et al., Topology of cell adhesion molecules. Proc Natl Acad Sci U S A, 1989. 86(3): p. 1088-92.
[236] Shogren, R., T.A. Gerken, and N. Jentoft, Role of glycosylation on the conformation and chain dimensions of O-linked glycoproteins: light-scattering studies of ovine submaxillary mucin. Biochemistry, 1989. 28(13): p. 5525-36.
[237] Wesseling, J., et al., Episialin (MUC1) overexpression inhibits integrin-mediated cell adhesion to extracellular matrix components. J Cell Biol, 1995. 129(1): p. 255-65.
[238] Agrawal, B., S.J. Gendler, and B.M. Longenecker, The biological role of mucins in cellular interactions and immune regulation: prospects for cancer immunotherapy. Mol Med Today, 1998. 4(9): p. 397-403.
[239] Kohlgraf, K.G., et al., Contribution of the MUC1 tandem repeat and cytoplasmic tail to invasive and metastatic properties of a pancreatic cancer cell line. Cancer Res, 2003. 63(16): p. 5011-20.
[240] Paszek, M.J., et al., Integrin clustering is driven by mechanical resistance from the glycocalyx and the substrate. PLoS Comput Biol, 2009. 5(12): p. e1000604.

[241] Paszek, M.J., et al., The cancer glycocalyx mechanically primes integrin-mediated growth and survival. Nature, 2014. 511(7509): p. 319-25.
[242] Syrkina, M.S., D.M. Potashnikova, and M.A. Rubtsov, The length of mucin MUC1 extracellular domain affects integrin-mediated cell adhesion to fibronectin and vitronectin. Biopolymers and Cell, 2019. 35(4): p. 288-302.
[243] Pemberton, L.F., et al., The epithelial mucin MUC1 contains at least two discrete signals specifying membrane localization in cells. J Biol Chem, 1996. 271(4): p. 2332-40.
[244] Silverman, M.A., et al., Motifs that mediate dendritic targeting in hippocampal neurons: a comparison with basolateral targeting signals. Mol Cell Neurosci, 2005. 29(2): p. 173-80.
[245] Arroyo, A.G., et al., Regulation of the VLA integrin-ligand interactions through the beta 1 subunit. J Cell Biol, 1992. 117(3): p. 659-70.
[246] Takada, Y. and W. Puzon, Identification of a regulatory region of integrin beta 1 subunit using activating and inhibiting antibodies. Journal of Biological Chemistry, 1993. 268(23): p. 17597-17601.
[247] Yagi, M., A. Campos-Neto, and K. Gollahon, Morphological and biochemical changes in a hematopoietic cell line induced by jacalin, a lectin derived from Artocarpus integrifolia. Biochem Biophys Res Commun, 1995. 209(1): p. 263-70.
[248] Arockia Jeyaprakash, A., et al., Structural basis for the energetics of jacalin-sugar interactions: promiscuity versus specificity. J Mol Biol, 2005. 347(1): p. 181-8.
[249] Darula, Z., F. Sarnyai, and K.F. Medzihradszky, O-glycosylation sites identified from mucin core-1 type glycopeptides from human serum. Glycoconj J, 2016. 33(3): p. 435-45.
[250] Milner, R. and I.L. Campbell, The integrin family of cell adhesion molecules has multiple functions within the CNS. J Neurosci Res, 2002. 69(3): p. 286-91.
[251] Lilja, J. and J. Ivaska, Integrin activity in neuronal connectivity. J Cell Sci, 2018. 131(12).
[252] Hsieh, P. and L.B. Chen, Behavior of cells seeded in isolated fibronectin matrices. J Cell Biol, 1983. 96(5): p. 1208-17.
[253] Lang, F. and M. Paulmichl, Properties and regulation of ion channels in MDCK cells. Kidney Int, 1995. 48(4): p. 1200-5.
[254] Boocock, D., et al., Theory of mechanochemical patterning and optimal migration in cell monolayers. Nature Physics, 2020. 17(2): p. 267-274.
[255] Uroz, M., et al., Regulation of cell cycle progression by cell-cell and cell-matrix forces. Nat Cell Biol, 2018. 20(6): p. 646-654.
[256] Valon, L., et al., Optogenetic control of cellular forces and mechanotransduction. Nat Commun, 2017. 8: p. 14396.
[257] Inaba, H., Q. Miao, and T. Nakata, Optogenetic control of small GTPases reveals RhoA mediates intracellular calcium signaling. J Biol Chem, 2021. 296: p. 100290.
[258] Mahn, M., et al., Biophysical constraints of optogenetic inhibition at presynaptic terminals. Nat Neurosci, 2016. 19(4): p. 554-6.
[259] Raimondo, J.V., et al., Optogenetic silencing strategies differ in their effects on inhibitory synaptic transmission. Nat Neurosci, 2012. 15(8): p. 1102-4.

Acknowledgments

I would like to express my sincere gratitude to all the people who helped me during my doctoral study at the Institute of Biological Information Processing (IBI-3) of Forschungszentrum Jülich.

First, I would like to sincerely thank Prof. Andreas Offenhäusser for giving me the great opportunity to work in such an interdisciplinary and intercultural academic environment. I appreciate your great support and nice advice on my project. I am also truly grateful to Prof. Björn Michael Kampa for kindly being my second supervisor and for your precious time in reviewing my thesis.

I would like to give my deep thanks to my group leader Dr. Vanessa Maybeck, even though words are unable to fully express my gratitude to you. Thank you very much for accepting me as one of the members of your nice group, and also for your unreserved support, help, and encouragement all the time. Moreover, thanks for always being patient for proofreading my manuscripts. I will keep every little thing you have done for me in my mind, like the moment when you were patiently answering my questions. Your scientific attitude and spirit will always inspire me.

I am thankful to all the colleagues who offered help on my work. Ekaterina, thanks a lot for always being willing to help me whenever I had any problem, especially with Matlab code, I really appreciate your expertise and kindness. Bogdana, you are a patch-clamp specialist, thanks for detailedly answering my questions about patching every time and sharing your knowledge especially on capacitance analysis, your passion for science impressed me. Dominik, thanks for always being kind to provide help, especially at the beginning of my patching and micro-contact printing experiments. Ruoyan, thanks for your help on my experiments, and for being a nice roommate. Frano, thanks for your help on the usage of the live-cell imager. Corinna, thanks for your help with the Apotome setup. Timm, thanks for your introduction to calcium imaging. Lei (Jin), thanks for your previous work from which I benefit a lot. Sarah, thanks for getting me familiar with my project soon in the beginning. Besides, many thanks to our lab technicians and administrators. Tina, thanks for your professional assistance as an excellent biolab technician. Rita, thanks for spending your time proofreading the German abstract of my thesis. Dr. Dirk Mayer, thanks for your nice administration on labs. Michael, thanks for fabricating the pattern stamps for me. Marko, thanks for the introduction about the plasma oven. Elke, thanks for ordering laboratory consumables. Moreover, Lei (Zhou), thanks for always being nice to give me a favor on trivial things, and also for kindly driving us to travel around on holiday. Ann, I will miss all the leisure time we had in Jülich and also the time we spent in Düsseldorf. Lena and Marie, thanks for being nice officemates. Jamal, thanks for helping me solve trivial things in German. Changtong, Yuanying, Yuting, Ting, Erfan, Gabriela, Viviana, Ruifeng, and many other colleagues, thanks for meeting you all in Germany. I would like to thank all the members of ICS-8/IBI-3 for the pleasant and friendly working atmosphere.

Additionally, I appreciate the financial support from China Scholarship Council for my doctoral study abroad.

Finally, I want to thank my friend Dr. Liu, without your encouragement, I would not have had the courage to apply for the doctoral study overseas. Meanwhile, I would like to thank my family and friends for your constant caring and support. Especially, I want to thank my boy friend, thank you for always being there for me, giving me good advice, and supporting me unconditionally. Thank you all very much!

Appendix

Additional Figures

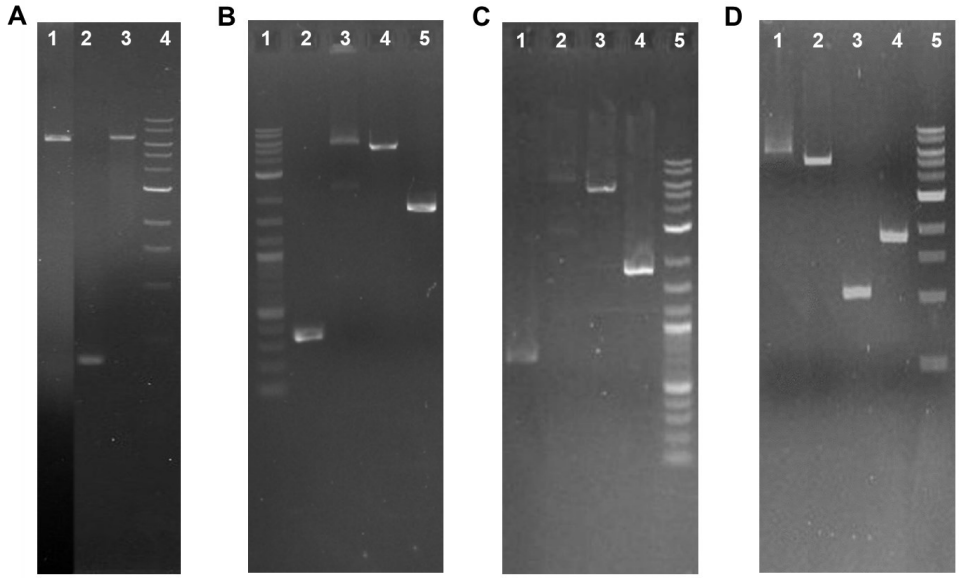

Figure A.1 DNA fragments of plasmids TO-ChR2opt-mKATE-AT and TO-TR-ChR2XXL-YFP before and after assembly shown in gel electrophoresis images.

(**A**) TO-ChR2opt-mKATE-AT. Lane 1, linear TO-ChR2opt-mKATE after double enzyme digestion, 6755 bp; lane 2, AT, 341 bp; lane 3, TO-ChR2opt-mKATE-AT, 7028 bp; lane 4, standard DNA ladder.

(**B**) TO-TR5-ChR2XXL-YFP. Lane 1, standard DNA ladder; lane 2, TR5, 359 bp; lane 3, TO-TR5-ChR2XXL-YFP, 7080 bp; lane 4, linear pcDNA4/TO, 5078 bp; lane 5, ChR2XXL-YFP, 1711 bp.

(**C**) TO-TR10-ChR2XXL-YFP. Lane 1, TR10, 659 bp; lane 2, TO-TR10-ChR2XXL-YFP, 7380 bp; lane 3, linear pcDNA4/TO, 5078 bp; lane 4, ChR2XXL-YFP, 1711 bp; lane 5, standard DNA ladder.

(**D**) TO-TR15-ChR2XXL-YFP. Lane 1, TO-TR15-ChR2XXL-YFP, 7680 bp; lane 2, linear pcDNA4/TO, 5078 bp; lane 3, TR15, 953 bp; lane 5, standard DNA ladder. Figures correspond to Section 2.1.5.

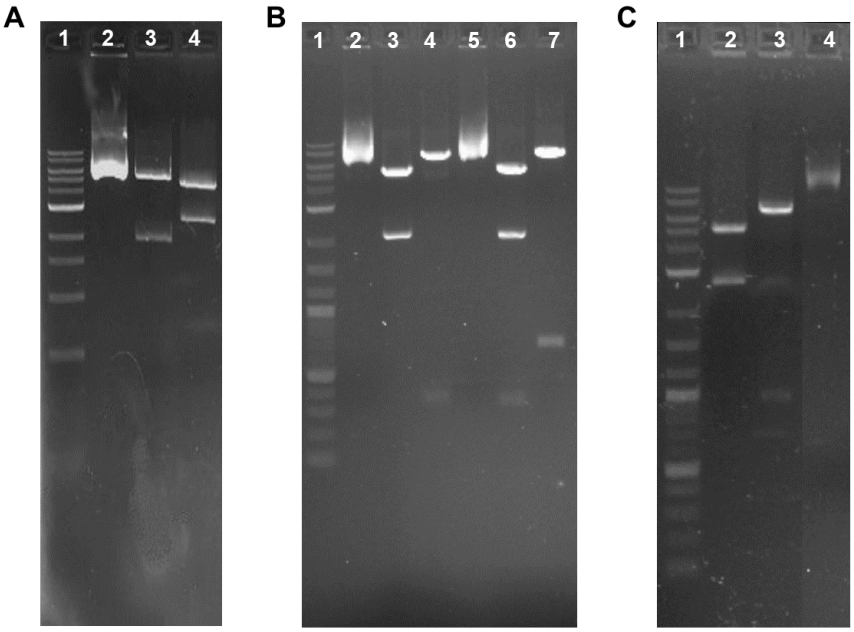

Figure A.2 Evaluation of the constructed plasmids TO-ChR2opt-mKATE-AT and TO-TR-ChR2XXL-YFP by restriction enzyme digestion followed by gel electrophoresis.

(**A**) TO-ChR2opt-mKATE-AT. Lane 1, standard DNA ladder; lane 2, TO-ChR2opt-mKATE-AT, 7028 bp; lane 3, double restriction enzyme digestion 1, 5134 bp and 1894 bp; lane 4, double restriction enzyme digestion 2, 4543 bp and 2485 bp.

(**B**) TO-TR5-ChR2XXL-YFP (lanes 2, 3, and 4) and TO-TR10-ChR2XXL-YFP (lanes 5, 6, and 7). Lane 1, standard DNA ladder; lane 2, TO-MUC5-ChR2XXL-YFP, 7080 bp; lane 3, double restriction enzyme digestion 1, 5078 bp and 2002 bp; lane 4, double restriction enzyme digestion 2, 6753 bp and 327 bp; lane 5, TO-MUC10-ChR2XXL-YFP, 7380 bp; lane 6, double restriction enzyme digestion 1, 5078 bp, 1993 bp, and 309 bp; lane 7, double restriction enzyme digestion 2, 6753 bp and 627 bp.

(**C**) TO-TR15-ChR2XXL-YFP. Lane 1, standard DNA ladder; lane 2, double restriction enzyme digestion 1, 5078 bp and 2602 bp; lane 3, double restriction enzyme digestion 2, 6753 bp and 927 bp; lane 4, TO-TR15-ChR2XXL-YFP, 7680 bp. Figures correspond to Section 2.1.5

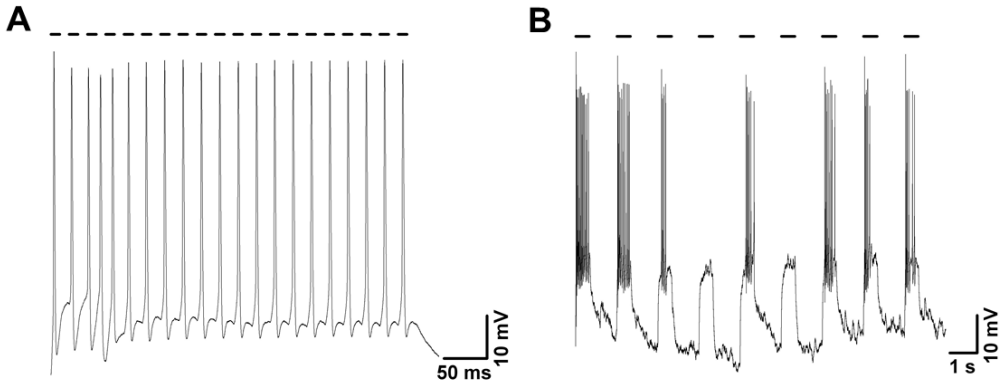

Figure A.3 The voltage traces of ChR2opt-mKATE-AT triggered by blue light in fast-spiking (**A**) and burst-spiking neurons (**B**). (A) Both pulse time and interpulse time were 10 ms. (B) The pulse time was 500 ms, and the interpulse time was 1000 ms. Figures correspond to Section 3.4.3.

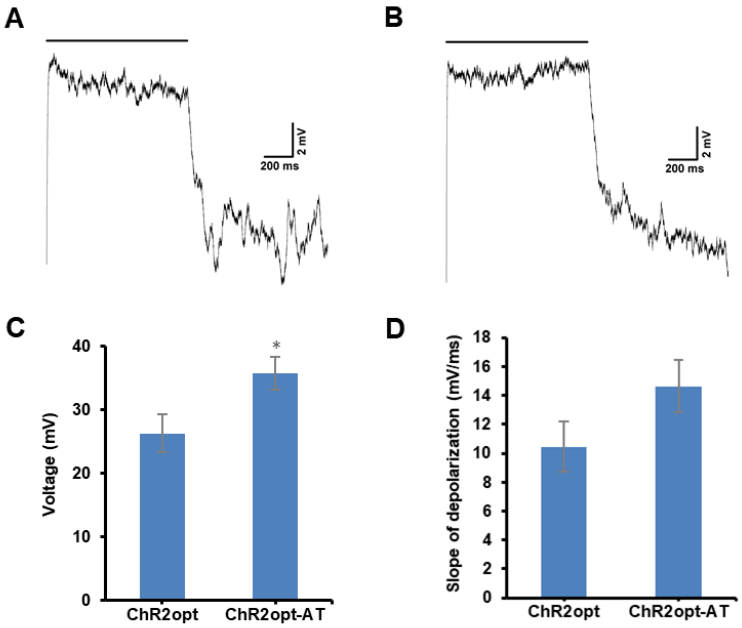

Figure A.4 Electrophysiological characteristics of ChR2opt-mKATE and ChR2opt-mKATE-AT recorded in current clamp mode when expressed in neurons.

(**A-B**) Representative voltage traces produced in cortical neurons expressing ChR2opt-mKATE (A) and ChR2opt-mKATE-AT (B) upon 1 s blue light stimulation.

(**C**) The amplitude of the induced voltage. Data are presented as mean ± SEM, n = 11 and 8. One-Way ANOVA test, $^{*}p < 0.05$.

(**D**) The slope of depolarization evoked by light stimulation, which was determined by linearly fitting voltage traces. Data are presented as mean ± SEM, n = 15 for each group. Mann-Whitney test, $p > 0.05$. Figures correspond to Section 3.5.1.

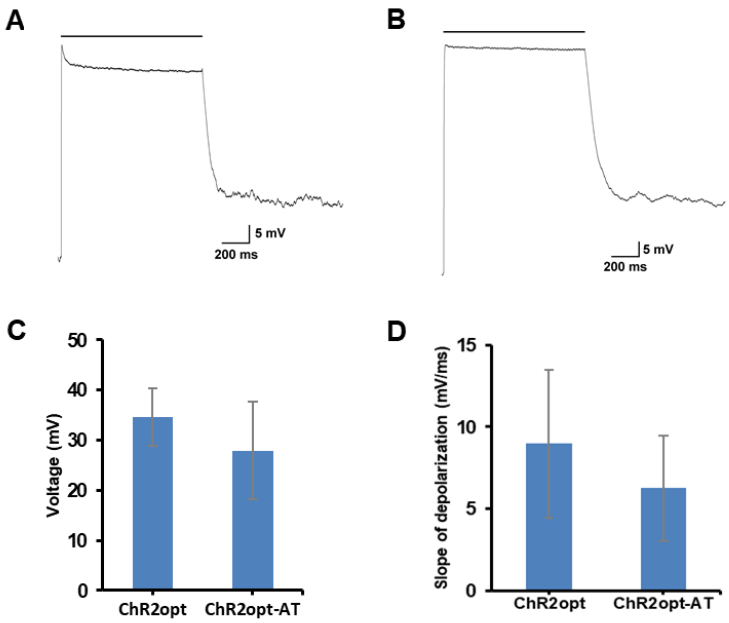

Figure A.5 Electrophysiological characteristics of ChR2opt-mKATE and ChR2opt-mKATE-AT recorded in current clamp mode when expressed in HEK293 cells.

(**A-B**) Representative voltage traces produced in HEK293 cells expressing ChR2opt-mKATE (A) and ChR2opt-mKATE-AT (B) upon 1 s blue light stimulation.

(**C**) The amplitude of the induced voltage. Data are presented as mean ± SEM, n = 8 and 6. Mann-Whitney test, $p > 0.05$.

(**D**) The slope of depolarization evoked by light stimulation. Data are presented as mean ± SEM, n = 5 for each group. Mann-Whitney test, $p > 0.05$. Figures correspond to Section 3.5.2.

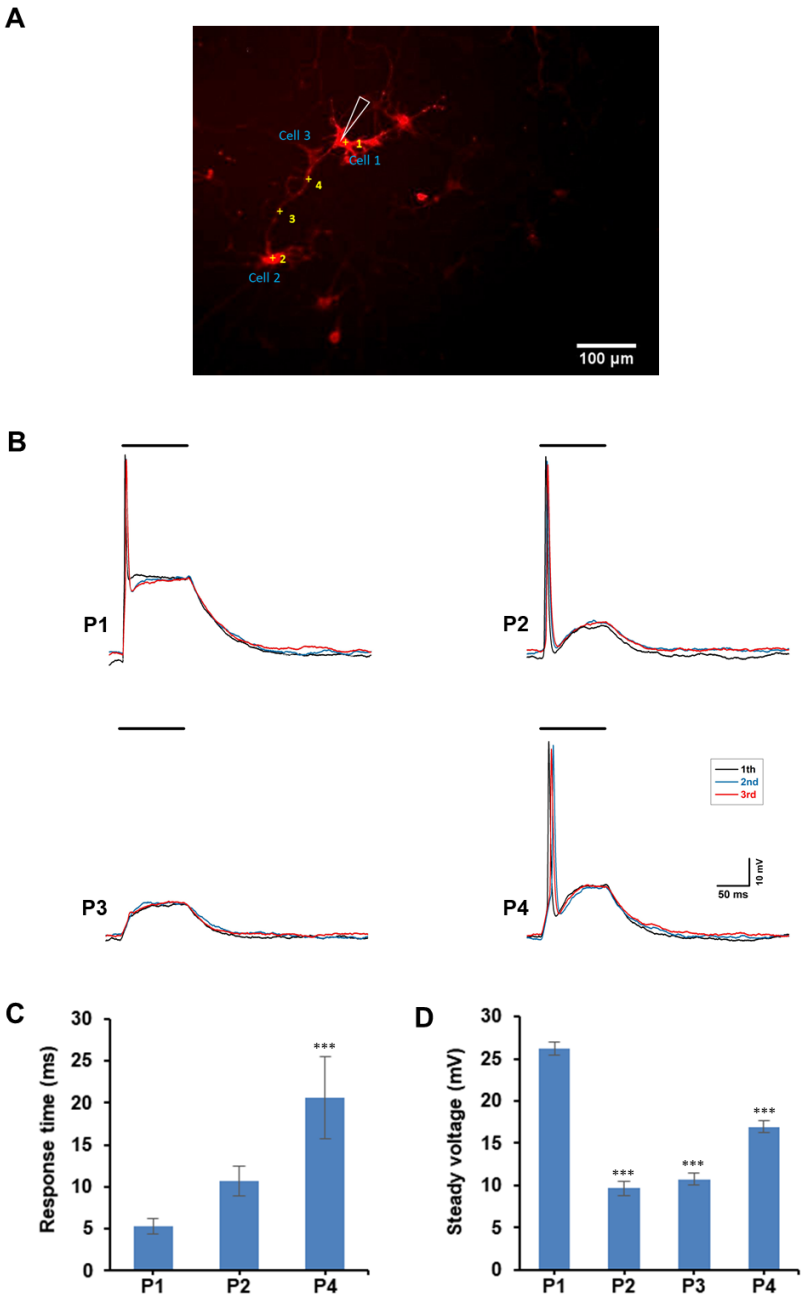

Figure A.6 Optogenetic manipulation with ChR2opt-mKATE to map microcircuits in neural networks.

(**A**) Image of neurons expressing ChR2opt-mKATE in a small neural network. The triangle represents the recording position by patch clamp. The numbers represent laser stimulation positions successively in one round. Scale bar, 100 µm.

(**B**) The induced voltage traces at soma upon light stimulation at P1 (Position 1), P2, P3, and P4 in the first three rounds. The pulse time was 100 ms, and the interpulse time was 900 ms.

(**C**) The response time to reach the peak of an action potential elicited by stimulating at individual positions. Kruskal-Wallis One-Way ANOVA test, $^{***}p<0.001$, against the value at P1.

(**D**) The amplitude of the induced voltage at a steady state. One-way ANOVA test, $^{***}p<0.001$, against the value at P1. Figures correspond to Section 5.1.3.

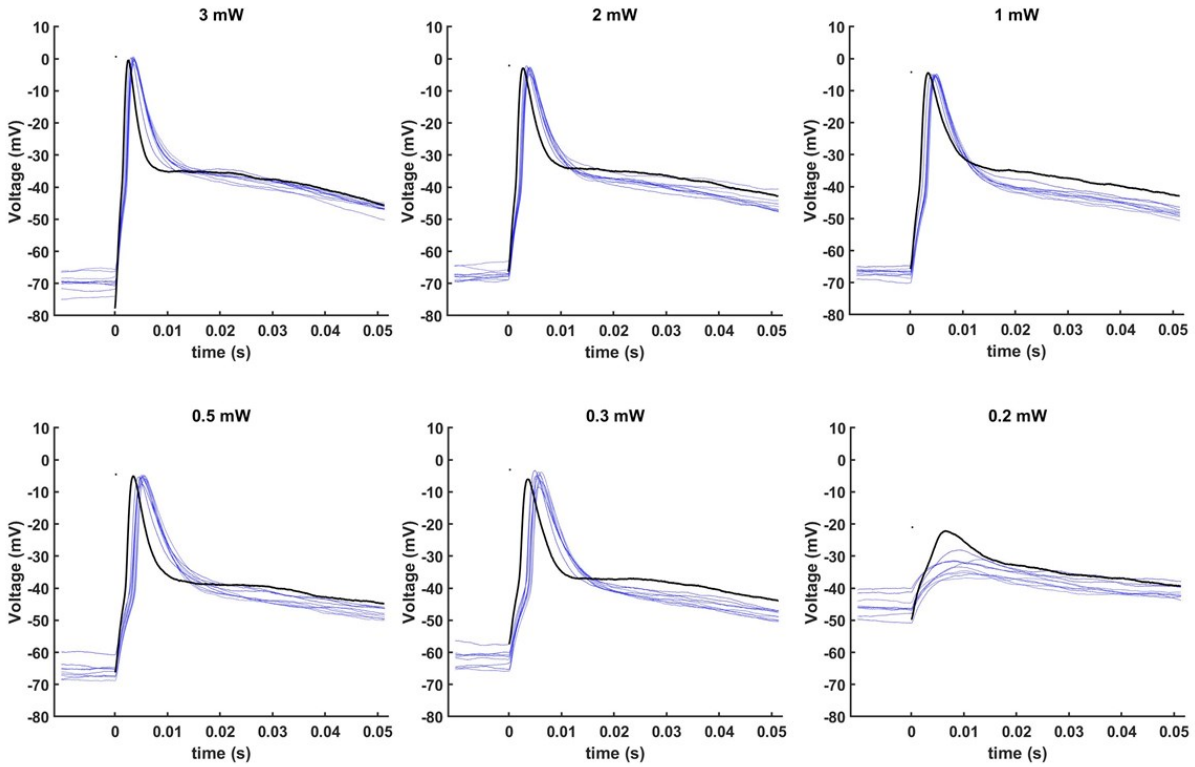

Figure A.7 The voltage traces of ChR2opt-mKATE-AT under light stimulations with a series of output powers ranging from 3 mW to 0.2 mW when expressed in primary neurons. The radius of the laser spot size was about 6 μm. The pulse time was 0.01 ms, and the delay time was 1000 ms. The first trace, black line; the other nine traces, blue line. Figures correspond to Section 5.1.6.

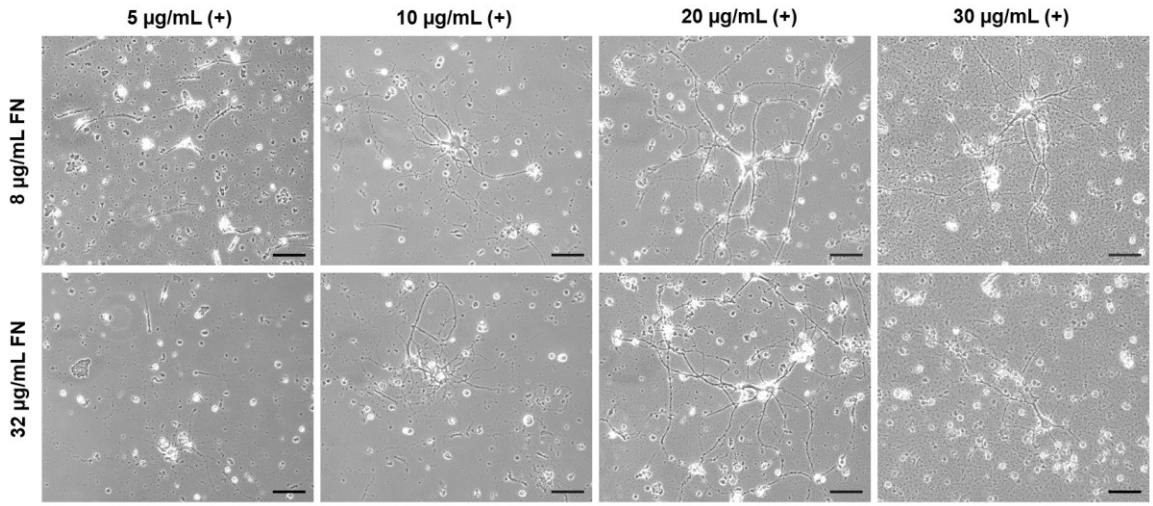

Figure A.8 The effect of jacalin on neurons grown on glass coverslips coated with ECM containing 8 µg/mL (upper row) or 32 µg/mL (lower row) fibronectin (FN). The concentrations of jacalin in the culture media were 5 µg/mL, 10 µg/mL, 20 µg/mL, and 30 µg/mL as indicated with (+) in the figure. Scale bar, 50 µm. Figures correspond to Section 5.2.4.

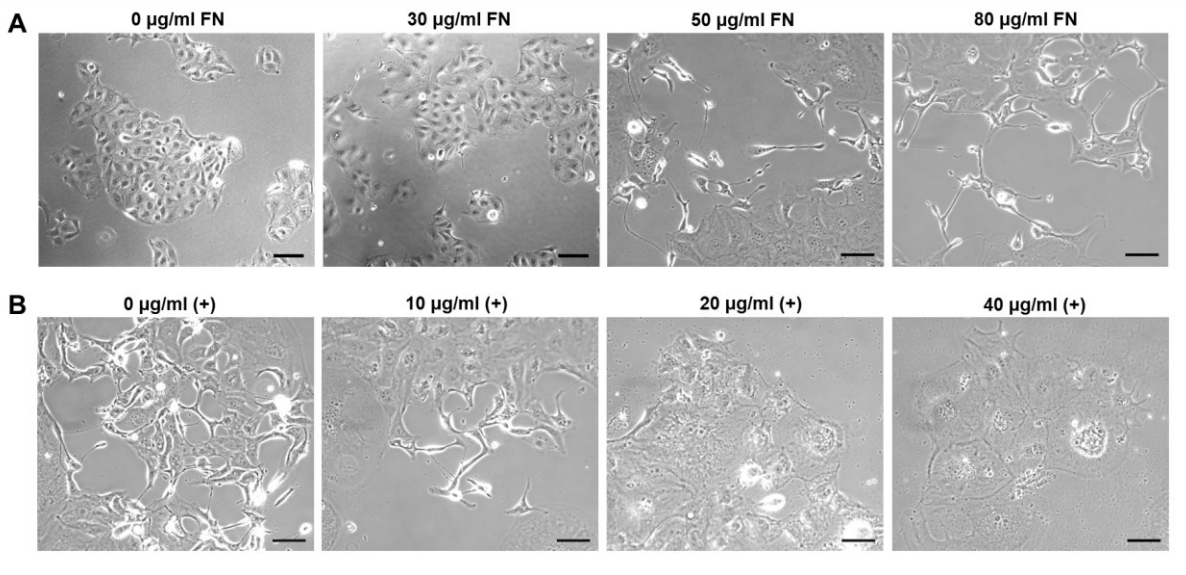

Figure A.9 The influence of fibronectin and jacalin on the morphology of MDCK cells.

(**A**) The morphology of MDCK cells grown on glass coverslips coated with ECM containing different concentrations of fibronectin (FN).

(**B**) The effect of jacalin on MDCK cells grown on glass coverslips coated with ECM containing 80 µg/mL FN. The concentrations of jacalin in the culture media were 0 µg/mL, 10 µg/mL, 20 µg/mL, and 40 µg/mL as indicated with (+) in the figure. Scale bar, 50 µm. Figures correspond to Section 5.2.4.

List of Figures

Abbreviations

aa	Amino acid
ACR	Anion channelrhodopsins
ADR	Axon-to-dendrite expression ratio
AIS	Axon initial segment
Arg/R	Arginine
Asp/D	Aspartic acid
AT	Apical targeting
ATP	Adenosine triphosphate
AP	Action potential
bp	Base pair
BR	Bacteriorhodopsin
CCR	Cation channelrhodopsins
CD	Cluster of differentiation
ChR1	*Chlamydomonas reinhardtii* Channelrhodopsin-1
ChR2	*Chlamydomonas reinhardtii* Channelrhodopsin-2
ChR2opt	Optimized ChR2(H134R)
ChR2XXL	ChR2(D156C) (extra high expression and long open state)
CMV	Cytomegalovirus
Cys/C	Cysteine
DAPI	4’,6-diamidino-2-phenylindole
DIV	Day *in vitro*
DNA	Deoxyribonucleic acid
DPT	Day post transfection
ECM	Extracellular matrix
ER	Endoplasmic reticulum
FN	Fibronectin
fS	Femtosiemens
FWHM	Full width at the half maximum
GPCR	G-protein-coupled receptors

HEK293	Human Embryonic Kidney 293
His/H	Histidine
HR	Halorhodopsin
hSyn	Human synapsin
LED	Light-emitting diode
MAP	Microtubule associated protein
MDCK	Madin-Darby canine kidney
mKATE	Mutated Katushka
MUC	Mucin
NpHR	*Natronomonas pharaonis* Halorhodopsin
PCR	Polymerase chain reaction
PLL	Poly-L-lysine
RIS	Rod inner segment
ROS	Rod outer segment
$RSBH^+$	Protonated retinal Schiff base
SEM	Standard error of mean
SFO	Step function opsin
SD	Standard deviation
TCP	Tissue culture plastic
TGN	Trans-Golgi network
TM	Transmembrane
TR	Tandem repeat
uADR	Unnormalized axon-to-dendrite expression ratio
VN	Vitronectin
YFP	Yellow fluorescent protein

Declaration of Authorship

I, *Jiali Wang*, declare that this thesis and the work presented in it are my own and has been generated by me as the result of my own original research.

I do solemnly swear that:

1. This work was done wholly while in candidature for the doctoral degree at this faculty and university;

2. This thesis has not been submitted for any other degree or title at this university or any other institution;

3. Where I have consulted the published work of others or myself, this is always clearly attributed;

4. Where I have quoted from the work of others or myself, the source is always given. This thesis is entirely my own work, with the exception of such quotations;

5. I have acknowledged all major sources of assistance;

6. The thesis is mostly based on the work done by myself. I performed all the experiments and data analyses except the parts that I point out below. Vanessa Maybeck helped me with the design of the study and contributed to the patching experiment in polarized MDCK cells; Ekaterina Savelyeva helped me with Matlab code; Bogdana Cepkenovic helped me with Python code for capacitance analysis; and Vanessa Maybeck and Andreas Offenhäusser provided critical discussion and insights.

7. Parts of this work are in preparation for publication as:
Characterization and Subcellular Targeting of Channelrhodopsin-2 Mediated by the Cytoplasmic Tail of Rhodopsin. Jiali Wang, Ekaterina Savelyeva, Bogdana Cepkenovic, Andreas Offenhäusser, Vanessa Maybeck[*].

Parts of this work have been submitted for publication as:
Expressing Optogenetic Actuators Fused to N-terminal Mucin Motifs Delivers Targets to Specific Subcellular Compartments in Polarized Epithelia and Neurons. Jiali Wang, Andreas Offenhäusser, Vanessa Maybeck[*].

14. 11. 2022

Jiali Wang